APPLICATION OF DISCRETE MULTIPHYSICS TO FLUID-STRUCTURE-INTERACTION SIMULATION OF VASCULAR FLOWS

By

ADAMU MUSA MOHAMMED

A thesis submitted to the University of Birmingham for the degree of DOCTOR OF PHILOSOPHY

School of Chemical Engineering

College of Engineering and Physical Sciences

The University of Birmingham

October 2021

ABSTRACT

The advent of computer simulation has not only reduced the cost and time for testing a suitable design or product through expensive experiments but also become a potential tool for an in-silico and in-vitro research. With computer simulations different solutions can be evaluated numerically and only promising designs are sent to laboratory or production line for scale-up production. In this thesis, flow problems related to cardiovascular disorders in humans were studied using a mesh-free particle modelling technique. Since cardiovascular disease is the main cause of death worldwide, study into its causes, progression, and treatment is necessary. Therefore, the diseased cardiovascular organs (aortic valve and coronary artery) which are solid, and the blood (liquid) are represented as particles, constituting the full geometry that is employed for this study. This takes us to the use of a framework known as Discrete Multiphysics, which integrates two particle approaches, notably the Lattice Spring Model for solid mechanics and Smooth Particle Hydrodynamics for fluid mechanics. Employing this approach therefore, the mesh-free particle method in the form of discrete multiphysics was used to simulate the two cardiovascular problems with complex geometries, (i) effect of aortic valve calcification on blood flow and deformation of the valve (ii) the interaction between fluid (blood) and solid (arterial wall and stent) within a coronary artery implanted with a metal stent. In the case of aortic valve, the effects of various calcification stages (ranging from mild to severe) on cardiac output were simulated and evaluated. It was found that increasing levels of calcification result in a reduction in heart flow rate, and a critical threshold of calcification exists below which the flow rate drastically declines. Additionally, in the case of coronary stents, the key factors that affect how much the stent deforms are sorted according to dimensionless numbers, and a connection between the elastic forces of the stent and the pressure forces of the fluid is formed. The blood flow and stiffness of the stent material were

subsequently found to considerably contribute to the stent's deformation and to have an impact on its rate of deformation. In both cases however, mechanical stresses were analysed and how the severity of calcification as well as the elastic and pressure forces affect the rate of deformation of the valve and the stent respectively were investigated. Therefore, it will be convincingly concluded that despite the complexity of these biological organ's geometries, we were able to achieve the solid-liquid mechanics analyses with little difficulty, thanks to Discrete Multiphysics modelling approach.

Keywords: geometry, mesh, mesh-base method, particle-based method, smooth particle hydrodynamics, lattice spring model, discrete multiphysics, conical electrodes, aortic valve, coronary stent, calcification, stenosis, mechanical deformation, fluid structure interaction.

DEDICATION

This thesis is dedicated to my family.

ACKNOWLEDGEMENT

I want to sincerely express my appreciation and thanks to the Nigerian government through the Petroleum Technology Development Fund (PTDF) for finding me suitable for the scholarship award to study in the UK for my PhD.

I truly want to express my unreserved gratitude to my supervisor Dr Alessio Alexiadis for his immense support and guidance through this research. He has groomed me academically and to say that I learned a lot from him is an understatement. The entire work would not have been achievable without his guidance. He showed me the way of publishing my work in a reputable journal while the PhD is ongoing.

I also want to thank my family especially my mother and my wives for supporting me both physically and emotionally through this challenging period. My children are also appreciated for their patience. Your sacrifices are highly appreciated.

My collaborators Mostapha Ariane, Reez Neil, Mustapha Iqbal and my research group members Andrea, Michael, and Danilo are also appreciated for their contribution and sharing of ideas.

Thanks to Nigerian Muslim Forum UK (NMFUK) and Nigerian community in University of Birmingham for being another family in another country. Special thanks to my brother (from another mom) Ali Musa whom we started this journey together. I also want to appreciate my Nigerian colleagues in persons of Usman Tee, Bilyaminu, bashir (Bash), Suleiman, Mukhtar, Abubukar (Habu Na-Sabuwa), Mustapha (German scientist), Sagir and Mudi for their emotional support.

LIST OF PUBLISHED ARTICLES AND CONFERENCES

The following papers were published from the thesis:

- **Mohammed, A.M.**, Iqbal, M., Rees, N.V., Alexiadis, A., 2019. Computational study of mass transfer at surfaces structured with reactive nanocones. Applied Mathematical Modelling 74, 373–386. https://doi.org/10.1016/j.apm.2019.04.057

- **Mohammed, A.M.**, Ariane, M. and Alexiadis, A. (2020) Using Discrete Multiphysics Modelling to Assess the Effect of Calcification on Hemodynamic and Mechanical Deformation of Aortic Valve. ChemEngineering, 4 (3): 48. doi:10.3390/chemengineering4030048.

- **Mohammed, A.M.**, Ariane, M. and Alexiadis, A. (2021) Fluid-Structure Interaction in Coronary Stents: A Discrete Multiphysics Approach. ChemEngineering, 5 (3): 60. doi:10.3390/chemengineering5030060.

The work was also presented in the following conference:

- **Mohammed, A.M.**, Ariane, M., Alexiadis, A. Assessing the Effect of Calcification in Aortic Valve Using Particle-Method Modelling. Presented as poster at 11th PGR BEAR Conference, Birmingham, 2021

TABLE OF CONTENTS

LIST OF FIGURES

LIST OF TABLES

CHAPTER1: INTRODUCTION

1.1 Computer Modelling and Simulation

Modelling and simulation can be considered as a discipline on its own; one that necessarily support the integration of other disciplines for application (Sokolowski and Banks, 2010). It has become academic program of choice for science and engineering students and can be used for a wide range of applications both in the industry and academia. For many industrial applications, a loss is prevented through simulation. In order word, all the likely failures and problems that may be encountered when running a process, must have been seen and corrected from the simulation results. Therefore, modelling and simulation is getting information about how something will behave without testing it in real life (Sharma and Sharma, 2014). Simulation provide an alternative approach of scientific investigation preventing a time-consuming, very expensive and dangerous experiments in laboratory or on site (Liu and Liu, 2003). Therefore, as a technique or tool for loss prevention modelling and simulation's benefits cannot be quantified.

Modelling starts with developing a model which gives an approximate representation of the real live problem and also represent key characteristics or behaviour of a physical process or system. Then modification and repeated observation of the model is done through simulations in order to obtain a desired result. Verification, conclusion, and validation of the data obtained from the simulation is done and hence makes modelling and simulation a problem-based tool that is used for testing hypothesis. To differentiate between modelling and simulation, it can be said that the model represent a system whereas the simulation represents the operation of the system over time (Banks, 2001). In other word, the distinction between "model" and "simulation" can be compare with the difference between representation and imitation. Whether written on paper or into a computer language a model remains a representation of

the system (problem) whereas simulation is the imitation of the behaviour of the system (Kaizer et al., 2015). However, a model can be viewed as an abstraction of reality as it is a simplified representation of a complex real system, and no matter how good a model is it cannot capture all the factors of the system (Jenner, 2012). According to George Box all models are wrong, but some are useful (Box, 1999).

Mathematical modelling and computer simulation are increasingly becoming valuable to the field of science and technology. In biology and medicine, for instance, computer simulation gives understanding of a biological system under investigation since it provides details on both the fluid and the solid dynamics (Ariane, 2018a). Fluid and solid interacting at the same time (fluid structure interaction FSI) is a complex phenomenon, difficult to solve analytically but amenable to numerical simulation. However, the simulation of a system with a multiple physical phenomenon is possible today and is referred to as multiphysics simulation.

1.2 Multiphysics Modelling

Multiphysics is the science of studying multiple interacting phenomena and can be considered the royal discipline of numerical modelling to solve scientific and engineering problems due to its complexity and coverage of range of physical fields. Numerical methods are the essential tool for predicting and simulating the multiphysical behaviour of interacting complex engineering systems (Peksen, 2018) and due to progress and upgrades in numerical methods, multiphysics recorded a significant development in the last century.

The definition of multiphysics is very broad and may include coupled physical phenomenon in computer simulation which may consists more than one component governed by its own principle of evolution or equilibrium (Krzhizhanovskaya and Sun, 2007; Liu, 2018). To carry out multiphysics simulation identification of a system that is set to be analysed is required.

Geometry, materials and domain are to be specified and the system will be finally interpreted using mathematical languages (models) such as partial differential equation (PDE) as the auxiliary or governing equation (Liu, 2018) and the solutions and postprocessing is done with the aid of a computer using appropriate solver.

The modelling approach could be the traditional continuum multiphysics where the system is considered a whole single body and the model is solved using a large system of ordinary differential equation or partial differential equation (PDE), which traditionally are solved numerically over computational grids with techniques such as the Finite Element Method (FEM). The solution is achieved using a meshed geometry to represent the system's domain. The continuum model can be grided with a Lagrangian or Eulerian mesh. Discrete Multiphysics (DMP) is an alternative to mesh-based multiphysics. DMP considers the system as and integration of particles (like cells in biology); these particles are connected to each other to form the complete structure. This method linked two or more particle methods such as SPH, Lagrangian particle method, LSM and DEM together. Since each particle is treated independently, discrete Multiphysics is said to have, in some instances, a better representation of the physics of the system domain and often gives more accurate results compare to mesh-based approach (Desrues et al., 2019).

1.3 Application

There are many academic articles on the application of modelling and simulation to solving real life problems. Today modelling and simulation is being applied in many areas and discipline, for instance, the smooth particle hydrodynamic (SPH) model is used in a variety of fields and has a wide range of applications such as multiphase flow, biomedicals, fluid–solid interaction, and hydrodynamic instability (Mohammed et al., 2020). In biology and

biomechanics DMP was used to model a blood flow in flexible biological valve and simulate the flow and agglomeration in deep veins valves (Ariane, 2018a). Hydrodynamics and mixing profile of human proximal colon (Schütt et al., 2020a) as well as human physiology of the autonomic nervous system (Alexiadis, 2019b) were also simulated using DMP modelling or some versions of it. Rahmat et al., 2019a used SPH which is a DMP model to simulate the dissolution of solid particles in fluid flow and also used incompressible smooth particle hydrodynamic (ISPH) to simulate droplet coalescence and electro-coalescence (Rahmat and Yildiz, 2018).

In the other hand, the application of mesh-based simulation has been in practice long before the particle method for modelling complex systems in many disciplines across science and engineering. In that approach, the mesh cells are used as discrete local approximations of the larger domain and are now created by computer algorithms. With high performance computers, meshes of high resolution are generated and perhaps the increase of computational power has influenced the rapid development of software for both mesh and particle-method simulations. Some examples of commercial and non-commercial software used for mesh generation, calculations and post-processing include Abaqus, Gmsh, Grid-Pro, ANSYS, COMSOL Multiphysics, Code Aster, LS-DYNA, Elmer, LAMMPS, Ovito, etc.

In this thesis, therefore, the application of particle simulation and, subsequently, the application of DMP will be used to analyse flows in the cardiovascular system and how is affected by the structural changes in the vascular tissues (heart and or blood vessels). These flows often become irregular or distorted due to the dynamic nature of the heart and or blood vessels when its original structure changes as a result of physical injury or disease.

1.3.1 Cardiovascular system

The vascular system plays a key function in transporting oxygen-rich blood, nutrients, and waste products to every organ and tissue. The cardiovascular system is made up of the heart operating as a pump and the blood arteries used for this delivery of vital nutrients and oxygen. (Jarvis, 2018). Therefore, the cardiovascular system provides blood supply to the body and can equally control the amount of the blood transported through the vessels. Coupled together, the cardiovascular system consists of the heart and the blood vessels (arteries veins, and capillaries) which works together to provide adequate blood flow all parts of the body (Chaudhry et al., 2022). This role made the cardiovascular system very important as it helps the body meet the demand for activity, exercise and stress and maintaining the body temperature.

There are a lot of cardiovascular diseases (CVD) which occur as a result of poor performance of the system. Such diseases include disease affecting the heart and blood vessels such as coronary heart disease, aortic disease, stroke, transient ischaemic attack (TIA) etc. Therefore, to avoid most of these diseases one has to indulge in and exercise to allow free and efficient blood flow. Cardiovascular exercise made a person to become fit, and more the fit a person is the better transfer of oxygen from the lungs to the minor blood vessels. It was confirmed that the consistent exercise will also improve performance of heart as a pump which in turn also increase the efficiency of blood transport into surrounding vasculature (Lee and Jung, 2015). To further highlight the need for a constant blood flow it is worthy of note that its aids in maintaining the elasticity of the blood vessels and avoid vessels difficulties such as plaques and blockage (stenosis).

Therefore, to improve the efficiency of blood transport in the body and reduce cardiovascular diseases, one need a regular exercise. The American college of sports and medicine (ACSM) set a guideline for cardiovascular exercise. Its recommend that all healthy adults aged 18-65 years should participate in moderate intensity aerobic physical activity for a minimum of 30 min on five days per week, or vigorous intensity aerobic activity for a minimum of 20 min on three days per week (Bayles et al., 2018). This translates to expenditure of 500Kcal/week and 1000Kcal/week through cardiovascular exercise to reduce the risk of cardiovascular diseases and mortality (Lee and Jung, 2015). Generally, every adult should perform activities that maintain or increase muscular strength and endurance for a minimum of two days per week. This is to avoid potential risk of cardiovascular diseases.

1.3.2 Cardiovascular disease

Cardiovascular disease (CVD) is the umbrella term for illnesses that damage the heart or blood vessels. It is frequently associated with atherosclerosis, a buildup of fatty deposits in the arteries that increases the risk of blood clots. It might also be related to arterial damage in a number of organs, including the kidneys, eyes, heart, and brain. CVD is one of the leading causes of mortality and disability worldwide, however leading a healthy lifestyle can typically greatly reduce your risk (WHO, 2021). There are many different types of CVD, but the following are the most prevalent ones:

i. Coronary heart disease
ii. Aortic disease
iii. Stroke, and
iv. Peripheral arterial disease

In order to prevent or lessen the risk factor, it is important to understand how these diseases manifest themselves and how to anticipate their negative impact on human life. Therefore, this research will use computer simulation to examine two of these most common CVDs—aortic and coronary heart disease.

1.4 Why Computer Simulation?

The benefit of computer modelling is to allow a scientist to conduct thousands of simulated experiments by computer to solve the problem being studied. Computer simulation can save time, money, and life. Instead of spending hours, days and perhaps years to carrying out repeated laboratory experiments, you can run the same experiment at the comfort of your office or home in lesser time without spending money on laboratory reagents. Computer simulation is also crucial to auto safety. Automobile crash-testing need not to be carry out on road rather an engineer can run the test inside computers. It also allows early-stage performance comparison of different designs while cars are still on drawing board, saving money and injuries.

Computational models can be used to study complex systems such as weather forecasting by predicting numerous atmospheric factors, flight simulators where complex equations that govern how aircraft flies defying the effect of turbulence, air precipitations and density. Computational modelling also bring improvement in medical care and research. It is used to study biological systems at multiple levels and models the development and tracking of infectious disease by studying the cell-to-cell interactions, and how those changes affect tissues and organs.

Today the application of computer simulation is vast and practiced in almost all discipline however the use of discrete multiphysics modelling approach is not extended to many areas of

science and engineering and is still considered to be in its early stage hence, the need for continuous exploitation of this method and therefore more research and expertise is needed.

1.5 Aim and objectives

The aim of this work is (i) to use computer simulation to study flows in the cardiovascular system using Discrete Multi-Physics (a combination of particle method, and (ii) to demonstrate that Discrete Multi-Physics can be use more conveniently to tackle problems that are considered very challenging with mesh-based (continuum) multi-physics.

The following objectives are to be achieved:

- ✓ To apply Discrete Multi-Physics to assess the effect of calcification on hemodynamic and mechanical deformation of aortic valve.
- ✓ To evaluate the importance of stiffness, stress, and the blood flow stagnation on the assessment of valve calcification severity
- ✓ To apply discrete multiphysics to simulate the fluid-structure interaction in coronary stent accounting for its mechanical deformation.
- ✓ Demonstrate that Discrete Multiphysics framework can be used to solve problems that perceived to be complicated using traditional modelling approach.

These objectives were chosen with the goal to cover several challenging problems, both in terms of modelling application and solving technique, that prove a wide overview of the capabilities and the power of mathematical modelling in engineering.

Besides those scientific objectives. This thesis also goes towards my personal ambitions to develop in an all-round fashion my individual skill as a ‘mathematical modeller’. My personal goal was to have a hand-on experience in both mesh-based and particle-based method. I

wanted to specialize and gain an in-depth knowledge and expertise in mathematical modelling and computer simulation. Three papers were published from the research carried out in this thesis. These three studies refer to different applications that require different modelling techniques and approaches. This was made on purposes in order to gain experience on a variety of different applications.

1.6 Layout of Study

The thesis structure is organised into the following outlines:

Chapter 1: Introduction: Introduces the mesh-based approach to modelling and application of Discrete Multiphysics to Vascular Flows

Chapter 2: Reviews of literature on cardiovascular flow problems including flows through calcified aortic valve and flow through stented artery.

Chapter 3: Methodology: Introduces the discrete multiphysics (particle method) approach and computational set ups.

Chapter 4: A result chapter that applies discrete multiphysics to access the effect of calcification on hemodynamics and mechanical deformation of aortic valve.

Chapter 5: A result chapter that also applies discrete multi physics modelling to study the Fluid-Structure Interaction in a stented coronary artery.

Chapter 6: conclusion, summary of all findings, and perspective for future work.

CHAPTER TWO: LITERATURE REVIEW

2.0 Introduction

The computational analysis of the cardiovascular system and cardiovascular disorders is reviewed in this chapter. It became clear that such investigations might use both conventional mesh-based and mesh-free particle modelling techniques. Therefore, the overall idea of this mathematical modelling is described with a focus on the particle approach, which also includes the discrete multi-physics (DMP) framework methodology for merging two or more of these particle methods. The development of DMP and its present condition are also examined. It is emphasised how the DMP framework can be used to research vascular flows and flows that are impacted by cardiovascular illnesses.

2.1 Vascular flows

The flow within the blood vessels and the transport of nutrients, oxygenated blood and metabolic waste is a complicated transport phenomenon. The dynamic of blood flow (hemodynamics) is based understood using rheology rather than hydrodynamics. This is because the blood itself is non-Newtonian fluid and the blood vessels are non-rigid tubes, as such the classical fluid mechanics and hydrodynamics cannot explain the hemodynamics (Thiriet, 2008). With the heart as the driver of the circulatory system blood is being pumped out of the heart to the rest of the body through contraction and relaxation. The output from the heart first goes to the aorta before it proceeds to other parts of the body by subdividing into smaller arteries, then arterioles and capillaries where the oxygen transfer finally occurred. The flow could be smooth (laminar) or rough (turbulent) depending on the smoothness of the blood vessels.

Vascular flow in human body involves different mechanism such as pulsatile flow, valve movements, coagulation and aggregation. However, when there is a plaque or build-up of fatty

deposit on the arterial wall the flow tends to be turbulent which often signifies abnormal flow. The abnormality in the flow indicates the presence of a cardiovascular disease. There are several in-vivo imaging techniques available for valve disease detection such as the Doppler echocardiography, or the Magnetic Resonance Imaging (MRI) among others (Masci et al., 2008; Myerson, 2012).

2.2 Cardiovascular Disorder

Cardiovascular disorder or popularly known as cardiovascular disease (CVD) is an umbrella term covering a number of connected pathologies, including coronary heart disease (CHD), cerebrovascular disease, peripheral arterial disease, rheumatic and congenital heart illnesses, and venous thromboembolism. Mortality from CVD accounts for 31% of deaths worldwide, with CHD and cerebrovascular accident making up the majority of these deaths (Stewart et al., 2017).

The understanding of the aetiology of CVD and its treatment has been static for thousands of years. Only in the latter half of the 20th century did research into the causes of CVDs pick up speed, leading to the discovery of new treatments (Hajar, 2017). What was the catalyst for this study? This research was sparked in the USA by the early demise of US President Franklin D. Roosevelt from hypertensive heart disease and stroke in 1945 (Mahmood et al., 2014). At that time, deaths from CVD and stroke in the USA had pandemic proportions, prompting Americans to lead cardiovascular research (Mahmood et al., 2014; Hajar, 2017). Today there are several studies on CVD and their treatments (Hajar, 2017; Badimon et al., 2012; Roth et al., 2020) and therefore the burden of CVDs can be ameliorated by careful assessment and reduction of the risk factors.

Atherosclerosis (from aortic and coronary artery diseases) is a common element in the pathophysiology of CVD, thus addressing risk factors connected with its development is crucial. Although CVD may directly result from several aetiologies, such as emboli in a patient with atrial fibrillation that result in ischemic stroke or rheumatic fever that causes valvular heart disease, among others, it is vital to address risks factors related to their formation (Olvera Lopez et al., 2022).

In this chapter therefore, the aetiology and pathology of these diseases will not be discussed in detail; instead, we will evaluate the impacts these diseases may produce and how to track their progression in order to forecast the risk that will aid us in proposing solutions in a timely manner.

2.2.1 Aortic valve disease

Aortic valve is a valve located at the left ventricle and the aorta of the heart. As the name 'valve' it controls the forward and backward flow of the blood. When this valve malfunctioned there may be inadequate flow in and out of the heart due to blockage, a condition called aortic valve stenosis (AS) which happened when the cusps of the aortic valve become thick and stiff or fused together. This narrows the valve's diameter and reduces blood flow from the heart to rest of the body. Moreover, the stiffness of the valve sometimes causes a backflow of blood, another condition called aortic valve regurgitation (AVR). This happened when the valve does not close properly causing the blood to flow backward into the left lower chamber of the heart.

However, aortic valve may just thicken leading to a condition known as aortic valve thickening (AVT). This condition is common, and it occurs without necessarily having the aortic valve stenosed. According to Cosmi et al., 2002, AVT may be consider as the beginning of AS and establish the fact of checking whether AVT patients are at risk of developing AS where he

found that “although AVT is often considered the benign, it is known that patient with AVT have risk factor for the development of cardiac disease” and therefore, AVT may progress significantly to an AS (Cosmi et al., 2002). The aortic thickening and stiffening may occur as a result of calcium deposit (aortic valve calcification AVC), age, or congenital (at birth).

The aortic thickening and stiffening may occur as a result of calcium deposit (aortic valve calcification AVC), age, or congenital (at birth). The calcium deposit can build-up on the heart valve which may not exhibit any symptoms until old age. The incidence of aortic valve calcification has shown an increasing rate of 12% for age group 80 and above while is just shown to 5% in age less than 50 (Leopold, 2013). This is a clear indication that AVC does not manifest at lower age until later in life. However, the condition is deadly as it progresses from mild to moderate and then severe. In severe calcification the valve does not open widely enough to allow smooth blood flow, and this makes the heart works harder enough to pump the blood in order to meet the body’s demand. As time goes on, the excessive work of the heart make it weaken and lead to potential heart failure.

2.2.1.1 Aortic valve calcification

Aortic valve calcification (AVC) is a disease that affect the heart’s valve due to calcium deposit on the valve leaflets and is commonly found in the elderly. The calcium deposit can build-up on the heart valve which may not exhibit any symptoms until old age. The incidence of aortic valve calcification has shown an increasing rate of 12% for age group 80 and above while is just shown to 5% in age less than 50 (Leopold, 2013). This is a clear indication that AVC does not manifest at lower age until later in life. However, the condition is deadly as it progresses from mild to moderate and then severe. In severe calcification the valve does not open widely enough to allow smooth blood flow, and this makes the heart works harder enough to pump the blood in order to meet the body’s demand. As time goes on, the excessive work

of the heart make it weaken and lead to potential heart failure. Age, gender, hypercholesterolemia, diabetes, hypertension, smoking, and renal failure are all risk factors for AVC, as are those for atherosclerosis. AVC is similar to atherosclerosis in many ways, including inflammatory cells and calcium deposits, and it correlates with coronary plaque burden. The presence of AVC is linked to an increased risk of adverse cardiovascular events (Wasilewski et al., 2012).

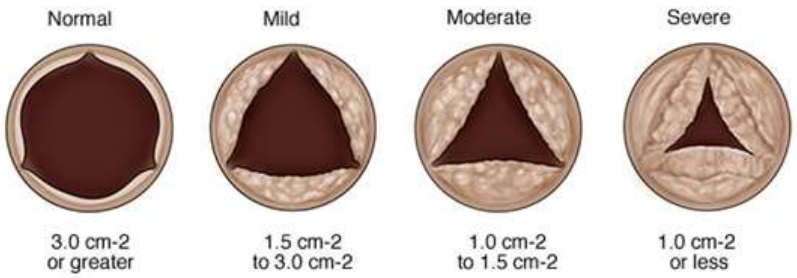

Figure 2.1: Stages in aortic valve stenosis severity (www.mayoclinic.org, 2019)

Figure 2.1 shows the stages of calcification in diseased aortic valve based on the corresponding orifice diameter was shown. The stages show how the valve's geometry or structure change physically. When the valve is severely calcified it does not open and closed properly thereby causing hinderance in ejecting the blood through it and or allowing a backflow (regurgitation) of the blood. It was also established that AS and regurgitation are both predisposed by a congenital bicuspid valve (Michelena et al., 2014)

Aortic valve calcification (AVC) is the most common cause of aortic stenosis (AS) in Western countries, and between 2000 and 2017, the number of people dying from aortic stenosis increased in Europe (Hartley et al., 2021) mostly the elderly, and that made aortic valve disease a serious health challenge.

2.2.2 coronary artery disease

Coronary artery disease (CAD) is one of the main cardiovascular disorders impacting the entire human population. CAD is an inflammatory atherosclerotic disease caused by the coronary artery atherosclerosis or occlusions. Stable angina, unstable angina, myocardial infarction (MI), or abrupt cardiac death are its symptoms (Malakar et al., 2019). Atherosclerosis begins when the endothelial function of the artery wall is disrupted because of the build-up of lipoprotein droplets in the intima of the coronary capillaries (Badimon et al., 2012; Malakar et al., 2019). The development of the atherosclerotic plaque in the coronary artery causes blood flow restriction, which causes an imbalance between myocardial oxygen demand and supply. This obstruction causes the substernal discomfort, weight, and pressure that might radiate to the jaw, shoulder, back, or arm, which are all signs of CAD. The common causes of these symptoms, which often linger for several minutes, are a large meal, emotional stress, physical exercise, or a cold. These sensations could be alleviated in a matter of minutes with rest or nitroglycerin (Cassar et al., 2009).

However, CAD's risk factors and management were intensively researched and coronary angioplasty, also known as percutaneous coronary intervention, is used for the treatment. This technique is used to unblock a clogged artery fast during a heart attack and lessen the damage to the heart. In order to temporarily widen the artery, a tiny balloon must be temporarily inserted and inflated where the artery is blocked (Parisi et al., 1992). Chest pain and shortness of breath are two signs of blocked arteries that are lessened by the angioplasty.

However, a tiny wire mesh tube called a stent can also be permanently inserted to maintain the artery open in order to reduce the likelihood of arterial constriction occurring again. Drug-

eluting stents and bare metal stents are the two main types of stents used to maintain the artery open (Serruys et al., 2006).

2.2.3 Mortality rate due to CVDs

Cardiovascular disorders are typically more prevalent in older persons, with alarmingly high rates of aortic valve disease. According to Bach et al., 2007, estimated that about 5.8 million US adults had aortic valve disease in 2016 of which 5.2 million are aged 65 and above (Bach et al., 2007). In the United Kingdom however, the population for those suffering from a fatal heart disease was estimated at approximately 300,000 in 2019. The research projected that, 291 448 men and women aged 55 in the UK had severe AS in 2019 with a point prevalence of 1.48 percent. Of these, 68.3% (199 059) would have been symptomatic and more easily treated in accordance with their surgical risk profile, with the remaining 31.7% of instances (92 389) being asymptomatic (Strange et al., 2022).

This has no doubt indicates that heart valve diseases posed a serious health threat to human, especially the elderly, and its treatment has equally posed a serious economic burden. In the United State about 200 billion UD dollar is being spend annually for treating one of the heart diseases (coronary artery disease). Therefore, mitigating or controlling the prevalence of this heart valve diseases is paramount to say the least.

2.3 Studies on cardiovascular diseases

Numerous in-vitro and in-silico studies have been conducted on cardiovascular disorders. In this subsection, we'll cover a few of these studies that focus on two specific illnesses: aortic valve disease and coronary artery disease.

2.3.1 Effect of calcification

As mentioned previously, calcification or AVC is one of the AVDs which occur due to calcium deposit and resulted into fusion of the valve's leaflet (aortic stenosis). This makes the tricuspid valve to behave in similar way with the congenital bicuspid aortic valve (CBAV). This can be said, in broader term, that the calcification has an advent effect on the geometry of the AV. This effect resulted into narrowing of the valve orifice diameter thereby making it difficult to pump the blood through the narrow path and consequently result into high pressure build up. Therefore, mechanical stress experienced on the valve and the flow velocity can be used as an indicator and assessment tool for determining the severity of AVC.

2.3.1.1 Mechanical stress

The geometry distortion of the valve leads to an overbearing stress on the leaflets. As we said that like CBAV like the severely calcified tricuspid aortic valve (TAV), and the valve orifice area in the fully open position of the CBAV is significantly smaller than that of the healthy tri-leaflet valve. However, the two types of leaflets CBAV and TAV became similar in characteristics when the latter become severely calcified. Therefore, it was found that the geometrical variations in the AV due to calcification may be a potential risk factor inducing calcific aortic stenosis, which is common in CBAV patients and the changes in geometry resulted in large changes in in-plane strain and stress (Jermihov et al., 2011). This occurred due to the changes in the valve's diameter which makes it smaller, like that of CBAV. Jermihov et al., 2011 computed the maximum in-plane stress for a simulated tricuspid and bicuspid valves (TAV and CBAV) at fully opened and fully closed and found result as shown in Figure 2.2 and 2.3.

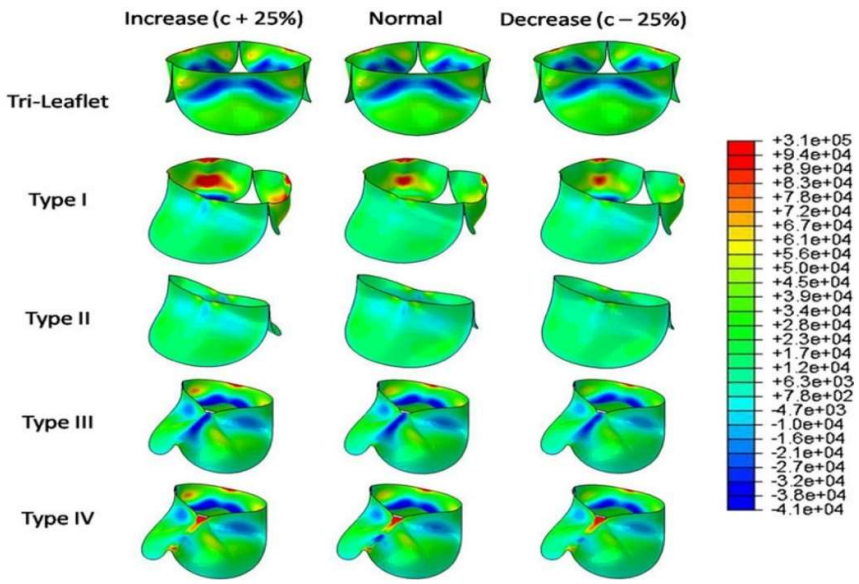

Figure 2.2. In-plane principal stress (N/m^2) for the tri-leaflet aortic valve and simulated CBAVs with leaflets in the fully opened configuration (Jermihov et al., 2011)

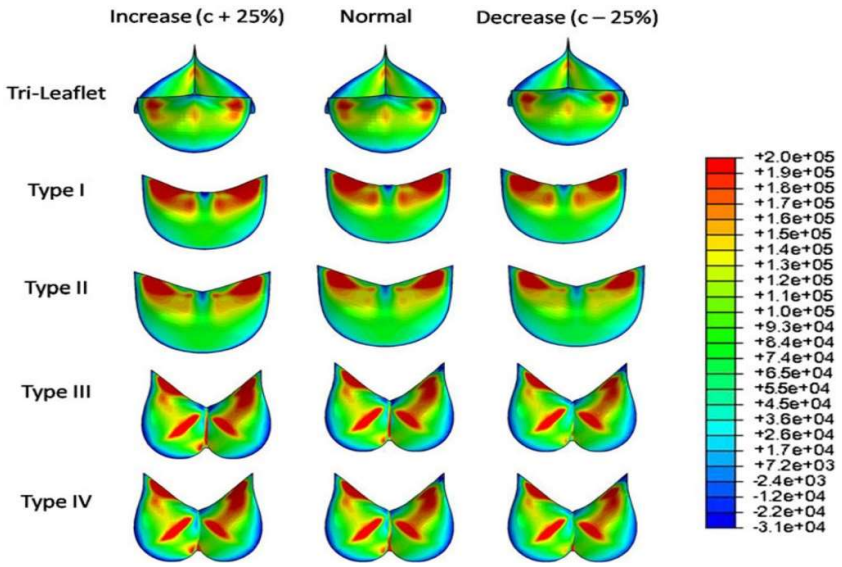

Figure 2.3. In-plane principal stress (N/m^2) for the tri-leaflet aortic valve and simulated CBAVs with leaflets in the fully closed configuration (Jermihov et al., 2011).

This shows that the stress increases as the valve geometry changes from TAV to CBAV and from opened to closed.

Another research was carried out by Huntley et al., 2018 to investigate the differences and similarities in the CBAV and TAV stenosis that occur at the same age, and whether any differences influence outcomes following aortic valve replacement (AVR). It was found that, when compared to patients of the same age with BAV stenosis, TAV stenosis was associated with a higher prevalence of cardiovascular risk factors and a greater degree of cardiac impairment (Huntley et al., 2018).

2.3.1.2 Flow velocity as indicator of severe aortic stenosis

Blood flow through the valve (transvalvular flow) is significantly affected when the valve is malfunctioned or diseased. The aortic valve stenosis can be assess based on the transvalvular flow rate. As the orifice diameter of the valve narrows, the transvalvular flow also decreases. This indicates the link between the valve area and the flowrate. Therefore, the flowrate can be used to measure the orifice diameter, severity of the stenosis and in turn, the mechanical stress on the leaflets due to stenosis. A flow rate of 250 mL/s was used by (Blais et al., 2001; Bermejo et al., 2004; Blais et al., 2006) as the standard value for measuring stenosis. It was found that any values greater than or equal 250 ml/s is acceptable for a normal valve whereas values between 250 and 200 ml/s are consider to be severely stenosed aortic valve, and flow rate less than 200 ml/s signifies high severity with low chances of survival (Blais et al., 2006; Saeed et al., 2017; Vamvakidou et al., 2017, 2019). Figure 2.4 shows the rate of survival of patients suffering from aortic valve stenosis based on the blood flow rate, after days of follow-up.

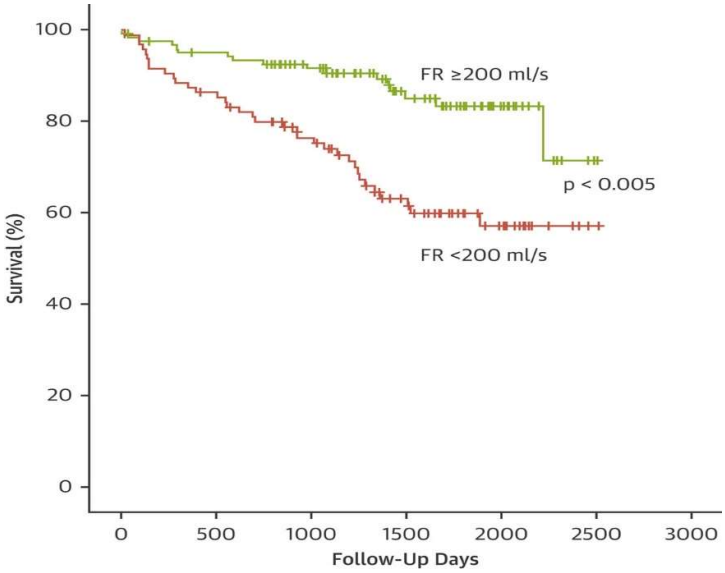

Figure 2.4. Survival curves for patients with abnormal aortic flow rate due to stenosis (Vamvakidou et al., 2019)

2.3.2 Flow within a stented artery

Blood flow through arteries closer to or further from the heart can be impacted by a variety of vascular artery diseases. The most vulnerable arteries to atherosclerosis, which is caused by an accumulation of atheromatous plaques in the artery walls, are the coronary arteries. A medical intervention is necessary in cases of partial or complete lumen obstruction to restore normal blood flow and prevent future problems (Mullany, 2003). Stenting offers certain advantages over alternative therapies because it doesn't involve surgery, has less side effects, less pain, and recovers more quickly (Balossino et al., 2008). The two main therapies for blocked or narrowed arteries caused by CAD are coronary artery bypass grafts (CABG) and percutaneous coronary interventions (PCI).

Vascular stents, which resemble tiny cages, are used to restore blood flow in stenosed blood arteries (i.e., vessels that have been narrowed by illness or dysfunction). These stents have found useful in a variety of applications, with percutaneous coronary intervention being one

of the most popular (Gott et al., 2015). With coronary stent intervention, the flow in coronary arteries that have become restricted due to the build-up of atherosclerotic plaque is restored.

Stents offer a less invasive alternative to traditional revascularization techniques, such bypass grafting, in certain applications. A small incision in the groyne or arm is used to insert a crimped (or collapsed) stent mounted on a deflated balloon catheter into the body in order to access the vasculature. This has been accomplished by using a catheter-based deployment technique. The stent is then directed intravascularly to the target lesion and deployed by balloon inflation, which dilates the vessel, compresses the plaque, and expands the stent into juxtaposition with the vessel's inner wall. In spite of this, the coronary artery stenting is frequently utilised for the treatment of coronary stenosis, and varied stent structures (geometries) do actually have diverse effects on the stress distribution inside the plaque and artery as well as the local hemodynamic environment (Wei et al., 2019b).

Therefore, the geometric design of the many stents utilised in clinical practise now serves as a defining characteristic for the selection of the stent type. An ideal stent should cause less damage to the artery when being expanded, have sufficient radial strength to give strong arterial support after expansion, high flexibility for simple manoeuvrability during deployment, and, for drug eluting stents, should release enough drug in the arterial tissue. These goals are frequently in conflict with one another in any stent design, so that achieving one goal better often necessitates a compromise of another goals (Pant et al., 2012).

There are varieties of stent structures/geometries being used. However, two key parameters for the stent structure, namely stent dogboning and stent recoiling, are to be consider during selection. Wei et al. (2019) studied six different stent geometries, namely- PS-shaped, XP-shaped, C-shaped, C-Rlink, C-Rcrown and C-Astrut and analysed the percentage rate of stent

dogboning and recoiling as well as the distribution of maximum principal plastic strain for the six stents after implantation as shown in Figure 2.3 and 2.4 (Wei et al., 2019b). These figures demonstrate how changes in geometry affect the properties of the stent after deployment, and they can be used as guide to choose geometries that will provide the needed attributes for a given usage or purpose. The dogboning (*DB*) and the recoiling (*RC*) ratio are defined as,

$$DB = \frac{D_{max,end} - D_{min,central}}{D_{max,end}} x100\% \quad (2.1)$$

where $D_{max,end}$ is the maximum stent diameter at the end (distal and proximal), and $D_{min,central}$ is the minimum stent diameter at the centre. And

$$RC = \frac{D_{max} - D_{unload}}{D_{max}} x100\% \quad (2.2)$$

where D_{max} and D_{unload} are mean diameters of the middle cross-section of the stent in the holding and unloading phases, respectively (Wei et al., 2019b).

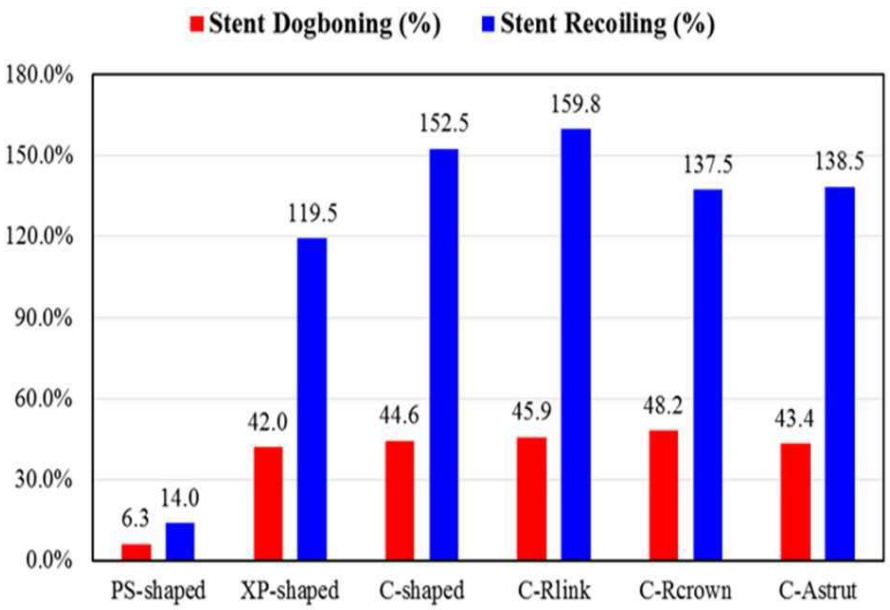

Figure 2.5. Comparison of stent dogbonings and recoilings for six stent structures (Wei et al., 2019b).

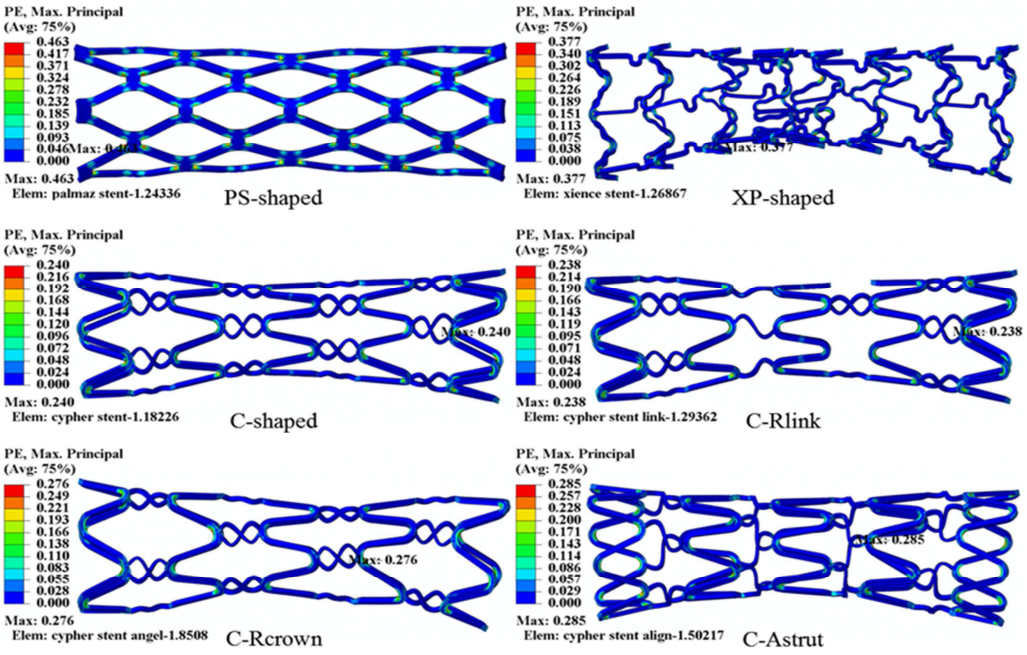

Figure 2.6. The distributions of maximum principal plastic strain for six stents after implantation (Wei et al., 2019b).

2.3.2.1 in-silico models on coronary stents

Computational analysis is proven to be a more and more practical substitute for expensive experimental design and testing of stents and therefore served as a key technique used in the design and deployment of stents nowadays. There are numerous literatures on computational studies involving stents (Serruys et al., 2006; Chinikar and Sadeghipour, 2014; Colombo et al., 2002; Di Venuta et al., 2017; Duraiswamy et al., 2005; Everett et al., 2016; Finet and Rioufol, 2012; Jiménez and Davies, 2009; Khalilimeybodi et al., 2020; Kolodgie et al., 2007; Lally et al., 2005; Lüscher, 2018; Moravej and Mantovani, 2011; Murphy et al., 2003; O'Brien et al., 2010; Stone et al., 2004; Wall et al., 2018; Wiesent et al., 2019). In previous researches, the deployment of stents in cylinder-shaped, straight arteries has been modelled (Lally et al., 2005; Walke et al., 2005). However, as demonstrated in the work of Mortier et al., 2009, it is crucial to also take into consideration additional distortion brought on by deployment in more intricate vascular geometries, including arterial bifurcations (Harewood et al., 2010). Therefore, the morphological and functional assessment of coronary artery disease in the catheterization laboratory could be guided by computational simulations to guide percutaneous procedures. As a result, computational stenting may also describe the local biomechanical milieu before and after stenting. This allows for the optimization of bifurcation stenting and the creation of novel theories that can be tested in real-world settings (Zhao et al., 2021).

Moreover, aside the geometry, stents are also made up of different materials. These includes Bare-metals, metal alloys and polymers. With the invention of coronary bare-metal stents (BMS) in 1986, Sigwart and Puel achieved significant strides in PCI (Morice et al., 2002). Balloon angioplasty is used to inflate BMS, which are cylindrical metal wire meshes that stay in place after the surgery. They are intended to maintain arterial patency following balloon inflation. BMS were created in order to lower the high rate of restenosis following balloon

angioplasty (Stevens et al., 2021). However, it has been discovered that there are a number of issues with inserting a stent with a metal-based scaffold into an artery. Endothelial damage, activation of the clotting cascade, platelet aggregation, and perhaps the development of a blood clot can all result from the interaction between bare-metal stent struts and endothelium (in-stent thrombosis or IST (Buccheri et al., 2016). When a stent is expanded, vascular smooth muscle cells, which give the artery wall its structural integrity, may also sustain injury. This results in vascular smooth muscle cell proliferation and migration to the surface of the endothelium, a condition described as "neointimal hyperplasia" (Ribeiro and Otto, 2014). Neointimal hyperplasia may shrink the size of the artery lumen, which raises the risk of in-stent restenosis (ISR).

Drugs Eluding Stents (DES) were introduced to reduce the problems of bare-metal stents. DES's growth progressed throughout several generations. A metallic stent, a polymer-based drug delivery platform, and a pharmacologic agent (usually an immunosuppressant and/or an antiproliferative substance) make up DESs. The objective of DES technology is to reduce vascular inflammation and cellular proliferation brought on by PCI, hence lowering ISR. The stainless-steel scaffolding of first-generation DES was coated with paclitaxel or sirolimus. First-generation DES were examined in the trials SIRIUS, RAVEL, and TAXUS (Morice et al., 2002, 2007). The second-generation DES carried either everolimus or zotarolimus because research demonstrated the advantages of rapamycin medicines (Mauri et al., 2010; Senst et al., 2022). The cobalt-chromium scaffolding used in second-generation DES contains various polymer coatings, allowing for decreased strut thickness, more flexibility, higher deliverability, improved biocompatibility, better eluting profiles, and superior re-endothelialization . Second-generation drug-eluting stents, which are presently the most frequently implanted stents, were studied in the ENDEAVOR and SPIRIT trials (Leon et al.,

2010; Mauri et al., 2010; Kandzari et al., 2013). Clinical trials for the third generation of DES using a biodegradable polymer or completely bioabsorbable scaffolds had begun latter (Simard et al., 2014).

However, the development of bioresorbable stents (BRS), often known as "biodegradable" stents, was made in response to the relatively late IST, which was principally brought on by the presence of metal stent struts. Biodegradable polymers are used to create BRS, which is a robust radial scaffold. The possibility of exposed stent struts developing, as with DES, is decreased by the stent's capacity to "disappear" within 12 months following deployment. BRS were created such that by the time the stent struts decay, the atherosclerotic plaque lesion in the artery wall will have healed (Stevens et al., 2021).

Therefore, it can be convincingly said that today, computational models were used for designing and testing of stents of any geometry, material, and type without actual or experimental fabrications. For instance, Schiavone et al., 2017 used the Finite Element modelling technique to simulate an Elixir polymer stent deployment in a damaged artery with direct comparison to Xience steel stent. The crimping process, which is required to attach the produced stent to the catheter, was specifically taken into account in the simulations and direct comparisons of the two stents' mechanical capabilities have been made in terms of radial expansion and stresses in the stent-vessel system. Moreover, the results were also contrasted with those that were produced without taking into account the residual stresses caused by the crimping process as illustrated in Figure 2.5 (Schiavone et al., 2017).

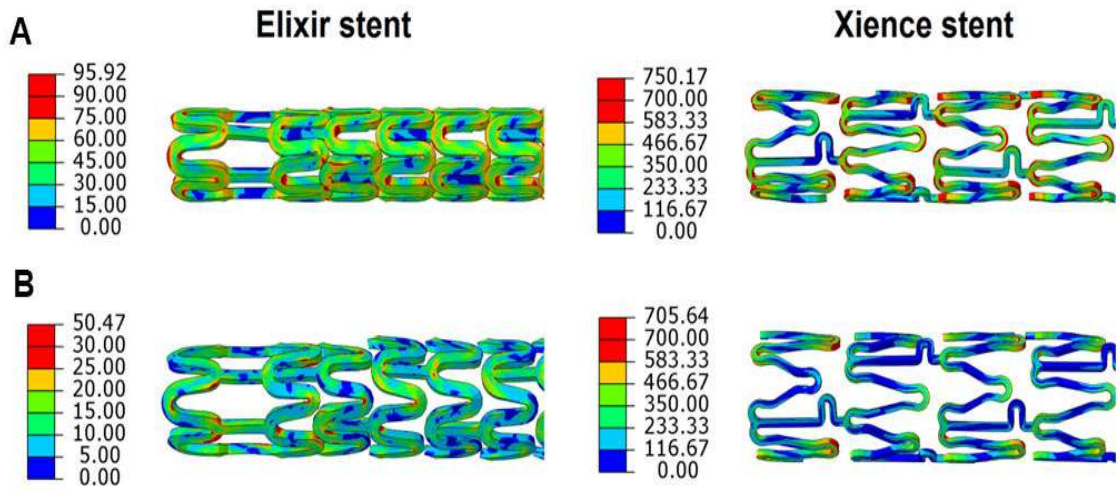

Figure 2.7. Von Mises stress (MPa) contour plot for the Elixir (left) and Xience (right) stents in (A) fully crimped state and (B) spring-back state (Schiavone et al., 2017).

In the other hand, Zhao et al., 2021 used CFD to simulate a completely computational, patient-specific coronary bifurcation stenting to obtain tailored pre-procedural planning that could enhance results. A 3D silicone bifurcation model that had been sliced into rectangular specimens and tested under uni-axial compression served as the basis for the simulation. Stress-strain curves were created from the obtained force-displacement curves. The non-linear stress-strain curve was fitted using the Neo-Hookean hyperelastic model. The shell components of each bifurcation were given a particular thickness to correspond to the real thickness of the silicone models. Compliant, semi-compliant, and non-compliant balloons were each assigned an elastic modulus of 300 MPa, 900 MPa, and 1500 MPa, respectively (Zhao et al., 2021).

Another computational study on stents was the one carried out by Boland et al., based on the Abaqus programme (DS-SIMULIA, USA), and created a computational testbed for stent angioplasty that can simulate stent tracking, balloon expansion, recoil, and in-vivo loading in an atherosclerotic artery model. A surface corrosion model that simulates uniform and pitting

corrosion of biodegradable stents as well as a simulation of the active reaction of the artery tissue after stent implantation, i.e., neointimal remodelling, have also been developed. The simulations of arterial neointimal remodelling with biodegradable stent corrosion show that the mechanical behaviour of degrading stents is significantly influenced by the formation of new arterial tissue around the stent struts (Boland et al., 2016).

In another research by Weisent et al, a non-linear finite element analysis (FEA) software ABAQUS was used to simulate a coronary stent considering different dogboning ratios and asymmetric stent positioning where the results are experimentally validated (Weisent et al., 2019).

2.4 Approach to computational study of CVDs

The *in-silico* experiments are ones that are performed using computer. Therefore, the *in-silico* study of multiphysical problems could be through the use of the traditional mesh-based modelling or the mesh free (particle based) approaches. In addition to that however, two or more particle methods can be combined to form a framework called the DMP which was used intensively for the *in-silico* study of biological systems. In-silico models has advantage over in-vitro models. The main advantage being that the *in-silico* models use fewer resources than models from *in-vitro* and *in-vivo* experiments. Furthermore, in silico models are highly versatile and provide additional insights that are difficult to obtain using common measurement techniques, often at equally unattainable resolutions. However, *in-vitro* models are required to account for all relevant variables that occur in the real world and to generate enough data to inform the development and validation of their digital counterpart.

The concept of the modelling approaches often used to study the CVDs is introduced in the coming sections.

2.4.1 Traditional mesh-based modelling approach

Traditionally, studies using computer simulations are carried out over system domains made of meshed (grid) surfaces. According to Ji et al., (2010), "traditional modelling approaches make use of parametric patches, implicit surface, or subdivision surfaces that have been well integrated into 2D or 3D software". The procedure for mesh-based simulation includes building a geometry, meshing and solution of the model equations using a given software. The system is first translated into a geometry which is latter discretized into mesh of a given size and finally the model, which is normally a differential equation, is solved. After building the geometry the operation is usually carried out in three stages (mesh generation, solution and postprocessing) and this, sometimes, require three independent software to do the job. For example, in computational study of mass transfer at surfaces with reactive nanocones (Mohammed et al., 2019) the geometry and meshing were done by Gmsh software, whereas solution and postprocessing were carried out by Elmer and Paraview, respectively. Each of the stages mentioned above is as important as the other and the error in one stage will significantly lead to an error in the other. However, some software (e.g. COMSOL) were developed in such a way that it can handle all the three operations.

When complex geometries were involved in a quantitative study of a physical phenomenon, numerical methods (such as finite element based) that discretize space are often the best method (Fischbacher and Fangohr, 2009). The procedure for discretization in Multiphysics is not much different with the numerical simulation that is based on partial differential equation discretization.

Therefore, this method is employed in this study to investigate a mass transfer on a conical nano-electrode surface. The complete report may be found in Appendix A, and it serves as a

first step in developing the mathematical modelling and simulation skills needed to use the mesh-free particle technique of modelling.

2.4.2 Particle-based modelling approach

A particle methods or meshfree particle methods (MPMs) generally refer to the class of meshfree methods that employ a set of finite number of discrete particles to represent the state of a system and to record the movement of the system (Liu and Liu, 2003; Capasso et al., 2021). In that regard, each particle is either directly associated with one discrete physical object or constitute and represent part of the continuum problem domain. Some typical MPMs includes Molecular Dynamics (MD), Monte Carlo (MC), Discrete Element Method (DEM), Dissipative Particle Method (DPD), Smooth Particle Hydrodynamics (SPH), etc.

In particle method modelling the movement of the particle that constitutes the system is all according to Newtonian equation of motion.

$$\sum F = ma \tag{2.3}$$

The force F consist of internal and external energy, therefore the equation its derivatives forms become

$$m_i \frac{dv_i}{dt} = m_i \frac{d^2 r_i}{dt^2} = \sum F_E + \sum_{i \neq j} F_{i,j} \tag{2.4}$$

where m_i is the mass of particle i, v_i its velocity, r_i its position, F_E is the external forces, and $F_{i,j}$ the inter-particle force between particle i and particle j.

Particle methods such as SPH, the lattice Spring Model (LSM) which often called Mass Spring Model (MSM), and Discrete Element Method can be link together to study multi-physics problems using a framework called Discrete Multi-Physics.

The internal forces of the particles have different meaning depending on the type of particle method employed. In the Discrete Element method, for example, the internal force is the contact force between two particles. In Smooth Particle Hydrodynamics it can be the viscous and the pressure forces (hydrodynamics forces) between two portions of fluid represented by two (fluid) computational particles. In the lattice Spring Model, the internal forces refer to the elastic forces occurring between two portions of solid represented by two (solid) computational particles deformation forces (Forces between two particles). A typical algorithm for particle-based method is illustrated in Fig.2.8.

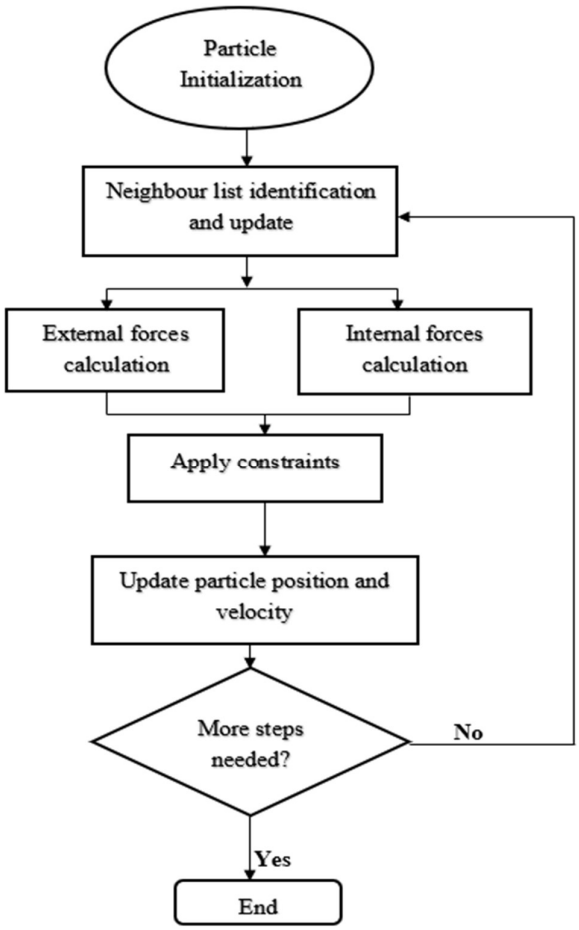

Figure 2.8 Typical structure of particle-based algorithms with internal forces highlighted

The important features of particle methods that, in certain cases, makes them advantageous over the grid-based methods can be summarised as follows (Daxini and Prajapati, 2014; Capasso et al., 2021):

i. No fixed connectivity of the particle at the node as the problem domain is discretised with particles therefore, treatment of large deformation would relatively be much easier.
ii. Complex geometries can be discretised easily with meshfree method as only initial discretization is required.
iii. Obtaining the features of the entire physical system through tracing the motion of the particle is easy with meshfree method, therefore, identifying free surfaces, moving interfaces, and deformable boundaries is no longer a tough task.
iv. Refinement of particle is much easier compared to mesh refinement.

Additionally, many particle methods (e.g. MD, DPD, SPH, LSM, DEM) share the same algorithm (Figure 2.8) and, therefore, it is relatively easy to combine them together in a hybrid simulations. In particular, this thesis used Smooth Particle hydrodynamics for fluid treatment (Gingold and Monaghan, 1977; Liu and Liu, 2003b), and the solid structure uses the Lattice Spring Model (Kot et al., 2015; Kot, 2021). The connection of liquid-solid is done using the Discrete multi-Physics approach (Alexiadis, 2015a).

2.4.2.1 Smooth Particle Hydrodynamics (SPH)

Smooth Particle Hydrodynamics is a mesh-free Lagrangian method developed by Gingold and Monaghan(Gingold and Monaghan, 1977), and Lucy (Lucy, 1977) in 1977 for astrophysics problems to simulate astrophysical three-dimensional problems (Lind et al., 2020). The basic

idea of SPH is to consider the fluid as an ensemble of smooth particle with each particle having a kernel that represent its mass distribution (Di Lisio et al., 1998).

Since its introduction, the areas of application remained limited to space study until 1990's when it was developed in fluid dynamics (Monaghan, 1992; Swegle et al., 1995; Morris et al., 1997) and multifluid problems (Monaghan, 2012). Today the application of SPH has become versatile and span into variety of engineering problems. Recently, SPH coupled with other particle methods such as DEM, LSM and PeriDynamics was used in modelling problems that involved liquid-solid interaction (Ji et al., 2019; Li et al., 2019; Mohammed et al., 2021; Rahmat et al., 2019a), multiphase flow problems (Hopp-Hirschler et al., 2018; Rahmat and Yildiz, 2018), and problems in human biological organs (Ariane et al., 2017a; Schütt et al., 2020a; Alexiadis et al., 2017; Ariane et al., 2018b).

Accuracy and convergence of SPH method has been improve over these years of applications. Careful consideration of factors that can be manipulated to improve the convergence of the method is important. The right choice of SPH formulation for fluid (either incompressible or weakly compressible), setting appropriate boundary conditions, using higher order kernel and manipulation of the truncation error time can improve the convergence of the SPH method (Lind et al., 2020). Today the continuing modifications and improvements made the SPH method reached an acceptable level of practical engineering applications in term of accuracy and stability.

2.4.2.2 SPH set up equations

The SPH method represents the state of a system with particles which possess individual material properties and move according to a governing equation (Liu and Liu, 2003). The fundamental idea behind this discrete approximation lies in the mathematical identity

$$f(r) = \iiint f(r')\delta(r - r')dr' \tag{2.5}$$

which gives a discretized particle approximation within a domain of a smoothing function (kernel) *W* within a characteristic width *h* called the smoothing length (Alexiadis, 2015b) such that

$$\lim_{h\to 0} W(r, h) = \delta(r). \tag{2.6}$$

This gives rise to the discrete approximation

$$f(r) \approx \iiint f(r')W(r - r', h)dr' \tag{2.7}$$

which can be discretised over a series of particle of mass m_i and density ρ_i to obtain

$$f(r) \approx \sum_i \frac{m_i}{\rho_i} f(r_i)W(r - r_i\,, h). \tag{2.8}$$

where *f(r)* is a generic function defined over the volume *V*, *r* is the three-dimensional vector point, and *δ(r)* is the three-dimensional delta function.

Equation (2.8) is a representation of the discrete approximation of a generic continuous field. Further simplification of Equation (2.8) can be done to approximate the Navier–Stokes equation. Therefore, using this approximation, the Navier-Stoke equation can be discretised over a series of particles to obtain:

$$m_i \frac{dv_i}{dt} = \sum_j m_i m_j \left(\frac{P_i}{\rho_i^2} + \frac{P_j}{\rho_j^2} + \Pi_{i,j}\right)\nabla_j W_{i,j} + f_i, \tag{2.9}$$

where v is the particle velocity, t the time, m is the mass, ρ the density, and P the pressure associated with particles i and j. The term f_i is the volumetric body force acting on the fluid and $\Pi_{i,j}$ introduces the viscous force as defined by (Morris et al., 1997). An equation of state is required to relate pressure and density. In this paper, Tait's equation of state is used:

$$P(\rho) = \frac{c_0\rho_0}{7}\left[\left(\frac{\rho}{\rho_0}\right)^7 - 1\right], \tag{2.10}$$

where c_0 and ρ_0 are a reference sound speed and density. To ensure weak compressibility, c_0 is chosen to be at least 10 times larger than the highest fluid velocity. See detail and complete equations in the numerical methodology chapter (Chapter 3).

2.4.2.3 Lattice Spring Model (LSM)

The behaviour of deformable objects can be simulated using the LSM approach. This model consists of mass point and linear springs which exert forces at the nodes located at the end point (Kot et al., 2015), which are placed on either a regular lattice or positioned randomly within the system (Pazdniakou and Adler, 2012). The term LSM is interchangeable with mass spring model (MSM), where the latter is mostly used in computer graphics and the former in solid mechanics. Nowadays, LSM is applicable in many areas and disciplines, for instance, cloth simulation, face animation, or soft tissue behaviour in surgery training systems (Lloyd et al., 2007; Stevens et al., 2003) are simulated using LSM.

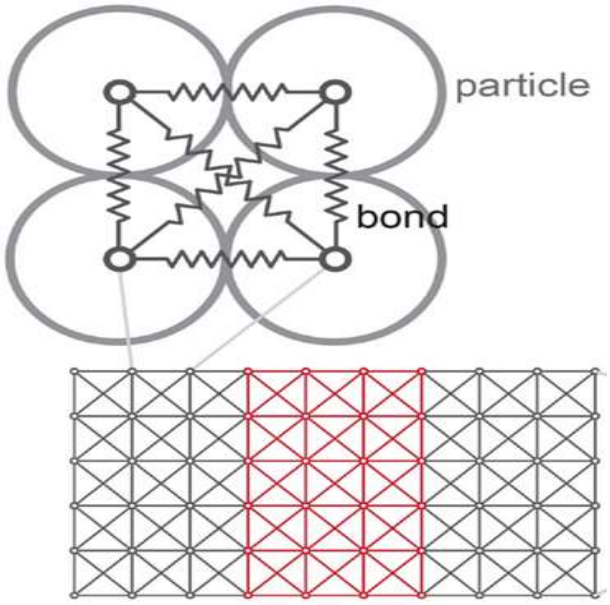

Figure 2.9. Illustration of Lattice Spring Model from its molecular origin (Brely et al., 2015)

The LSM follows the idea that any material point of the body can be referred to by its position vector r = *(x,y,z)* (Pazdniakou and Adler, 2012)..When the body undergo deformation its position changes and the displacement is related to the applied force as:

$$\mathbf{F} = k(r - r_0) \tag{2.11}$$

where **F** is the force, r_0 is the initial distance between two particles, r is the instantaneous distance, and k the spring constant (or Hookean constant).

According to (Kot et al., 2015), in a regular cubic lattice structure, the spring constant is related to the bulk modulus of the material by

$$K = \frac{5}{3}\frac{k}{r_0} \tag{2.12}$$

And

$$E = \frac{3}{2}K \tag{2.13}$$

where K is the bulk modulus, E the young modulus, r_0 is the initial particle distance and k the spring constant.

From Equations (2.12) and (2.13) the spring constant is then related to the young modulus of the material by

$$k = \frac{Er_0}{2.5}. \tag{2.14}$$

2.4.3 Discrete multi-physics

Several computational studies using particle-based methods were presented, including Smooth Particle Hydrodynamics (SPH), Discrete Element Method (DEM), Lattice Spring Model (LSM), and others. Particle methods can be used to solve a wide range of problems that appear to be very different on the surface. SPH, for example, is frequently used to model hydrodynamics problems, as well as LSM solid mechanics and DEM real particles. Despite

these differences, they all use the same algorithm (DISCRETE MULTIPHYSICS: modelling complex systems with particle methods., 2021).

Computational particles represent real particles (e.g., DEM) or discrete portions of liquid (e.g., SPH) or solid (e.g., LSM) matter in the computational domain. These particles move due to the exchange of forces between them. The type of physical phenomena represented by the forces distinguishes different particle methods. For example, in SPH, they represent pressure and viscous forces in fluids; in LSM, elastic forces in solids; and in DEM, Hertzian contact forces between real particles.

2.5 DMP modelling approach at the cutting-edge

The vascular flow problems such as aortic valve disease and stenosed coronary artery stenting can equally be tackled using a discrete multiphysics modelling approach. In that approach the mesh-free Discrete Multiphysics technique relies on "computational particles" rather than computational meshes, in contrast to traditional Multiphysics. It is a hybrid strategy that integrates many particle approaches, including Smoothed Particle Hydrodynamics (SPH), Lattice-Spring Model (LSM), and Discrete Element Method (DEM). It has become clear that discrete multiphysics is more than merely a substitute for classical multiphysics. DMP solves a number of problems that are extremely challenging, if not impossible, for conventional multiphysics.

Therefore, in DMP the user decides, before to the simulation, which parts of the domain belong to the solid domain and which parts to the fluid domain. This decision cannot be changed while the simulation is running in traditional multiphysics. In DMP, the distinction between solid and fluid is solely determined by the type of force supplied to the computational particles. By altering the type of force, we may change the behaviour of the computational particles during

the simulation from solid to liquid and vice versa (Alexiadis, 2019). This flexibility gives discrete multiphysics a distinct advantage in a number of situations, including cardiovascular flows with blood aggregation (Ariane et al. 2017a; Ariane et al. 2017b, Ariane et al. 2018a), capsules and cell breakage (Alexiadis 2015b, Rahmat at al. 2019a), dissolution problems (Alexiadis 2015a, Rahmat et al. 2019b), and phase transitions (Alexiadis 2018).

Moreover, several in-silico models of the human proximal colon have been developed in recent years using the DMP technique (Alexiadis et al., 2017; Schütt et al., 2022; Alexiadis et al., 2021). the colon serves many purposes, including digestion and waste elimination. It is divided into five sections, each of which absorbs water and nutrients, solidifies stool, and transports waste to the rectum. The colon also houses the majority of the gut's microorganisms, which aid in the breakdown of material that the body cannot digest on its own. Some parts of the colon, such as the appendix and paracolic gutters, are still unknown to scientists. Hydrodynamics of colon is also one thing that requires the attention of research for an effective drugs administration and absorption.

This approach has also been applied recently to the pharmaceutical field, where it was used to model drug release from a solid dosage form under the influence of various in vivo motility patterns (Schütt et al., 2020). Colon-targeted drug delivery has received increased attention in recent years, due to regional conditions that provide advantages for the delivery of certain types of pharmaceutical formulations, compared to the small intestine. The hydrodynamics of the proximal colon are critical for the design and optimization of colon-targeted formulations, especially in terms of disintegration, dissolution, and distribution of the dosage form (Schütt et al., 2022). According to Alexiadis et al., 2017 a model that predicts drug concentrations at the colon's surface is likely to correlate with drug performance because this is the site of

absorption for systemically absorbed drugs or the site of action for many drugs used for local targeting within the colon.

2.6 Summary

This chapter focused on cardiovascular illnesses and how computational studies are used to control and track the disease's progression. Previous research on coronary artery stenting and aortic valve calcification is reviewed. Additionally, a particle-based modelling strategy has been examined as a viable strategy for the investigation of these CVDs. The DMP framework and its state-of-the-art on the research of vascular flow, pharmaceuticals, and human organs was also discussed.

2.7 Notations and abbreviations

Notations

m	mass [Kg]
ρ	Density [Kg m^{-3}]
c_0	Sound speed [m s^{-1}]
P	Pressure [N m^{-2}]
u	Fluid velocity [m s^{-1}]
v	Kinematic viscosity [P.sa]
g	Gravity [m s^{-2}]
W	Kernel function [m]
h	Smoothing length [m]

r	Distance [m]
V	Volume [m^3]
k	Spring constant [N m^{-1}]
K	Bulk Modulus
F	Force [N]
E	Young modulus [N m^{-2}]
t	Time [s]

Abbreviations

DMP	Discrete Multiphysics
MRI	Magnetic Resonance Imaging
CVD	Cardiovascular Disease
AVD	Aortic Valve Disease
AS	Aortic Stenosis
AVR	Aortic Valve Regurgitation
AVT	Aortic Valve Thickening
AVC	Aortic Valve Calcification
CAD	Coronary Artery Disease
MI	Myocardial Infarction
CBAV	Congenital Bicuspid Aortic Valve

TAV	Tricuspid Aortic Valve
BAV	Bicuspid Aortic Valve
CABG	Coronary Artery Bypass Grafts
PCI	Percutaneous Coronary Interventions
BMS	Bare Metal Stent
IST	In-Stent Thrombosis
ISR	In-Stent Restenosis
DES	Drugs Eluding Stent
BRS	Bioresorbable stent
FEM	Finite Element Method
FEA	Finite Element Analysis
MPM	Meshfree Particle Method
MD	Molecular Dynamics
MC	Monte Carlo
DEM	Discrete Element Method
DPD	Dissipative Particle Method
SPH	Smooth Particle Hydrodynamics
MSM	Mass Spring Model
LSM	Lattice Spring Model

CGMD	Coarse Grained Molecular Dynamics
DMP	Discrete Multi-Physics
CFD	Computational Fluid Dynamics
FSI	Fluid Structure Interaction

CHAPTER THREE: NUMERICAL METHODOLOGY

3.0 Numerical Methodology

In this study, a mesh-free particle approach of simulation was employed, where two particle methods—Smooth Particle Hydrodynamics (SPH) and Lattice Spring Model (LSM)—were combined to create a framework known as DMP. In the next sections, the simulation setups and the model governing equation are described.

3.1 SPH formulation

The general idea of SPH is to approximate a partial differential equation over a group of movable computational particles that are not connected over a grid or a mesh (Ruiz-Riancho et al., 2021).

The method's formulation starts with the identity

$$f(r) = \iiint f(r')\delta(r - r')dr', \tag{2.5}$$

where $f(r)$ is a generic function defined over the volume, *r* is the position where the property is measured, and $\delta(r - r')$ is the Dirac delta function. In SPH, the delta function is approximated by a bell-shaped smoothing Kernel function W over a characteristic width h (smoothing length), which satisfies the following conditions called normalisation condition, delta function or limit condition, and compact condition.

$$\iiint W(r - r', h)dr' = 1 \qquad \text{(Normalisation condition)} \tag{3.1}$$

$$\lim_{h \to 0} W(r - r', h) = \delta(r - r') \qquad \text{(Limiting condition)} \tag{3.2}$$

$$W(r - r', h) = 0 \qquad \text{when } |r - r'| \geq h \qquad \text{(Compact condition)} \tag{3.3}$$

Note that the compact condition expresses the area of effectiveness of the smoothing function. The smoothing length h determines the size of the neighbouring domain (Fig. 3.1).

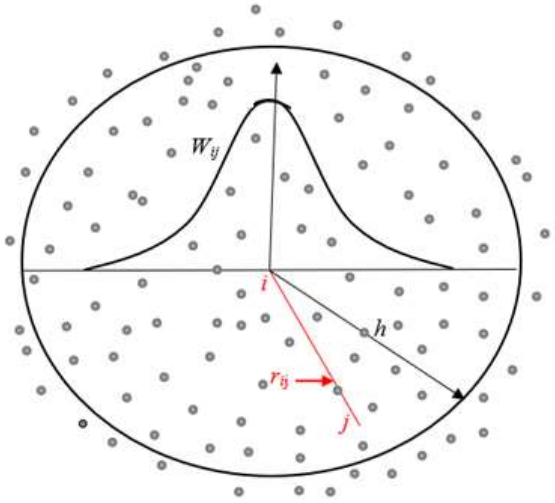

Figure 3.1: Domain of the smoothing kernel function *Wij*, with the smoothing length *h*

Figure 3.1 Domain of the smoothing kernel function W_{ij}, with the smoothing length h

Substituting δ with W in Eq. 3.3 brings to

$$f(r) \approx \iiint f(r')W(r-r',h)dr', \tag{2.7}$$

which can be discretised over a series of particles of mass $m=\rho(r)\mathrm{d}r$ to obtain

$$f(r) \approx \sum_i \frac{m_i}{\rho_i} f(r_i)W(r-r_i,h), \tag{2.8}$$

where m_i and ρ_i are the mass and density of the i^{th}particles, and i ranges over all particles withing the smoothing Kernel.

3.1.1 Smoothing Kernel function

In SPH formulation, the kernel function W is very important because it determines the pattern to interpolation. The kernel function is closely related to the computational accuracy and stability of the SPH method (Yang et al., 2014). Several kernel function were used in literatures such as the Lucy form (Lucy, 1977), the exponential form (Gingold and Monaghan, 1977), the cubic and quadratic spline (Monaghan, 1992; Morris et al., 1997), double cosine kernel function (Yang et al., 2014), among others.

There seems to be no consensus on which kernel function is more adaptable. Monaghan, (1992) said that the exponential form of kernel function is most adaptable and is a rule of thumb for stability and accuracy in SPH. However, Belytschko et al., (1996) has a contrary argument that the exponential form has no significant advantage over a spline form. Several other kernel functions were used in literature ((Liu and Liu, 2003; Morris et al., 1997; Fulk and Quinn, 1996; Yang et al., 2014) and each one said to have it certain advantage in terms of stability and accuracy. Therefore, as mentioned earlier, the original Lucy form of smoothing kernel function is used in this work as it was already used successfully for simulating water flow (Lucy, 1977) as well as cardiovascular flow with similar geometries and condition (Ariane et al., 2017a).

$$W(r - r_i, h) = \lambda_d \left[1 + 3\frac{|r-r_i|}{h}\right]\left[1 - \frac{|r-r_i|}{h}\right]^3 \quad \text{for} \quad |r - r_i| < h \tag{3.4}$$

$$W(r - r_i, h) = 0 \qquad \text{for} \qquad |r - r_i| \geq h \tag{3.5}$$

3.1.2 Fluid dynamic Equation

The newton equation of motion in its discrete form (eqn. (3.2)) can be approximated in Lagrangian form eqn. (3.11) and eqn. (3.12) which is continuity density with each particle represented by its mass, pressure, density, and velocity.

$$m_i \frac{dv_i}{dt} = \sum_j m_i m_j \left[\frac{P_i}{\rho_i^2} + \frac{P_j}{\rho_j^2}\right] \nabla_j W_{i,j} + \sum F_E, \tag{3.6}$$

$$\frac{d\rho_i}{dt} = \sum_j m_i v_{i,j} \nabla_j W_{i,j}. \tag{3.7}$$

This can be extended to approximate the Navier-Stoke equation discretised over a series of particles to obtain:

$$m_i \frac{dv_i}{dt} = \sum_j m_i m_j (\frac{P_i}{\rho_i^2} + \frac{P_j}{\rho_j^2} + \Pi_{i,j}) \nabla_j W_{i,j} + f_i, \tag{2.9}$$

where v is the particle velocity, t the time, m is the mass, ρ the density and P the pressure associated with particles i and j. The term f_i is the volumetric body force acting on the fluid and $\Pi_{i,j}$ introduces the viscous forced as defined by (Morris et al., 1997). An equation of state is required to relates pressure and density.

3.1.3 Weak compressibility and artificial viscousity

The Navier-Stoke equation can be written in Lagrangian form as

$$\frac{du}{dt} = \frac{1}{\rho} \nabla P + v \nabla^2 \mathbf{u} + \boldsymbol{g} \tag{3.8}$$

and the continuity equation as

$$\frac{d\rho}{dt} = -\rho \nabla . u \tag{3.9}$$

Where **u** is the fluid velocity vector, ρ is the fluid density, t is time, P is fluid pressure, v is kinematic fluid viscosity and **g** is the gravity.

A stiff equation of state is often used for weak compressibility SPH formulation. Hence the equation of state relates fluid pressure to changes in density via

$$P = \frac{c_0^2 \rho_0}{\gamma}\left(\left(\frac{\rho}{\rho_0}\right)^{\gamma} - 1\right). \tag{3.10}$$

where c_0 and ρ_0 are a reference sound speed and density.

However, Monaghan (1994) used the artificial Tait's equation of state for simulating a free surface water flow, where γ in eq. (3.16) is equal 7

$$P = \frac{c_0^2 \rho_0}{7}\left(\left(\frac{\rho}{\rho_0}\right)^{7} - 1\right), \tag{2.10}$$

To ensure weak compressibility, c_0 is chosen to be at least 10 times larger than the highest fluid velocity. Since equation of state is needed to relate density with pressure, therefore, Tait's equation of state (eqn. 3.17) is used in this work.

3.2 Young modulus and the spring constant for LSM

For a regular cubic lattice structure, the spring constant is related to the bulk modulus of the material, according to Kot et al., (2015) as follows:

$$K = \frac{5}{3}\frac{k}{r_0} \tag{2.12}$$

And

$$E = 3K(1 - 2b) \tag{3.11}$$

where K is the bulk modulus, E the Young modulus, r_0 is the initial particle distance and k the spring constant and b the poison ratio.

For 3D spring model (cubic lattice), the Poison's ratio b is constrained to 0.25 (Kot et al., 2015) and equation (3.11) becomes

$$E = \frac{3}{2} K. \tag{2.13}$$

and,

$$k = \frac{Er_0}{2.5}. \tag{2.14}$$

For any given value of E, the k can be evaluated and used as the spring constant in the particle simulation.

3.3 Coupling of SPH-LSM: The Discrete Multiphysics framework

Two or more particle methods can be combined within a discrete Multiphysics (DMP) framework. In this thesis, the Multiphysics problems were modelled using a DMP framework consisting of SPH and LSM. Fluid is represented by SPH and the solid by LSM. In DMP, there are different types of interactions viz: interaction between liquid-liquid of the SPH particles; solid-solid interaction by LSM where each particle is linked to another by means of bonds between them, and the solid-liquid interaction at the solid interface when the two models are combined.

These interactions were presented schematically in Fig. 3.2. The interactions are type 1, 2, and 3 which were represented by SPH, LSM, and Lennard-Jones potential model (a boundary condition discussed in section 3.3.2), respectively

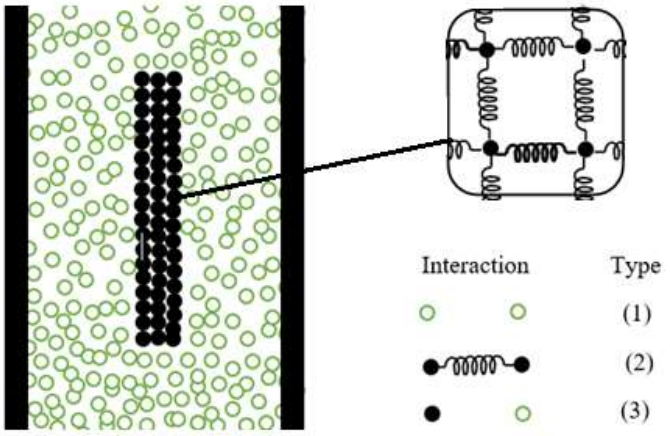

Figure 3.2: Types of interactions occurring between elemental particles

The interaction of solid-liquid at solid interface is used to define the solid boundary condition (section 3.3.2).

3.3.1 Initial Particle distribution

Particle distribution is generated using GMSH software where the geometry with the mesh is built. Then a MATLAB code is used to give an exact replica of all the coordinates and points of the already built geometry. These coordinate and points translate into particle in LAMMPS and the geometry if formed of particle (Fig.3.3b). For complex geometries, commercial software such as Salome or GAMBIT can be used to build the geometry and the associated mesh is then replaced with particles.

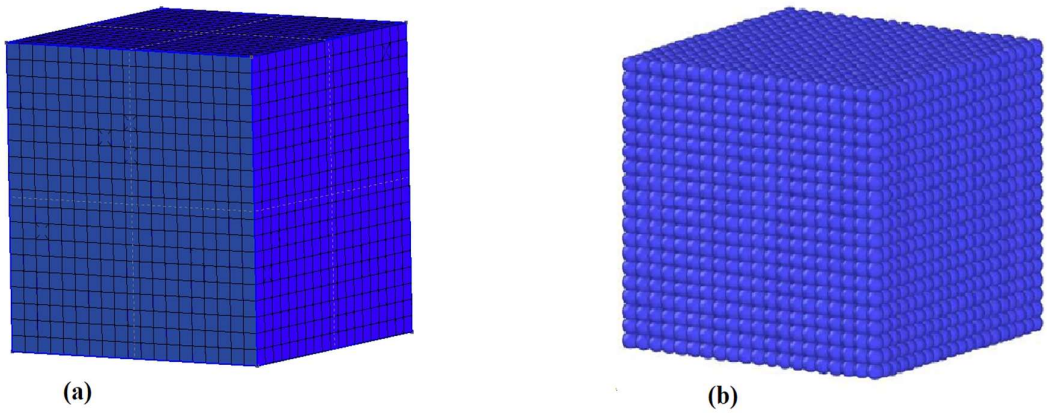

Figure 3.3: A cubic geometry with (a) structured mesh, and (b) particles

3.3.2 Boundary conditions

Interaction forces is used in particle method to implement a boundary between solid and liquid particles. The forces (interaction forces) define the behaviour of the two distinct materials at the solid-liquid interface.

$$\left(\frac{\partial}{\partial t}u - v\right).\boldsymbol{n} = 0 \text{ (no penetration)} \tag{3.12}$$

$$\left(\frac{\partial}{\partial t}u - v\right)\text{x}\boldsymbol{n} = 0 \text{ (no slip)} \tag{3.13}$$

Newton's Third Law demands the continuity of stresses which means that the traction forces of solid g_f must be opposite to the traction forces of the fluid g_s on the boundary

$$g_s = \sigma_s.\boldsymbol{n} = \sigma_f(-\boldsymbol{n}) = -g_f \text{ (Continuity of stress)} \tag{3.14}$$

Where n and -n are the outward normal on solid and fluid respectively (Müller et al., 2004).

To enforce the boundary condition of no-penetration and no-slip, a velocity of same magnitude is imposed at the solid-liquid interface of the two materials in mesh-based method, whereas, in DMP framework interaction forces are used instead. Solid boundaries are often modelled

with fixed wall particle and artificial repulsive forces (Violeau and Issa, 2007) with a Lennard-Jones potential kind of interaction.

Artificial repulsive interaction forces are also used in particle method for boundary between solid-liquid and liquid-liquid particles. The Lennard-Jones potential is used such that the force of repulsion between the particle is greater than that of attraction (Ackland and Bonny, 2020), thus imposing no penetration condition between the particles. Therefore, the no-penetration condition is often implemented by means of Lennard-Jones central force which has the form

$$f(r) = Q\left[\left(\frac{r^*}{r}\right)^{m_1} - \left(\frac{r^*}{r}\right)^{m_2}\right]\frac{r}{r^2}, \tag{3.15}$$

Where r^* is the particle's repulsive radius, and m_1 and m_2 usually set to 4 and 2 for liquid-liquid and 12 and 6 for solid-liquid (Monaghan, 1994). The constant Q is often chosen based on the characteristic flow velocity.

For the fixed particle boundary, some particles are stationed as rigid solid wall to provide a blockade and ensure no penetration of particle from within and outside the wall, and that also keeps the conservation laws valid. More than one layer of particle can be used to provide the rigid wall.

3.4 Simulation Setup

To set up the simulation, a number of steps were taken. For DMP model executable in LAMMPS, there are two files generated. These are the Data file where the coordinate and mass of the particles that formed the geometry were written, and the input file where all simulations parameters such as density, viscousity, gravity, velocity, kernel function, etc., and the simulation type were also specified. The coordinate of the geometry is written directly with MATLAB code or sometimes from a preprocessing solver in the case of a complex geometry as described in section 3.4.1.

3.4.1 How to adapt 3D CAD models for Discrete Multiphysics

This section explains how to adapt the 3D CAD model for Discrete Multiphysics. The valve geometry is taken from (Bavo et al., 2016) and was initially created with the help of CAD. In general, particle distribution can be generated with a programming code or a pre-processing solver. In the first case, the coordinates of the points are created with a separate standard programming code such as C++ and MATLAB, or directly in the processing solver with an integrated algorithm (in the software LAMMPS for instance). For complex geometries, a pre-processing commercial builder (GAMBIT, ABAQUS, SALOME) can be used for the structure and the associated mesh is then replaced with particles (Fig. 3.4). For the case of aortic valve geometry, we used the second approach in order to design our tricuspid valve system.

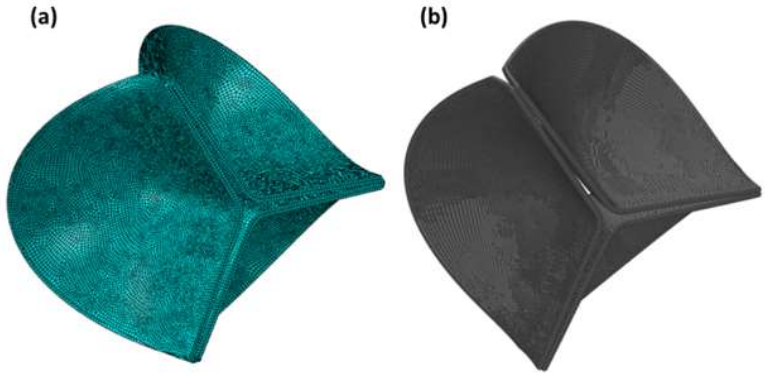

Fig. 3.4: Mesh generation using a pre-processing solver (a) and the generated particle distribution (b).

The procedure of implementation is simple but requires a couple of sequences to obtain the final input file. Here, we present the one used for our valve model, but the methodology can be extended to any other applications.

The different steps can be described as follow:

1. Creation or Importation of the CAD geometry
2. Writing of the data file
3. Generation of the bond and coefficient files
4. Implementation of the input file

The first step consists of designing the part geometry or importing an existing one to any CAD commercial or open-source software (Fig. 3.5a). The idea is to use the software capability for generating automatically or manually the mesh (elements and nodes, Fig. 3.5b). Next, the nodes information (numbers and coordinates) are downloaded (Fig. 3.5c) and collected into a text file (Fig. 3.5d).

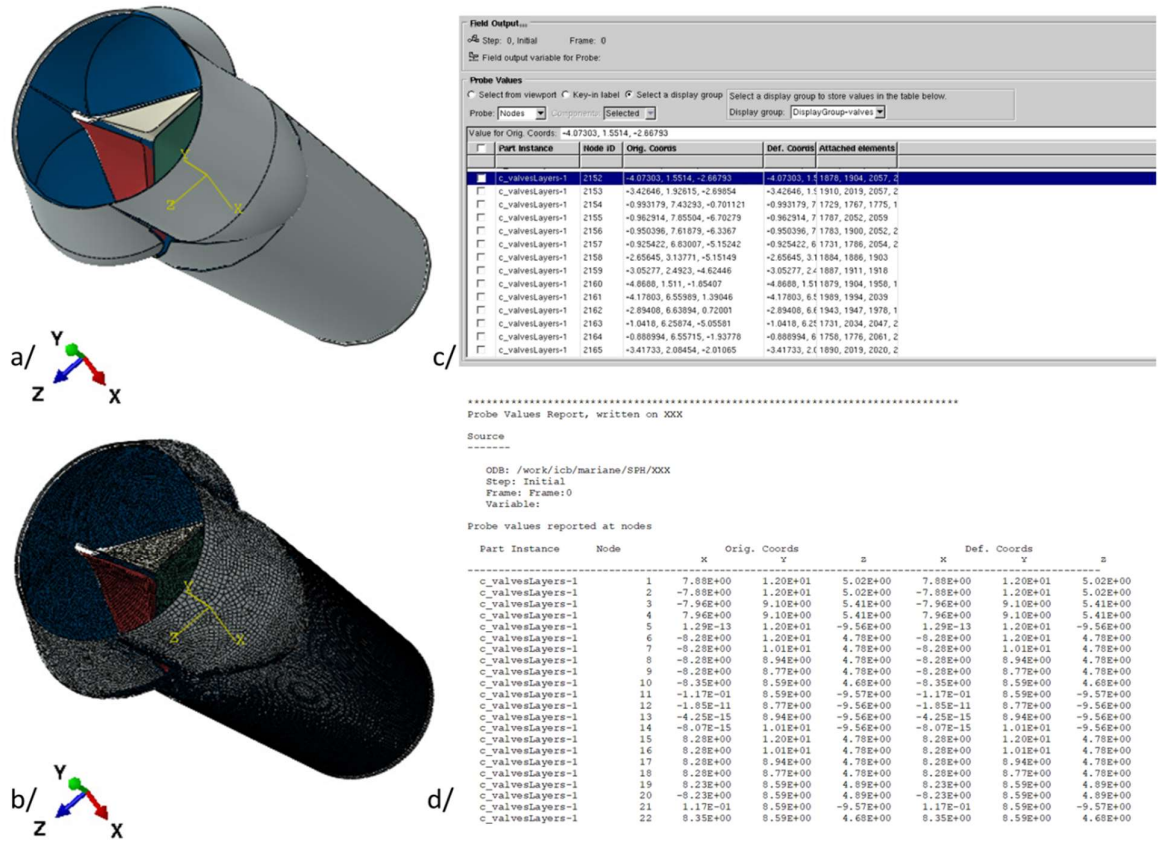

Fig. 3.5: Tricuspid valve CAD part (a), tricuspid valve meshed CAD part (b), nodes generation using the CAD software (c) and external data file (d).

Subsequently, the data file is adapted and implemented in a LAMMPS format file, which contains specific line codes and keywords (for more details and documentation, readers can refer to LAMMPS documentation available at https://lammps.sandia.gov/doc/Manual.html). For instance, for this model, we used the keywords *meso* for the atom style and *bond* for the inter-atomic potential.

The unsymmetrical shape of the tricuspid valve system makes necessary a 3-D design. This representation requires a fine mesh with a consequent number of nodes (418,743 particles) to ensure a realistic valve motion. Each node/particle is connected with at least 3 other nodes located nearby, increasing drastically the data processing. As a result, we developed an

algorithm (C++ code) in order to set automatically the bonds definition. All particle positions are scanned by the code and for each particle, its neighbour (within a prescribed radius distance of interaction) is identified, numbered and printed out in a bond file. Meanwhile, a second file is also created with the storage of the bond coefficients (potential force) and the distance (between 2 particles).

Finally, as the number of fluid particles is very important (342,358), the inclusion of the list into the data file (which it is technically possible) makes heavy the input file processing. Instead, we preferred to generate, during the first step of the simulation, the fluid particles via the LAMMPS commands '*create_atoms'* and '*region*'. The command '*delete*' is also used to avoid overlapping.

Moreover, for the stent geometry, the same technique was employed. After obtaining the particle positions from the pre-processing solve, MATLAB code is then written to create the bond and the bond's coefficient between each particle as in Appendix C2. The program was written and where the initial positions (x, y, and z) of the stent's particle was as excel file with a **'.cvs'** extension. When this is executed in MATLAB two resulting files stent.bonds and Bonds.txt were obtained. The former contained the information about the bond coefficient of all the stent particles whereas the later gives the bond positions. See Appendix C3 and C4 for these files.

3.5 Discrete Multiphysics for Fluid-Structure Interaction

The DMP framework can be used to study a problem involving the interaction between solid and liquid which in other word called Fluid-Structure interaction. As discussed in section 3.3 the fluid and the solid structure are represented by the SPH and LSM particle respectively. This approach is used to study a deformable solid structure within a moving fluid where the

rate of deformation is due to pressure force (solid-liquid interaction) and elastic force (solid-solid interaction). These are presented as case studies in Chapter 4 and 5.

3.6 Summary

In this chapter, the numerical methodology used in this study is presented. The mathematical concepts of meshfree methods SPH, LSM, and DMP were comprehensibly presented. Some characteristics of particle method such as initial particle distribution and boundary conditions were also explained. Phenomenon that relates to FSI and mechanics of material stiffness were also presented briefly.

3.6 Notations and abbreviations

Notations

m	mass [Kg]
ρ	Density [Kg m^{-3}]
c_0	Sound speed [m s^{-1}]
P	Pressure [N m^{-2}]
u	Fluid velocity [m s^{-1}]
v	Kinematic viscosity [P.sa]
g	Gravity [m s^{-2}]
γ	Dumping Coefficient [s^{-1}]
W	Kernel function [m]
h	Smoothing length [m]

r	Distance [m]
r*	Particle radius [m]
D	diffusivity [$m^2\ s^{-1}$]
t	time [s]
∇	Laplacian operator [-]
∇^2	Laplacian operator (sum of second partial derivatives) [-]
F/f	Force [N]
K	Bulk Modulus [$N\ m^{-2}$]
k	Spring constant [$N\ m^{-1}$]
v	Poisson's ratio [-]
E	Young modulus [$N\ m^{-2}$]
$g_{s/f}$	Traction force (solid/fluid) []
n	Normal Vector [-]

Abbreviations

MPM	Meshfree Particle Method
MD	Molecular Dynamics
MC	Monte Carlo
DEM	Discrete Element Method
DPD	Dissipative Particle Method

SPH	Smooth Particle Hydrodynamics
MSM	Mass Spring Model
LSM	Lattice Spring Model
CGMD	Coarse Grained Molecular Dynamics
DMP	Discrete Multi-Physics
FSI	Fluid Structure Interaction

CHAPTER 4: THREE DIMENSSIONAL MODELLING OF AORTIC VALVE TO ASSESS THE EFFECT OF CALCIFICATION

4.1 Abstract

This study proposes a 3D particle-based (discrete) multiphysics approach for modelling calcification in the aortic valve. Different stages of calcification (from mild to severe) were simulated, and their effects on the cardiac output were assessed. The cardiac flow rate decreases with the level of calcification. In particular, there is a critical level of calcification below which the flow rate decreases dramatically. Mechanical stress on the membrane is also calculated. The results show that, as calcification progresses, spots of high mechanical stress appear. Firstly, they concentrate in the regions connecting two leaflets; when severe calcification is reached, then they extend to the area at the basis of the valve.

4.2. Introduction

Aortic valve disease is the malfunction of the aortic valve due to heart malformation at birth (congenital) or developed during a lifetime related to injury, age, or calcification of the valve (Fioretta et al., 2018). Calcification, in particular, may result in calcific aortic valve disease (CAVD) caused by calcium deposits on the valve leaflets, which mainly affects the elderly population with an incidence rate of 2 –7% in the population above 65 years of age (Amindari et al., 2017). Over time, calcium build-up makes the aortic valve stiffer, preventing full opening (stenosis) and hindering the blood flow from the left ventricle to the aorta. It may also prevent the valve from closing properly (regurgitation), resulting in blood leakages back to the ventricle.

Stenosis starts with the risk of leaflet deformation and progresses from early lesions to valve obstruction, which is initially mild to moderate but eventually becomes severe, with or without clinical symptoms (Otto and Prendergast, 2014) and the patient has high risk of cardiac failure.

In the literature, several studies focus on the dynamics of blood flow and the deformation of the calcified aortic valve leaflets to better understand and assess the severity of calcification. Computational fluid dynamics (CFD) was used to generate patient-specific aortic valve models from patients' medical images in (Fedele et al., 2017; Youssefi et al., 2017). Other studies (Bluestein and Einav, 1995; Hamid et al., 1985; Arjunon et al., 2013; Morganti et al., 2014; Lazaros et al., 2018) focus on investigating the stresses on the valve leaflets, excluding the fluid flow behaviour in the model. Since the behaviour of the aortic valve depends on both the fluid and the leaflets, a fluid–structure interaction (FSI) approach is recommended to model the complex dynamic of this problem (Ghasemi Bahraseman et al., 2016; Amindari et al., 2017).

In this paper, we aim to use discrete multiphysics (DMP) (Alexiadis, 2015b, 2014, 2015a), which enables the fluid–solid interaction, to develop a 3D model representing various stages of calcification of the aortic valve. DMP has been extensively used in in silico medicine for modelling a variety of human systems including the aortic valve (Ariane et al., 2017a), the intestine (Alexiadis et al., 2017), deep venous valves (Ariane et al., 2018b, 2017b), the lungs (Ariane et al., 2018a), and, in conjunction with machine learning, peristalsis in the oesophagus (Alexiadis, 2019). Sections 2 and 3 give an overview of the method and model used, respectively.

4.2 Modelling Concept

Particle-based modelling approach was used to study the effect of AVC on the blood transport through the heart and how the disorder progresses. SPH and LSM are the two particle methods used which they are coupled together to form the hybrid DMP framework.

4.3.1. Smooth Particle Hydrodynamics

The evolution of Smoothed particle hydrodynamics (SPH) has already been discussed in the previous chapters (Chapter 2 and 3). Therefore, it is not news that the SPH method is gaining popularity, recently, in a variety of fields and has a wide range of applications such as multiphase flow (Hopp-Hirschler et al., 2018; Rahmat and Yildiz, 2018), biomedicals (Ariane et al., 2017a, 2018b, 2018a; Schütt et al., 2020), fluid–solid interaction (Alexiadis, 2015b; Schütt et al., 2020; Ji et al., 2019; Li et al., 2019; Rahmat et al., 2019; Tran-Duc et al., 2017), and hydrodynamic instability (Rahmat et al., 2014; Shadloo and Yildiz, 2011).

Fundamental equations of SPH and the SPH formulation were in the literature and the methodology chapters respectively. However, note should be taken we adapt all the equation from the initial identity (equation 2.5) to the final Tait's equation of state (equation 2.10)

$$f(r) = \iiint f(r')\delta(r - r')dr' \tag{2.5}$$

$$P(\rho) = \frac{c_0\rho_0}{7}\left[\left(\frac{\rho}{\rho_0}\right)^7 - 1\right], \tag{2.10}$$

4.3.2. Lattice Spring Model (LSM)

As earlier discussed (in chapter 2 and 3), the LSM follows the idea that any material point of the body can be referred to by its position vector *r = (x,y,z)* (Pazdniakou and Adler, 2012). When that body undergoes deformation due to an applied force *F*, the displacement is proportional to the force applied.

$$F = k(r - r_0) \tag{2.11}$$

where r_0 is the initial distance between the two particles, r is the distance at time t, and k is a Hookean constant, and the spring constant is then related to the young modulus of the material by equation (2.14).

$$k = \frac{Er_0}{2.5}. \tag{2.14}$$

4.3. Discrete Multiphysics

Multiphysics simulation allows for tackling problems that involve multiple physical models or simultaneous physical phenomena, and that gives it widespread application in both industry and academia (Alexiadis, 2019). Discrete multiphysics, therefore, is a method based on particles and that combines various particle methods such as smoothed particle hydrodynamics (SPH), lattice spring model (LSM), and discrete element method (Ariane et al., 2017a). The current model only accounts for SPH and LSM. Both modelling techniques are briefly discussed below. The reader can refer to (Liu and Liu, 2003) for a more extensive introduction to SPH, and to (Kot et al., 2015) for the LSM. For details on how the two models are linked together in DMP refer to chapter 3. However, this can also be found in Alexiadis, 2015b, 2014.

4.4. The Model

As mentioned, the multiphysics model used in this study is based on DMP, a computational method that combines various particle methods. In the case under investigation, the computational domain is divided into two parts: (i) a liquid part (blood) where smooth particle hydrodynamics (SPH) is used, and (ii) the solid structure part (valve) where the stress deformation equation is solved using the lattice spring model (LSM). The two parts are

coupled together to represent an FSI model that simulates the valve deformation and blood flow dynamics within the valve.

In Figure 1a, the valve's leaflets (tricuspid) are shown; Figure 1b shows the overall geometry. The geometry was firstly designed as a CAD model (nodes and elements) and then transformed to a particle model as explained in the Appendix A. Simulations were run with the open-source software LAMMPS (Plimpton, 1995).

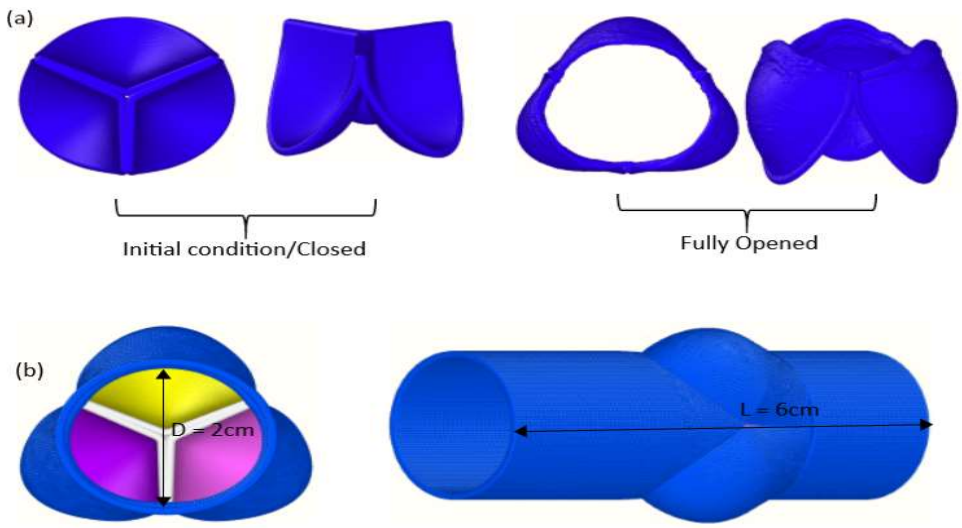

Figure 4.1: Valve leaflets (a) and complete geometry (b)

The system is three-dimensional and consists of 418,743 particles: 342,358 particles for the fluid, 19,725 particles for the leaflets, and 56,660 particles for the rigid pipe. The distance between particles (particle spacing) and the number of particles were chosen from the previous work done where DMP was used to model similar FSI problems (Schütt et al., 2020; Rahmat et al., 2019). In this study, the aortic valve geometry of (Bavo et al., 2016) was adopted. The leaflets tissue was modelled as linear and elastic, whereas the elasticity of the aorta (rigid pipe) was neglected, and the arterial wall was assumed to be rigid (Bavo et al., 2016).

In the simulation, the flow is driven by a periodic acceleration (Figure 4.2) given by

$$G = G_0 \sin^n(\omega t) cos(\omega t - \phi) \tag{4.5}$$

where $G_0 = 400$ m s^{-2}, $\omega = 2\pi f$ is the angular frequency, $n = 13$, and $\phi = \pi/10$ as discussed in (Stevens et al., 2003). The value of G_0 is determined to achieve full opening of the valve that gives an average flow rate around 600 mL s^{-1} for valves at normal condition, which is consistent with the literature, e.g., (Stevens et al., 2003; Murgo et al., 1980; Blais et al., 2006).

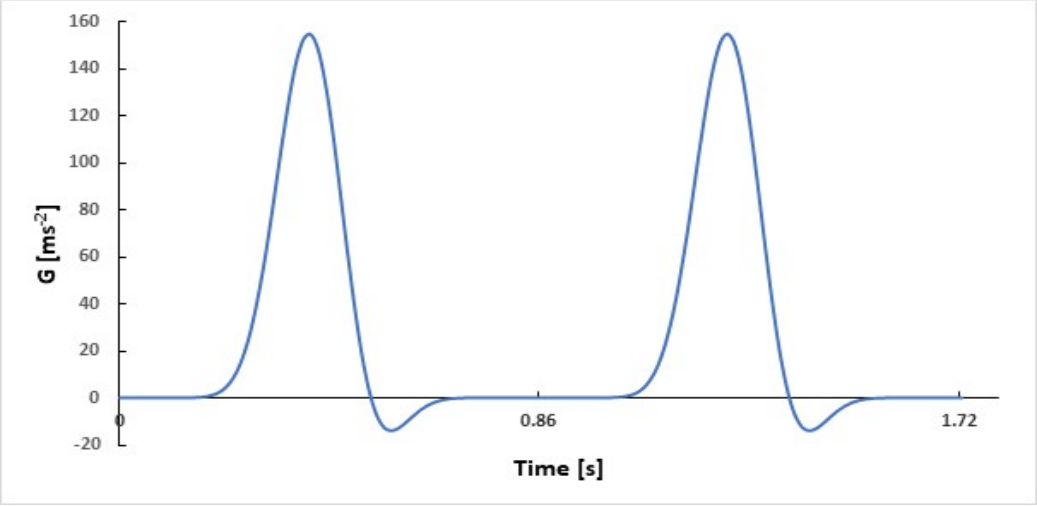

Figure 4.2: Pulsatile flow function

As mentioned, the flexible valve is modelled with LSM, which is a common approach for cardiovascular valves (Hammer et al., 2011). This implies that each computational particle is linked with its neighbour particles by means of a force in Equation (3.18).

In LSM, the value of k is linked to the Young modulus E of the material (Pazdniakou and Adler, 2012). In practice, however, it is not always straightforward to calculate k from E in the case of complex geometries, in particular, with irregular particles distribution (Lloyd et al., 2007). For this reason, we use a more practical approach: k is determined, together with G_0, in

such a way that the valve opens fully and the flow rate for a healthy and non-calcified valve is 600 mL s^{-1} as discussed above.

The numerical model used in this paper has extensively been tested and validated for a variety of similar fluid flow problems (Ariane et al., 2017a; Alexiadis et al., 2017; Ariane et al., 2018b, 2017b; Rahmat et al., 2019). In this paper, the value of k in the lattice model, as mentioned earlier, and G_0 in Equation (4.5) were chosen in such a way to make sure the flow in the valve and its opening are consistent with available observations (e.g., (Stevens et al., 2003; Murgo et al., 1980; Blais et al., 2006; Jermihov et al., 2011; Auricchio et al., 2014)). Convergence of the results on the number of particles used to discretise the system was carried out and the numbers reported in Table 4.1 represent the best compromise between accuracy and computational times. Since we refer to the human body, the available observations of real valves show very scattered results because of individual variability. Therefore, we cannot provide a systematic validation like in the case of experiments carried out in a laboratory under controlled conditions. This is even more true for calcified valves, where, on top of physiological variations, we have additional variations due to the severity and the course of the disease. Given all of the above, the best we can do is to make sure that the results are consistent with real data. In our study, we achieved this by making sure that the flow in the valve and the opening of the leaflets are both within the range of real observations.

Table 4.0.1: Model parameters used in the simulation; for the meaning of SPH parameters such as α or h, refer to (Liu et al., 2003).

Parameters	**Values**
Number of SPH wall particle	56,660
Number of SPH fluid particle	342,358
Number of SPH leaflets	19,725
Mass of each particle (fluid)	6.7×10^{-8} kg
Mass of each particle (Solid)	14×10^{-8} kg
Smoothing length h	1.0×10^{-3} m
Length L	6×10^{-2} m
Diameter D	2×10^{-2} m
Particle spacing l	0.4×10^{-3} m
Fluid Density ρ	1060 kg m^{-3}
Frequency f	1.167 s^{-1} (70 beats min^{-1})
Pseudo-gravity G_0	400 m s^{-2}
Viscosity μ	0.003 Pa·s
Elastic constant k	10−14,500 N m^{-1}
Sound speed c_0	16 m s^{-1}
Time step Δt	1×10^{-6} s

4.5. Results and Discussion

4.5.1. Stages of Calcification

In our model, the value of k was chosen to control the stiffness of the valve and model calcification. The higher the value of k, the stiffer the valve. In our model, higher values of k are used to model a higher degree of calcification. We define the degree of calcification γ as

$$\gamma = \log\left(\frac{k}{k_H}\right) \tag{4.6}$$

where k is the spring constant used to simulate the calcified valve and k_H is the stiffness of the healthy valve. Figure 4.3 shows the valve during maximal opening for four different degrees of calcification.

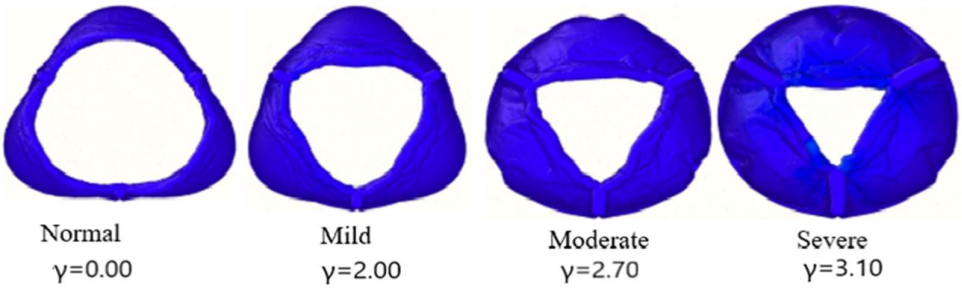

Figure 4.3: Severity of aortic valve stenosis in terms of orifice opening (stenosis)

Some important parameters like flow velocity, volume flow rate, and stress can be used to ascertain the level of calcification of the valves. Figure 4.4 shows how the flow velocity in the valve is affected by calcification.

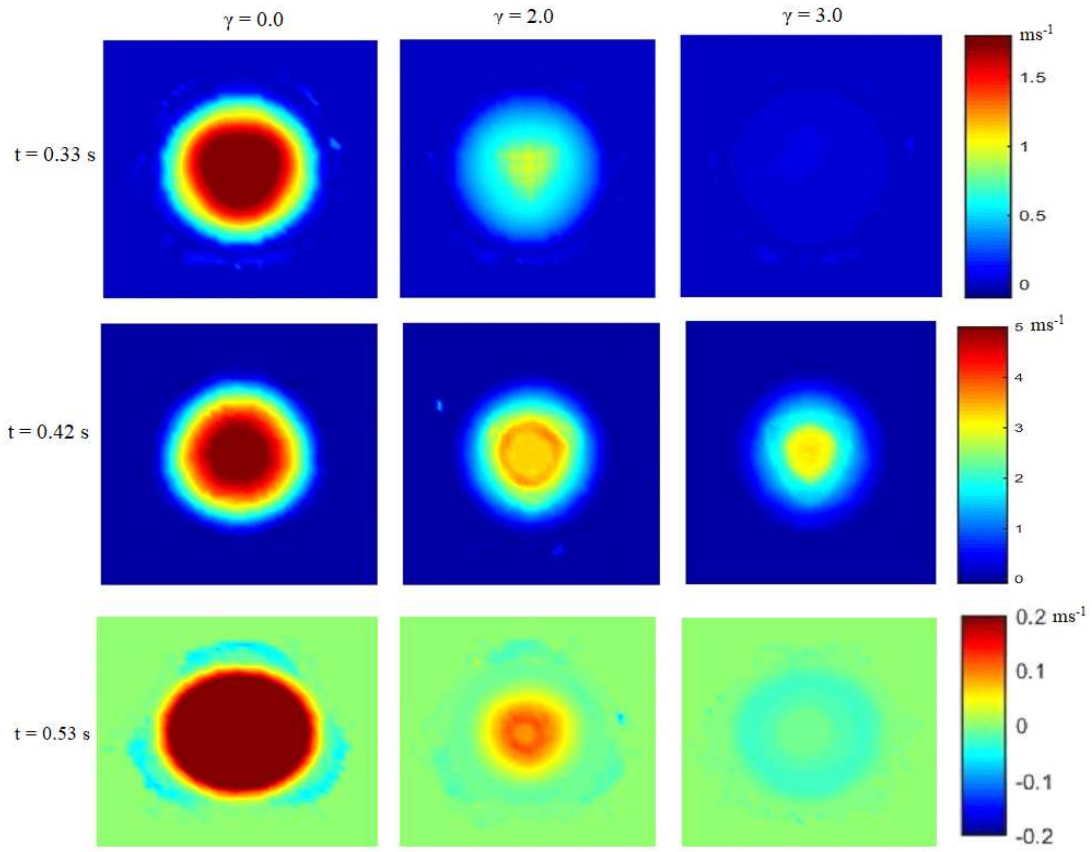

Figure 4.4: Velocity profile at different time steps

The flow velocity was measured on a section just above the valve for three different degrees of calcification and three different times. According to the level of calcification, the valve opens and closes at different times. The healthy valve ($\gamma = 0$) starts opening at $t = 0.29$ s, reaches maximal opening (peak systole) at $t = 0.41$ s, and closes again at $t = 0.56$ s. The valve with $\gamma = 2.0$ starts opening at $t = 0.32$ s, reaches maximal opening at $t = 0.43$ s, and closes again at $t = 0.54$ s. The valve with $\gamma = 3.0$ starts opening at $t = 0.37$ s, reaches maximal opening at $t = 0.43$ s, and closes again at $t = 0.53$ s. Figure 4.4 also relates with Figure 4.3 in showing how the valve opening is reduced (stenosis) in case of calcification. The time to attain peak velocity varies with the severity of the valve's stenosis, which signifies high mortality risk and the need for a valve replacement (Kamimura et al., 2016). The time at which the valve closes

also varies with the severity of calcification; at $\gamma = 3.0$, there is also evidence of regurgitation (back flow), a characteristic of a stenotic aortic valve (Fioretta et al., 2018; Otto and Prendergast, 2014; Morganti et al., 2014). Figure 4.4 also shows that, as expected, the blood flow in the healthy valve ($\gamma = 0.0$) is higher than in the calcified valves ($\gamma = 2.0$ and $\gamma = 3$).

Transvalvular flow is another important parameter for measuring aortic valve functionality. The flow reduces as γ increases (Figure 4.5); it decreases almost linearly up to a critical value $\gamma_{CR} = 3$, after which it decreases sharply. In Figure 4.5, γ_{CR} corresponds to a flow rate of 200 mL s^{-1}. Our calculations are consistent with the medical literature where a flow rate ≥250 mL s^{-1} is considered acceptable, whereas <200 mL s^{-1} is associated with an increase of mortality rate in cases of patients with aortic stenosis (Blais et al., 2006; Saeed et al., 2017). The maximum orifice diameter and the average stress on the valve (see next section) can also be used to monitor the progression of the valve stenosis. Table 4.2 summarizes the parameters as the condition worsens from normal to severe.

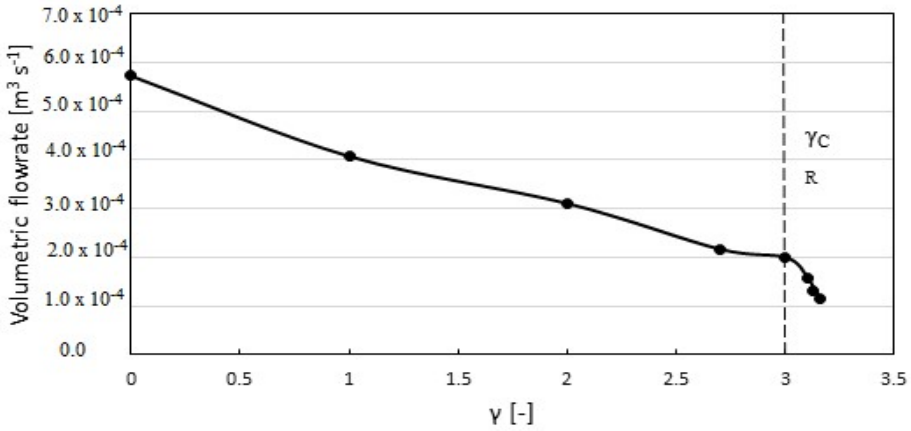

Figure 4.5: Volumetric blood flow with respect to γ

Table 4.0.2: Parameters for determining severity of calcification

Calcification	**Maximum Orifice Diameter [cm]**	**Mean Flow $\times 10^{-4}$ [$m^3 s^{-1}$]**	**Average Stress [kPa]**
Normal ($\gamma = 0.0$)	1.81	5.72	10.60
Mild ($\gamma = 2.0$)	1.41	3.21	91.68
Moderate ($\gamma = 2.7$)	1.29	2.17	181.61
Severe ($\gamma = 3.1$)	1.17	1.58	324.27

4.5.2. Stress Distribution on the Membrane

Calcification increases the stiffness of the valve, which results in higher stresses on the membrane. This is particularly important because mechanical stress plays a major role in the calcification of bioprostheses (Thubrikar et al., 1983). This, potentially, can create a vicious circle where calcification leads to higher mechanical stress, which, in turn, leads to further calcification. Figure 4.6 shows how the average stress increases with the degree of calcification. Since stenosis due to calcification can be related to congenital bicuspid valve disease or fused leaflets (Huntley et al., 2018), the numerical values of 0.28 to 0.35 MPa obtained for calcified valves are consistent with those reported by (Jermihov et al., 2011) for fused tri-leaflet valves. For stress distribution in a transcatheter aortic valve, the maximum value of 0.35 MPa is also consistent with the report of Auricchio et al. (2014).

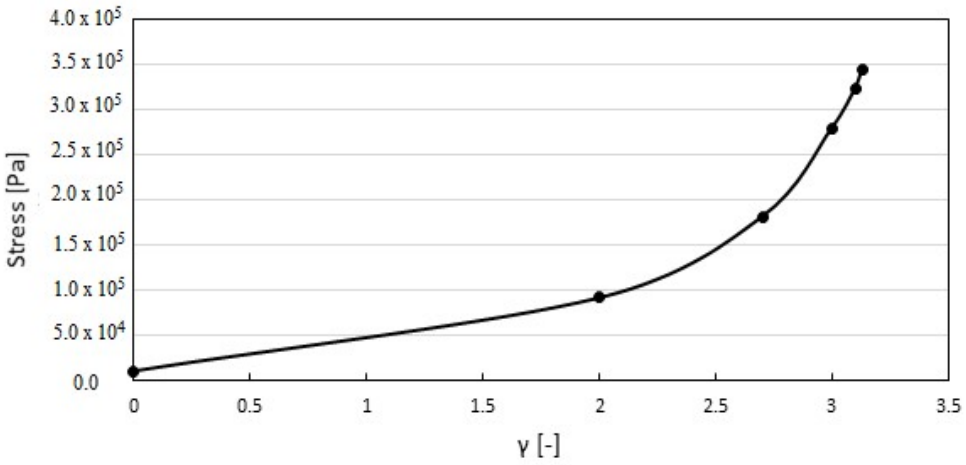

Figure 4.6: Stress at different degrees of calcification

The local stress distribution (i.e., the Frobenius norm of the stress tensor) on the leaflets is shown in Figure 4.7, considering a membrane thickness of 0.6 mm (Hamid et al., 1985). In this work, calcification is modelled by uniformly increasing the Young modulus of the membrane; Figure 4.7 suggests that calcification does not progress uniformly.

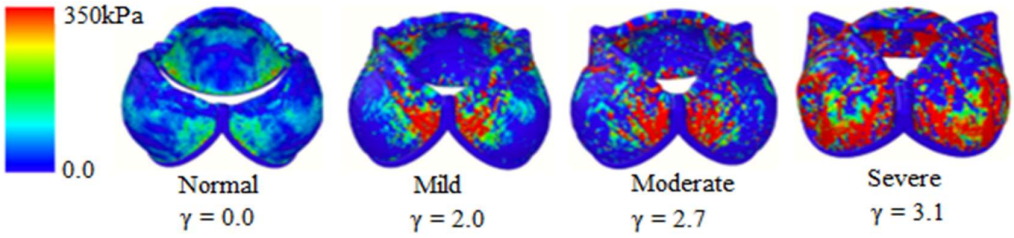

Figure 4.7: Mechanical stress on the valve leaflets at maximal opening

In fact, as calcification progresses, spots of high mechanical stress appear. Firstly, they concentrate in the regions connecting two leaflets; when severe calcification is reached, they extend to the area at the basis of the valve.

4.6. Conclusions

In this study, the effect of calcification in a 3D aortic valve is simulated with discrete multiphysics. The model accounts for both hemodynamics and leaflet deformation, and it can be considered an improvement over a previous 2D model (Ariane et al., 2017a). The results show that the mean transvalvular flow could be used to assess valve calcification, and severe calcification occurs when the flow rate is lower than 200 mL s^{-1}.

The model can also assess the local stress on the membrane. Calcification increases mechanical stress, which, in turn, promotes further calcification. In this work, calcification is modelled by uniformly increasing the young modulus of the membrane. The results show that, as calcification progresses, spots of high mechanical stress appear. Firstly, they concentrate in the regions connecting two leaflets; when severe calcification is reached, they extend to the area at the basis of the valve. This suggests that the model could be improved by accounting for local changes in stiffness, which depends on the local stress distribution.

Methodologically, this work can also benefit researchers interested in particle methods, but not necessarily to cardiovascular applications. In fact, the Appendix A explains how geometries designed with CAD model can be transformed to particle models.

4.7 Notations and abbreviations

Notations

m	mass [Kg]
ρ	Density [Kg m^{-3}]
c_0	Sound speed [m s^{-1}]
P	Pressure [N m^{-2}]
u	Fluid velocity [m s^{-1}]
v	Kinematic viscosity [P.sa]
g	Gravity [m s^{-2}]
W	Kernel function [m]
h	Smoothing length [m]
r	Distance [m]
V	Volume [m^3]
Δt	Time steps [s]
γ	Degree of calcification [-]
k	Spring constant [N m^{-1}]
k_H	Stiffness of the healthy valve [N m^{-1}]
F	Force [N]
f	Frequency [Hz]

ω	Angular frequency [Hz]
G	Periodic acceleration [m s^{-2}]
Φ	Angle [rad]
E	Young modulus [N m^{-2}]
t	Time [s]

Abbreviations

CFD	Computational Fluid Dynamics
FSI	Fluid Structure Interaction
DMP	Discrete Multi-Physics
SPH	Smooth Particle Hydrodynamics
LSM	Lattice Spring Model
MSM	Mass Spring Model
CAD	Computer Aided Design
LAMMPS	Large-scale Atomic/Molecular Massively Parallel Simulator
CGMD	Coarse Grained Molecular Dynamics

CHAPTER 5: FLUID-STRUCTURE INTERACTION IN CORONARY STENT: A DISCRETE MULTIPHYSICS APPROACH

5.1 Overview

Stenting is a common method for treating atherosclerosis. A metal or polymer stent is deployed to open the stenosed artery or vein. After the stent is deployed, the blood flow dynamics influence the mechanics by compressing and expanding the structure. If the stent does not respond properly to the resulting stress, vascular wall injury or re-stenosis can occur. In this work, a Discrete Multiphysics modelling approach is used to study the mechanical deformation of the coronary stent and its relationship with the blood flow dynamics. The major parameters responsible for deforming the stent are sorted in terms of dimensionless numbers and a relationship between the elastic forces in the stent and pressure forces in the fluid is established. The blood flow and the stiffness of the stent material contribute significantly to the stent deformation and affect its rate of deformation. The stress distribution in the stent is not uniform with the higher stresses occurring at the nodes of the structure. From the relationship (correlation) between the elastic force and the pressure force, depending on the type of material used for the stent, the model can be used to predict whether the stent is at risk of fracture or not after deployment.

5.2 Introduction

Atherosclerosis is a condition where arteries become clogged with fatty substances called plaque. The plaque is deposited on the arterial wall, and this leads to the narrowing of the artery and subsequently obstruction of the blood flow known as stenosis. This obstruction hinders the smooth transportation of blood through these arteries and consequently poses a serious health problem. When atherosclerosis affects an artery that transports oxygenated blood to the heart, it is called coronary artery disease. Coronary artery disease is the most common heart disease that becomes the leading cause of death globally. Worldwide, it is

associated with 17.8 million deaths annually (B rown et al., 2021). The healthcare service for coronary artery disease poses a serious economic burden even on the developed countries, costing about 200 billion dollars annually in the United States.

The obstruction of the flow line (stenosis) also alters the blood flow regime and causes a deviation from laminar to turbulence, or even transitional flow (Kolodgie et al., 2007; Evju and Mardal, 2015), a situation that signifies severely disturbed flow. Studies were carried out on the types of plaque and its morphologies as well as the flow type and its consequence (Otsuka et al., 2016; Griffith et al., 2013; Jain, 2020; Ahmed and Giddens, 1984) that occurred in human arteries. Although the disease is deadly, it is preventable. Therefore, it is paramount to manage or prevent it in order to restore normal blood flow in the affected artery.

One of the ways of managing coronary artery disease is restoring normal blood flow or revascularization in a patient with a severe condition using the percutaneous coronary intervention (with stent) (Di Venuta et al., 2017). Coronary stents are tubular scaffolds that are deployed to recover the shrinking size of a diseased (narrowed) arterial segment (Pant et al., 2012) and stenting is a primary treatment of a stenosed artery that hinders smooth blood flow (Hsiao et al., 2012).

The stents used in clinical practice come in differential geometry and design which implies varying stress distribution within the local hemodynamic environment as well as on the plaque and artery (Wei et al., 2019a; Colombo et al., 2002). The stent structure also induces different levels of Wall Shear Stress (WSS) on the wall of the artery (Balossino et al., 2008; Pant et al., 2012). Many cases of stent failure due to unbearable stress were reported and therefore, a careful study on how these stresses are distributed is needed. In fact, stent fracture or failure often occurs after stent implantation, and it can be avoidable if the mechanical property and

the performance of the material are predicted. An ideal stent should provide good arterial support after expansion by having high radial strength. It should also cause minimal injury to the artery when expanded and should have high flexibility for easy manoeuvring during insertion (Duraiswamy et al., 2005; Pant et al., 2010).

Studies on the different stent designs and how they affect their mechanical performance were reported (Balossino et al., 2008; Colombo et al., 2002). Stent deformation and fracture after implantation were also investigated (Finet and Rioufol, 2012; Choudhury et al., 2017; Ding et al., 2019; Chinikar and Sadeghipour, 2014; Alqahtani et al., 2013). Moreover, numerical modelling and simulations were also used in studying coronary stent and stent implantation. For instance, Di Venuta et al., 2017 carried out a numerical simulation on a failed coronary stent implant on the degree of residual stenosis and discovered that the wall shear stress increases monotonically, but not linearly with the degree of residual stenosis (Di Venuta et al., 2017). Simulation of hemodynamics in a stented coronary artery and for in-stent restenosis was performed by (Faik et al., 2007; Caiazzo et al., 2011).

With a few exceptions (Beier et al., 2016; Xu et al., 2016; Wei et al., 2019b), the mechanical properties of the stent and the blood fluid dynamics around the stent were studied separately. In this work, we propose a single Fluid-Structure Interaction (FSI) model that calculates the stress on the stent produced by the pulsatile flow around the stent; both the stent mechanics and the blood hydrodynamics are calculated at the same time. The model is based on the Discrete Multiphysics (DMP) framework (Alexiadis, 2014), which has been used in a variety of FSI problems in biological systems such as the intestine (Schütt et al., 2020), aortic valve (Ariane et al., 2018a; Mohammed et al., 2020), the lungs (Ariane et al., 2018a), deep venous valves (Ariane et al., 2017b, 2018b). In this study, therefore, we use the DMP framework to

develop an FSI 3D coronary stent model coupled with the blood hydrodynamics and analyse the mechanical deformations produced by the flow hydrodynamics.

5.3 Methodology

The methodology adopted is that of the previously used DMP. Recently, the Discrete Multiphysics framework combines together particle-based techniques such as Smooth Particle Hydrodynamics (SPH) (Albano and Alexiadis, 2020, 2021), Discrete Element Method (DEM) (Liu and Wu, 2020; Ng et al., 2020), Lattice Spring Model (LSM) (Sahputra et al., 2020; Ruiz-Riancho et al., 2021), PeriDynamics (PD) (Sanfilippo et al., 2021), and even Artificial Neural Networks (ANN) (Alexiadis, 2019a; Alexiadis et al., 2020). In this case, the model couples SPH and LSM. The computational domain is divided into the liquid domain and the solid domain. The liquid domain represents the blood, and it is modelled with SPH particles; the solid domain represents the stent and the arterial walls and it is modelled with LSM particles. Details on SPH theory can be found in (Liu and Liu, 2003), and of LSM in (Kot et al., 2015; Kot, 2021). Here a brief introduction of the equations used in SPH and LSM is provided.

For specifics and an accurate comprehension of the concept and methods, one might turn to the equations and formulation of SPH and LSM found in chapters 2 and 3.

5.4 Model and Geometry

A three-dimensional stent model including blood flow hydrodynamics and stent mechanics is developed. The model simulates the blood dynamics in a 3D channel similar to a coronary artery with a $1.5 \cdot 10^{-3}$ m internal radius, including a PS-shape stent of 4 struts in the *x*-direction and 4 struts in the *z*-direction (circumference). The stent has a thickness of 100 μm, and 7.5 mm length, the size that is within the range of the stent used in clinical practice (Wall

et al., 2018). We choose a PS-Shaped because it performs better compare to most commercially shaped stents as reported by (Wei et al., 2019b).

The geometry was created using CAD. From the geometry, we used MATLAB script to generate the coordinate of the computational particles as the points are created with MATLAB (details can be found in (Mohammed et al., 2020)). The script also generates a LAMMPS data file for the simulations and the simulations were run with LAMMPS, an open-source software (Plimpton, 1995). The three-dimensional model consists of 1,862,804 particles: 1,609,452 particles for the fluid, 46,336 particles for the stent and 207,016 particles for the arterial wall. The fluid has a density (ρ) of 1056 kg m^{-3} and viscosity (μ) 0.0035 Pa·s. Figure 5.1 shows the section geometry of the stent within and outside the arterial wall. Local acceleration term g_0 was included to force the fluid to flow at a particular velocity. The inclusion of the local velocity is due to the unsteady or pulsatile flow existing in the cardiovascular system (Ku, 1997). Womersley parameter α, which is the ratio of unsteady force to viscous force, was used in the model to induce the velocity profile of the flow. The particle spacing is $3.33 \cdot 10^{-5}$ m. The optimal spacing value is obtained after several simulations with different particle spacings to make sure the results are independent of the particle resolution. Stress and deformation and other postprocessing calculations were done with the visualization software OVITO (Stukowski, 2010). The arterial wall is assumed to be rigid with a no-slip condition (Wei et al., 2019b) whereas the stent is elastic. The no-slip and no penetration boundary condition is imposed at the interface of the solid-liquid interaction as discussed in our previous work (Alexiadis, 2015b). Figure 1a and 1b show a section of the solid geometry which includes the stent and the wall and the complete geometry of the stent respectively.

The flow is being driven by a sinusoidal (pulsatile) acceleration (G) of the flow in the axial direction to simulate a heartbeat of 60/min with a period (T) of 1 s; the same approach was used in a previous publication (Mohammed et al., 2020), where the reader can find more details.

Eighteen (18) sets of simulations were run with a combination of $v1 - v3$ and $k1 - k6$ (see Section 5.4 for reasons). The University of Birmingham Bluebear (super-computer) was used for the computation (simulation) where ninety (90) processors were assigned for 72 h to run each simulation. For each simulation, a dump file (result file) of 9–10 GB of memory is obtained.

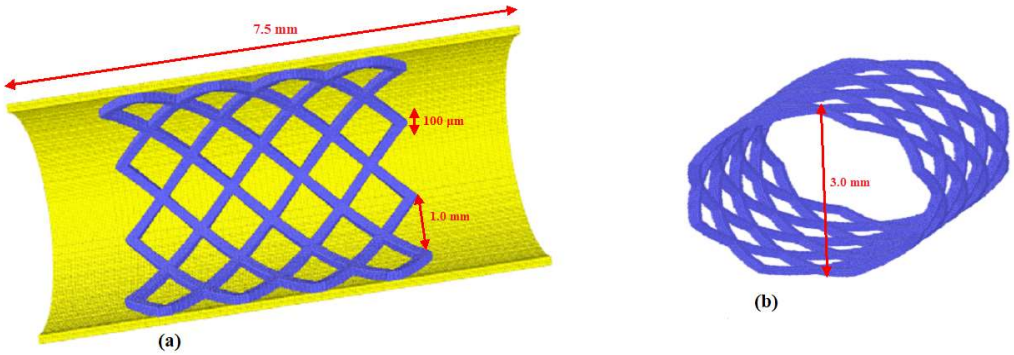

Figure 5.1: Illustration of the 3D stent geometry at (a) section view; and (b) front view showing complete stent

To better understand the hydrodynamics of the fluid and to be able to access the deformation of the stent, the discussion is carried out in terms of dimensionless numbers. According to the Buckingham π theorem, a physically meaningful equation involving n physical variables can be rewritten in terms of a set of $p = n - k$ dimensionless parameters $\Pi_1, \Pi_2, \ldots, \Pi_p$, where k is the number of physical dimensions involved. In this case, the physiochemical properties of blood are constant, and the geometry is fixed. Therefore, we want to express the resulting stress on the stent as a function f of the type

$$\sigma = f(P, d, E), \tag{5.10}$$

where s σ [kg m^{-1}s^{-2}] is the stress on the stent, P [kg m^{-1}s^{-2}] the dynamic pressure in the fluid (the force exerted by the fluid to the stent depends on P), d [m] a characteristic length of the stent (here, we use the thickness of the stent), and E [kg m^{-1}s^{-2}] the Young Modulus.

In this case, the dynamic pressure can be written in terms of fluid average velocity v and density r ρ,

$$P = \rho v^2, \tag{5.11}$$

Moreover, k [kg s^{-2}] and E are related in Equation (5.9). Therefore, assuming that the lattice spacing is fixed, we can replace Equation (7.10) with

$$\sigma = f(\rho, v, d, k), \tag{5.12}$$

Since we have 5 variables and 3 units, we can rewrite Equation (5.12) based on two dimensionless numbers

$$\Pi_2 = \varphi(\Pi_1). \tag{5.13}$$

The first dimensionless number can be defined as

$$\Pi_1 = \frac{k}{\rho v^2 d} \; \frac{\text{[elastic forces that contrast deformation (in the solid)]}}{\text{[pressure forces that tend to deform the stent (from the liquid)]}} \tag{5.14}$$

Knowing the typical ranges of E and d for the stent, and ρ and v for the blood, we can calculate the typical range of Π_1. The second parameter Π_2 can be defined as

$$\Pi_2 = \frac{\sigma\, d}{k}. \tag{5.15}$$

We can have different types of Π_2 according to the type of stress we use in Equation (5.15). The stress tensor has 6 independent components that can be composed in different ways to provide different types of information. One possibility is to use the Frobenius norm.

$$\sigma^F = \sqrt{\sigma_{xx}^2 + \sigma_{yy}^2 + \sigma_{zz}^2 + 2\sigma_{xy}^2 + 2\sigma_{xz}^2 + 2\sigma_{yz}^2} \tag{5.16}$$

In this case, we have a Π_2 based on the Frobenius norm

$$\Pi_2^F = \frac{\sigma^F d}{k}. \tag{5.17}$$

that expresses, in dimensionless form, the total stress in the stent. Another possibility is the von Mises stress

$$\sigma^V = \sqrt{\frac{1}{2}\left[\left(\sigma_{xx}-\sigma_{yy}\right)^2 + \left(\sigma_{yy}-\sigma_{zz}\right)^2 + (\sigma_{zz}-\sigma_{xx})^2\right] + 3\left(\sigma_{xy}^2 + \sigma_{yz}^2 + \sigma_{zx}^2\right)} \tag{5.18}$$

which provides another Π_2 number defined as

$$\Pi_2^V = \frac{\sigma^V d}{k}. \tag{5.19}$$

Physically, $\Pi^F{}_2$ and $\Pi^V{}_2$ are dimensionless stresses and can have both a local form $\Pi_2(x, y, z)$ (when we calculate them at each x, y, z position), and a global form $\langle\Pi_2\rangle$ (when we average them over the whole stent). Table 5.1 shows the parameters used in the simulation.

Table 5.1: Parameters used in the simulation of the coronary artery stent

SPH	
Number of SPH fluid particles	1,609,452
Mass of each particle (fluid)	3.41×10^{-12} kg
Length L	7.5×10^{-3} m
Diameter D	3.0×10^{-3} m
Particle spacing l	3.33×10^{-5} m
Smoothing length h	7.5×10^{-5} m
Local acceleration term g_0	0.47138–1.25 m s^{-2}

Fluid Density ρ	1056 kg m^{-3}
Viscosity μ	0.0035 Pa·s
Sound speed c_0	4 m s^{-1}
Alpha α	0.1–0.25 [-]
Time step Δt	1×10^{-7} s
LSM	
Number of SPH stent particles	46,336
Number of SPH wall particles	207,016
Mass of each particle of the stent (Solid)	3.41×10^{-12} kg
Mass of each particle of the wall (Solid)	6.0×10^{-12} kg
Stent thickness d	1.0×10^{-4} m
Elastic constant k	0.5−25 kg s^{-2}

5.5 Results and Discussion

Three flow velocities of $0.4\ \mathrm{ms}^{-1}$, $0.23\ \mathrm{ms}^{-1}$ and $0.16\ \mathrm{ms}^{-1}$ were chosen to represent the normal coronary artery and the baseline flow, respectively. The value of k was chosen from 0.5 to 5 to cover materials with the lowest to highest Young modulus. The blood flow velocity observed within the stent ranges from $0.23\ \mathrm{ms}^{-1}$ to $0.4\ \mathrm{ms}^{-1}$, whereas the minimum flow velocity which may occur due to stenosis is $0.16\ \mathrm{ms}^{-1}$ and taken to be the baseline (Vrints et

al., 1999). The velocity profile at different viewpoints is shown in Figure 5.2.

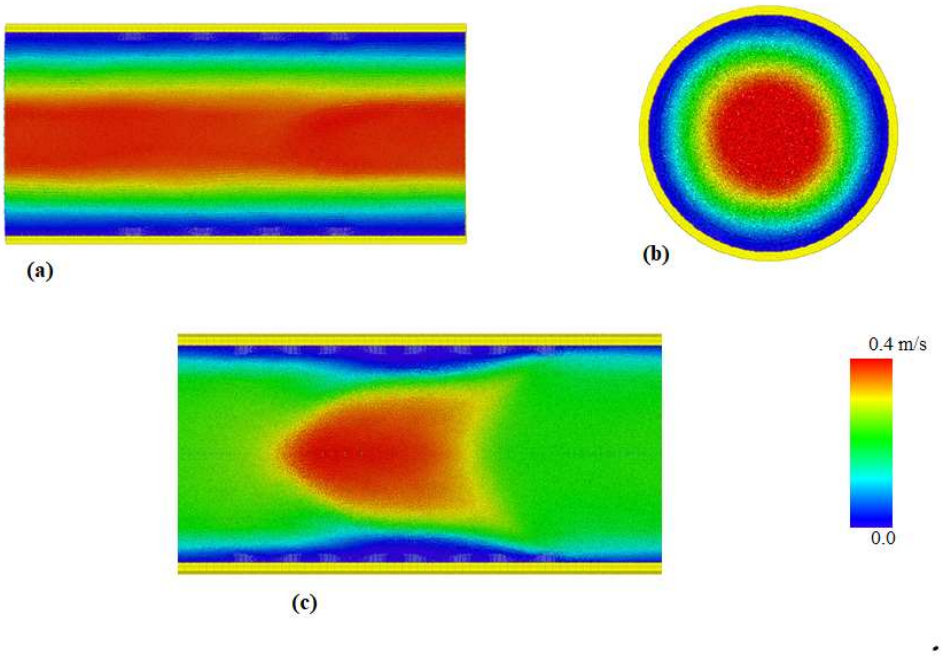

Figure 5.2: Velocity profile; (**a**) *x*-*y* view (steady state profile), (**b**) *y*-*z* view, and (**c**) parabolic profile at the beginning of the flow.

The dimensionless von Mises stress is shown in Figure 5.3 for two stents at different $\langle \Pi_1 \rangle$. Different values of $\langle \Pi_1 \rangle$ means different k and v. It is shown that the stress is more severe at the nodes (joints) with higher stress at higher $\langle \Pi_1 \rangle$ as clearly shown in Figure 5.3b. This may lead to potential stent failure (rapture) at the joins or size change of the stent resulting from compression or expansion. The expansion characteristics of a stent are the main causes of vascular wall injuries (Wiesent et al., 2019). Either of these conditions (failure or size change) will cause severe pain and damage to the patient and lead to restenosis and or stent redeployment.

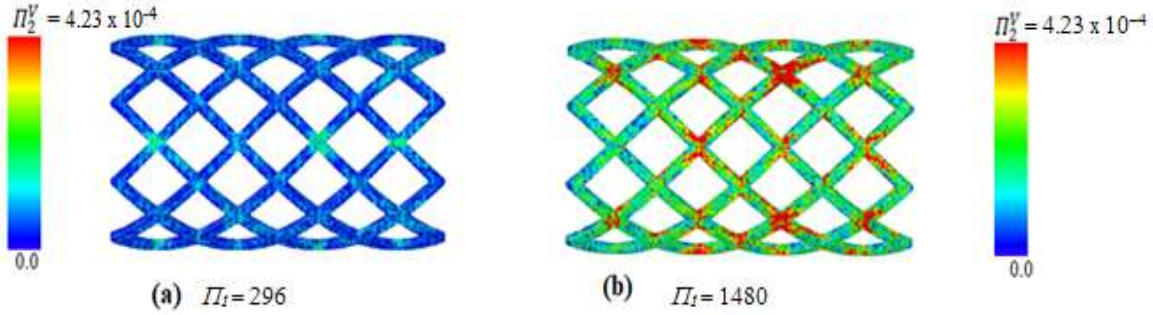

Figure 5.3: Local Π^V_2 at (a) $P_1 = 296$, and (b) $P_1 = 1480$

The result is first presented in Figure 5.4 and shows how the stress varies with k and v. This is then sorted in dimensionless form and presented in Figures 5.5 and 5.6, which shows the average stress $<\Pi^F_2>$, and $<\Pi^V_2>$ versus $<\Pi_1>$ in dimensionless form. If we use dimensionless numbers, the three curves of Figure 5.4 collapse in only one curve (Figures 5.5 and 5.6).

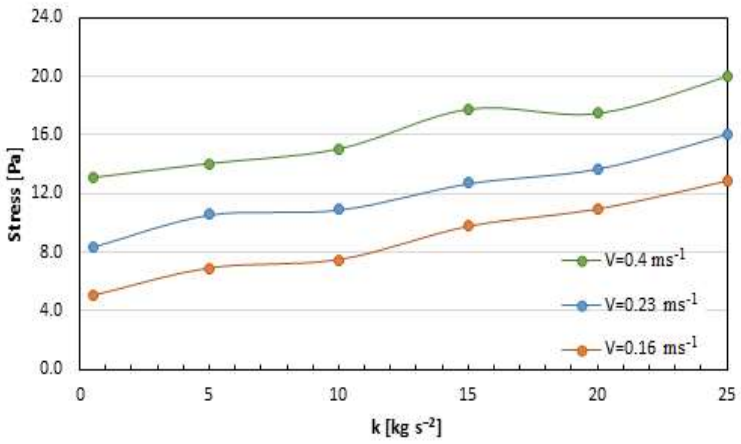

Figure 5.4: Stress (Frobenius norm of the stress tensor) with respect to k and v.

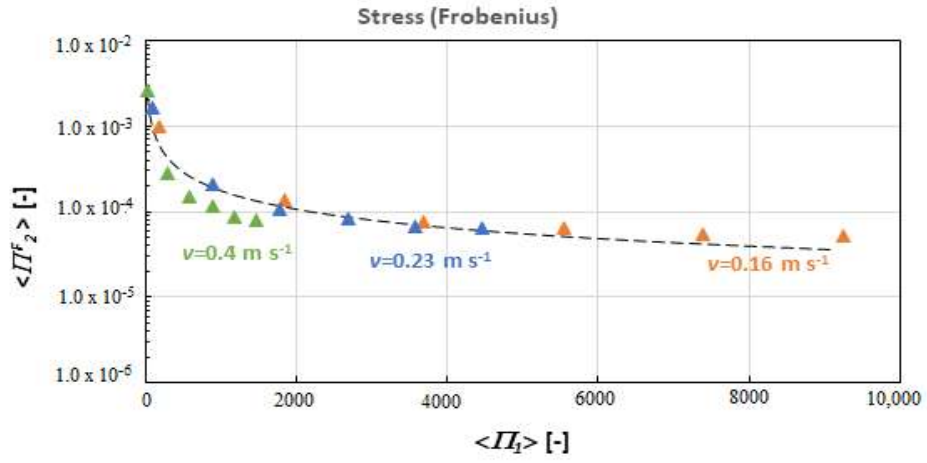

Figure 5.5**:** Relationship between average stress $<\Pi^F_2>$ and $<\Pi_1>$.

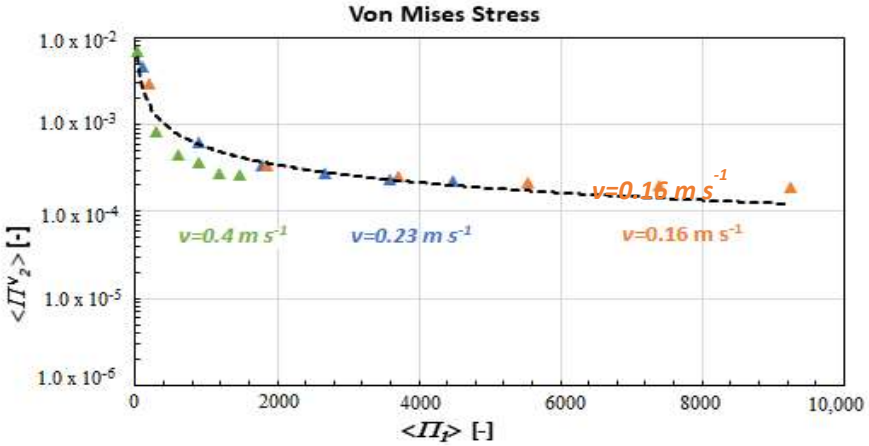

Figure 5.6**:** Relationship between average stress $<\Pi^V_2>$ and $<\Pi_1>$.

The plot confirms that the stress can be effectively sorted out with two dimensionless numbers based on the Buckingham π theorem. The three curves of Figure 5.4 can be fit by the same function as indicated in Equation (5.13). This function can be approximated by the following correlation (dotted line in)

$$< \Pi_2^F >= 0.026\langle \Pi_1 \rangle^{-0.723} \quad . \tag{5.20}$$

The same approach can be used for the von Mises stress which also has a correlation

$$< \Pi_2^V >= 0.058\langle \Pi_1 \rangle^{-0.6737}. \quad (5.21)$$

Numerically, we identified that the dimensionless numbers computed can be used as the fundamental group of the system in which the stress can be express in terms of Π_1 and Π_2.

Due to the pulsatile flow, the stent contracts and expands during the simulation. This causes the diameter of the stent to change with the flow. Figure 5.7 shows that the percentage change in the stent's diameter is fluctuating. This is because the arterial blood flow, which contributed to the stent deformation, is pulsatile in nature (Huo and Kassab, 2006; Cheung, 2010), therefore, it is expected to have a nonlinear change in the diameter. Note that the deformation is not only a function of the pressure forces from the liquid (blood) but also the elastic forces from the solid (stent). For that reason, several oscillation modes occur at the same time and the diameter change is not a simple repetition of the pulsatile flow.

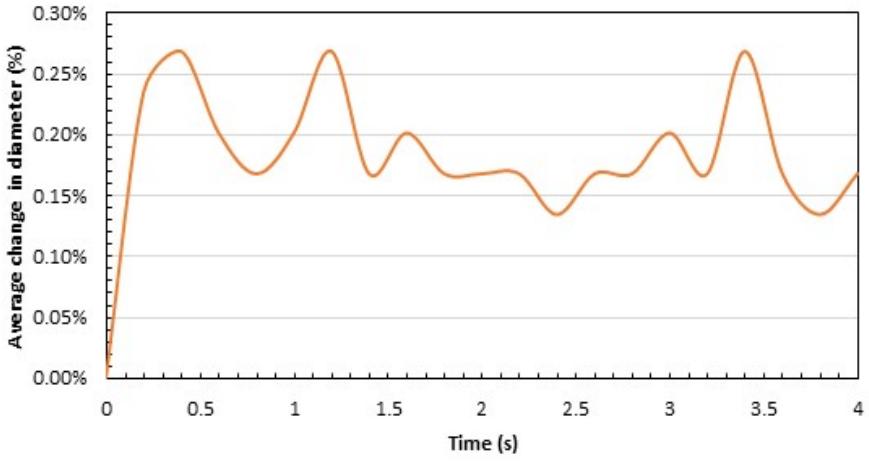

Figure 5.7: Average diameter change with time.

Another likely incidence of vascular wall injury associated with stent expansion which can be quantified using the model is the so-called dogboning (*DB*) effect/ratio. This phenomenon

occurs when the stent expands at the ends, resulting in increased stress and injuries at the arterial wall (Wiesent et al., 2019). This occurs when the diameter expands at both ends of the stent and contracts at the centre. The dogboning ratio is defined as,

$$DB = \frac{D_{max,end} - D_{min,central}}{D_{max,end}} x100\% \quad (2.1)$$

where $D_{max,end}$ is the maximum stent diameter at the end (distal and proximal), and $D_{min,central}$ is the minimum stent diameter at the centre. Our model is capable of analysing the dogboning ratio which could be used to assess and reduce the potential risk of vascular wall injury, and therefore, in this study, *DB* was calculated to be 4.4%. This is value is less than the 6.3% reported by (Wei et al., 2019b) for PS-shaped stent. This variation may be as a result of using different methodology from that of Wei et al. and may also indicate greater computational accuracy because the performance of a stent is improved when its *DB* value is lower.

5.6 Conclusions

In this paper, a Discrete Multiphysics model is used to simulate a coronary stent accounting for both its hemodynamics and mechanical stress. The model is three-dimensional and includes both the fluid (blood) and the solid structures (arterial wall and stent) and it is used to study the link between the flow dynamics and the mechanical deformation of the stent. The mechanical stress is computed using dimensionless numbers and a relationship between elastic forces and pressure forces was established. The results show that the blood flow contributes significantly to the stent deformation and the stiffness of the stent material affected the rate of

deformation. Nonuniform stress distributions are observed. In particular, high stresses are observed at the nodes of the stent.

Given a specific Π_1 and from the corresponding Π_2^V, the maximum stress can be obtained. However, a fracture is not directly accounted for. This will depend on the pressure (stress) and type of material used for the stent as reported in the literature. Different materials have different yield stress (above which the stent fracture occurs). Our model can be used for all types of material by comparing the maximal stress in the structure against the material yield stress. Using the correlation in Equation (5.21), maximum Π_2^V can be found when a specific stent material's property (Young modulus) is known. That means, from the value of Π_1, we will be able to predict the Von Mises stress from Π_2^V (which can be compared against the yield stress) as well as the flow velocity. For clinical purposes, one just needs to know the material and the blood flow velocity in the diseased artery to be able to predict whether the stent is at risk of fracture or not. Therefore, the model can be used to predict the deformation of the stent once in place and the conditions that can potentially cause its failure.

5.7 Notations and abbreviations

Notations

m	mass [Kg]
ρ	Density [Kg m^{-3}]
c_0	Sound speed [m s^{-1}]
P	Pressure [N m^{-2}]
v	Fluid velocity [m s^{-1}]
g	Gravity [m s^{-2}]
W	Kernel function [m]
h	Smoothing length [m]
r	Distance [m]
Δt	Time steps [s]
l_0	Initial distance between particles [m]
k	Spring constant [N m^{-1}]
F/f	Force [N]
E	Young modulus [N m^{-2}]
K	Bulk modulus [N m^{-2}]
μ	fluid viscosity [P.sa]
σ	Stress [N m^{-2}]

Abbreviations

DMP	Discrete Multi-Physics
WSS	Wall Shear Stress
FSI	Fluid Structure Interaction
SPH	Smooth Particle Hydrodynamics
LSM	Lattice Spring Model
DEM	Discrete Element Method
PD	PeriDynamics
ANN	Artificial Neural Networks
CAD	Computer Aided Design
LAMMPS	Large-scale Atomic/Molecular Massively Parallel Simulator

CHAPTER 6: CONCLUSIONS AND RECOMMENDATIONS

6.0 General Conclusion

In this work, a Discrete Multiphysics (DMP) framework, which is a Lagrangian mesh-free technique, was used to simulate a multi-physical problem that involves a cardiovascular flow. In this approach two particle methods, Smooth Particle Hydrodynamics (SPH) and Lattice Spring Model (LSM) were combined to form the hybrid DMP framework where the fluid is modelled by the SPH particles, and the solids by the LSM.

This modelling approach was successfully used in practise to a range of vascular flow challenges, demonstrating the DMP technique's potential for research on sensitive human organs and tissues. In this instance, the method was used to evaluate the mechanical characteristics of the aortic valve leaflets in relation to their level of calcification where several stages of calcification were simulated and the effect of calcification on the leaflets and the blood flow dynamic analysed. With the same technique (DMP), the interaction between fluid (blood) and a metal intra-stent in a coronary artery was simulated and a relationship between the blood flow dynamic and the mechanical deformation of the stent was established.

Therefore, it is convenient to conclude that the study's objectives were achieved and that the findings have practical significance and can be apply as follows:

i. For clinical diagnosis of a calcified aortic valve patient, our findings can be used as a guide in predicting the severity of the condition. The degree of calcification is defined by a parameter γ which is related to the blood flowrate as well as the valve's orifice diameter. In this work, therefore, a critical value of γ was found above which the condition is said to be severe.

ii. The relationship between the stiffness of the leaflet tissue and the force placed on the valve has been researched and established. The parameter that tells the extent of the

blood flow stagnation due to calcification was found. These can be used to gauge the degree of calcification and level stenosis in the aortic valve by monitoring γ and the flow velocity.

iii. Equally with DMP approach, a correlation in form dimensionless number was established between a coronary stent material and the blood flow dynamics. This correlation can be used for clinical purposes to predict whether the stent (specific) is at risk of fracture once the flow velocity in the diseased artery is known. Therefore, the model developed in this research can be used in predicting the deformation of the stent material and the conditions that can potentially cause its failure.

Finally, this work demonstrated that mathematical models are robust, and that the DMP framework is proven to be an approach to modelling that can be used to a wide range of applications with relative ease. In particular, the DMP framework shows its potential especially when modelling biological structures.

Beside the significance of the work, as highlighted, and its contribution to knowledge, this research has equally met my personal goal. It gives me the ability to develop my skill in mathematical modelling and computer simulation using both mesh and particle-method approaches. When I began my PhD, my goal was to gain expertise in mathematical modelling and computer simulations. Most of the research carried out in engineering faculties in my country (Nigeria) is applied: focused on taking the necessary steps to resolve specific practical problems. My personal ambition was to go beyond this aspect and become experienced in designing the theoretical tools that other researchers can then use to solve practical problems. These skills, as I mentioned above, are rare in my country and have long remained the purview of Universities and Research centres in Europe and North America. I hope to pioneer an

intensified interest in this area in the university and research environment in Nigeria and beyond.

6.2 Limitations

This work is limited to using computer simulations only and no laboratory experiment is carried out. Therefore, the limitation of this thesis remains the lack of comparison with an experimental data, however, it was compared with and existing literatures on aortic valve calcification and coronary stents. It was also noticed that the computational time in DMP is higher compared with the standard mesh-based method and often requires high performance computers. This may be due to the individual particle's properties calculation during the simulation and is a constrain to using personal computers to run the simulation.

6.2 Further work

In addition to replication, the DMP framework should be used to model a stent with a design (from same material) to see if the design has significant effect on the mechanical property of the stent, especially the yield stress. Also, the aortic valve and the stages of calcification modelled in this work should be tested experimentally to ensure the workability of the model.

Generally, despite publishing some of the results in this work, there is need for replication of this research. This is because replication is important in sciences as it test the credibility of original studies and separate the true outcomes from those that are unreliable. As Ioannidis, (2005) would say, "published research findings are sometimes refuted by subsequent evidence, with ensuing confusion and disappointment".

Acknowledgements

The author would like to acknowledge Dr. Mostapha Ariane, Dr Neil Reez, Mr. Mostapha Iqbal for their collaborations in the published articles.

REFERENCES

Abd-Elhady, A.A. and Sallam, H.E.-D.M. (2016) "Effect of Poisson's Ratio on Stress/Strain Concentration at Circular Holes in Elastic Plates Subjected to Biaxial Loading — Three Dimensional Finite Element Analysis." In Ikhmayies, S.J., Li, B., Carpenter, J.S., et al. (eds.) *Characterization of Minerals, Metals, and Materials 2016*. Cham: Springer International Publishing. pp. 45–55. doi:10.1007/978-3-319-48210-1_6.

Ackland, G.J. and Bonny, G. (2020) "Interatomic Potential Development." In *Comprehensive Nuclear Materials*. Elsevier. pp. 544–572. doi:10.1016/B978-0-12-803581-8.11687-X.

Ahmed, S.A. and Giddens, D.P. (1984) Pulsatile poststenotic flow studies with laser Doppler anemometry. *Journal of Biomechanics*, 17 (9): 695–705. doi:10.1016/0021-9290(84)90123-4.

Ahrens, J., Geveci, B. and Law, C. (2005) "ParaView: An End-User Tool for Large-Data Visualization." In *Visualization Handbook*. Elsevier. pp. 717–731. doi:10.1016/B978-012387582-2/50038-1.

Albano, A. and Alexiadis, A. (2020) A smoothed particle hydrodynamics study of the collapse for a cylindrical cavity Peters, M.H. (ed.). *PLOS ONE*, 15 (9): e0239830. doi:10.1371/journal.pone.0239830.

Albano, A. and Alexiadis, A. (2021) Non-Symmetrical Collapse of an Empty Cylindrical Cavity Studied with Smoothed Particle Hydrodynamics. *Applied Sciences*, 11 (8): 3500. doi:10.3390/app11083500.

Alexiadis, A. (2014) A smoothed particle hydrodynamics and coarse-grained molecular dynamics hybrid technique for modelling elastic particles and breakable capsules under various flow conditions: SPH-CGMD HYBRID. *International Journal for Numerical Methods in Engineering*, 100 (10): 713–719. doi:10.1002/nme.4782.

Alexiadis, A. (2015a) A new Framework for Modelling the Dynamics and the Breakage of Capsules, Vesicles and Cells in Fluid Flow. *Procedia IUTAM*, 16: 80–88. doi:10.1016/j.piutam.2015.03.010.

Alexiadis, A. (2015b) The Discrete Multi-Hybrid System for the Simulation of Solid-Liquid Flows Aliseda, A. (ed.). *PLOS ONE*, 10 (5): e0124678. doi:10.1371/journal.pone.0124678.

Alexiadis A. (2019). From Discrete Multiphysics to Deep Multiphysics: a case study concerning the design of continuous microfluidic devices for cell separation. hal-02143375

Alexiadis, A. (2019a) Deep Multiphysics and Particle–Neuron Duality: A Computational Framework Coupling (Discrete) Multiphysics and Deep Learning. *Applied Sciences*, 9 (24): 5369. doi:10.3390/app9245369.

Alexiadis, A. (2019b) Deep multiphysics: Coupling discrete multiphysics with machine learning to attain self-learning in-silico models replicating human physiology. *Artificial Intelligence in Medicine*, 98: 27–34. doi:10.1016/j.artmed.2019.06.005.

Alexiadis, A., Ghraybeh, S. and Qiao, G. (2018) Natural convection and solidification of phase-change materials in circular pipes: A SPH approach. *Computational Materials Science*, 150: 475–483. doi:10.1016/j.commatsci.2018.04.037.

Alexiadis, A., Simmons, M.J.H., Stamatopoulos, K., et al. (2020) The duality between particle methods and artificial neural networks. *Scientific Reports*, 10 (1): 16247. doi:10.1038/s41598-020-73329-0.

Alexiadis, A., Simmons, M.J.H., Stamatopoulos, K., et al. (2021) The virtual physiological human gets nerves! How to account for the action of the nervous system in multiphysics simulations of human organs. *Journal of The Royal Society Interface*, 18 (177): rsif.2020.1024, 20201024. doi:10.1098/rsif.2020.1024.

Alexiadis, A., Stamatopoulos, K., Wen, W., et al. (2017) Using discrete multi-physics for detailed exploration of hydrodynamics in an in vitro colon system. *Computers in Biology and Medicine*, 81: 188–198. doi:10.1016/j.compbiomed.2017.01.003.

Alqahtani, A., suwaidi, J. and Mohsen, M. (2013) Stent fracture: How frequently is it recognized? *Heart Views*, 14 (2): 72. doi:10.4103/1995-705X.115501.

Amindari, A., Saltik, L., Kirkkopru, K., et al. (2017) Assessment of calcified aortic valve leaflet deformations and blood flow dynamics using fluid-structure interaction modeling. *Informatics in Medicine Unlocked*, 9: 191–199. doi:10.1016/j.imu.2017.09.001.

Ariane, M., Allouche, M.H., Bussone, M., et al. (2017a) Discrete multi-physics: A mesh-free model of blood flow in flexible biological valve including solid aggregate formation Gao, Z.-K. (ed.). *PLOS ONE*, 12 (4): e0174795. doi:10.1371/journal.pone.0174795.

Ariane, M., Kassinos, S., Velaga, S., et al. (2018a) Discrete multi-physics simulations of diffusive and convective mass transfer in boundary layers containing motile cilia in lungs. *Computers in Biology and Medicine*, 95: 34–42. doi:10.1016/j.compbiomed.2018.01.010.

Ariane, M., Vigolo, D., Brill, A., et al. (2018b) Using Discrete Multi-Physics for studying the dynamics of emboli in flexible venous valves. *Computers & Fluids*, 166: 57–63. doi:10.1016/j.compfluid.2018.01.037.

Ariane, M., Wen, W., Vigolo, D., et al. (2017b) Modelling and simulation of flow and agglomeration in deep veins valves using discrete multi physics. *Computers in Biology and Medicine*, 89: 96–103. doi:10.1016/j.compbiomed.2017.07.020.

Arjunon, S., Rathan, S., Jo, H., et al. (2013) Aortic Valve: Mechanical Environment and Mechanobiology. *Annals of Biomedical Engineering*, 41 (7): 1331–1346. doi:10.1007/s10439-013-0785-7.

Armengaud, E., Watzenig, D., Karner, M., et al. (2009) Combining the Advantages of Simulation and Prototyping for the Validation of Dependable Communication Architectures: the TEODACS Approach. *SAE International Journal of Passenger Cars - Electronic and Electrical Systems*, 2 (1): 309–318. doi:10.4271/2009-01-0763.

Auricchio, F., Conti, M., Morganti, S., et al. (2014) Simulation of transcatheter aortic valve implantation: a patient-specific finite element approach. *Computer Methods in Biomechanics and Biomedical Engineering*, 17 (12): 1347–1357. doi:10.1080/10255842.2012.746676.

Bach, D.S., Radeva, J.I., Birnbaum, H.G., et al. (2007) Prevalence, referral patterns, testing, and surgery in aortic valve disease: leaving women and elderly patients behind? *The Journal of Heart Valve Disease*, 16 (4): 362–369.

Badimon, L., Padró, T. and Vilahur, G. (2012) Atherosclerosis, platelets and thrombosis in acute ischaemic heart disease. *European Heart Journal: Acute Cardiovascular Care*, 1 (1): 60–74. doi:10.1177/2048872612441582.

Balossino, R., Gervaso, F., Migliavacca, F., et al. (2008) Effects of different stent designs on local hemodynamics in stented arteries. *Journal of Biomechanics*, 41 (5): 1053–1061. doi:10.1016/j.jbiomech.2007.12.005.

Banks, J. (ed.) (2001) *Discrete-event system simulation*. Prentice-Hall international series in industrial and systems engineering. 3rd ed. Upper Saddle River, NJ: Prentice Hall.

Bard, A.J. and Faulkner, L.R. (2001) *Electrochemical Methods: Fundamentals and Applications*. 2nd ed. New York: Wiley.

Bavo, A.M., Rocatello, G., Iannaccone, F., et al. (2016) Fluid-Structure Interaction Simulation of Prosthetic Aortic Valves: Comparison between Immersed Boundary and Arbitrary Lagrangian-Eulerian Techniques for the Mesh Representation Borazjani, I. (ed.). *PLOS ONE*, 11 (4): e0154517. doi:10.1371/journal.pone.0154517.

Bayles, M.P., Swank, A.M. and American College of Sports Medicine (eds.) (2018) *ACSM's exercise testing and prescription*. First edition. Philadelphia: Wolters Kluwer.

Beier, S., Ormiston, J., Webster, M., et al. (2016) Hemodynamics in Idealized Stented Coronary Arteries: Important Stent Design Considerations. *Annals of Biomedical Engineering*, 44 (2): 315–329. doi:10.1007/s10439-015-1387-3.

Belytschko, T., Krongauz, Y., Organ, D., et al. (1996) Meshless methods: An overview and recent developments. *Computer Methods in Applied Mechanics and Engineering*, 139 (1–4): 3–47. doi:10.1016/S0045-7825(96)01078-X.

Bermejo, J., Rojo-Álvarez, J.L., Antoranz, J.C., et al. (2004) Estimation of the End of Ejection in Aortic Stenosis: An Unreported Source of Error in the Invasive Assessment of Severity. *Circulation*, 110 (9): 1114–1120. doi:10.1161/01.CIR.0000139846.66047.62.

Blais, C., Burwash, I.G., Mundigler, G., et al. (2006) Projected Valve Area at Normal Flow Rate Improves the Assessment of Stenosis Severity in Patients With Low-Flow, Low-Gradient Aortic Stenosis: The Multicenter TOPAS (Truly or Pseudo-Severe Aortic Stenosis) Study. *Circulation*, 113 (5): 711–721. doi:10.1161/CIRCULATIONAHA.105.557678.

Blais, C., Pibarot, P., Dumesnil, J.G., et al. (2001) Comparison of valve resistance with effective orifice area regarding flow dependence. *The American Journal of Cardiology*, 88 (1): 45–52. doi:10.1016/S0002-9149(01)01584-3.

Bluestein, D. and Einav, S. (1995) The effect of varying degrees of stenosis on the characteristics of turbulent pulsatile flow through heart valves. *Journal of Biomechanics*, 28 (8): 915–924. doi:10.1016/0021-9290(94)00154-V.

Boland, E.L., Grogan, J.A., Conway, C., et al. (2016) Computer Simulation of the Mechanical Behaviour of Implanted Biodegradable Stents in a Remodelling Artery. *JOM*, 68 (4): 1198–1203. doi:10.1007/s11837-015-1761-5.

Box, G.E.P. (1999) Statistics as a Catalyst to Learning by Scientific Method Part II—A Discussion. *Journal of Quality Technology*, 31 (1): 16–29. doi:10.1080/00224065.1999.11979890.

Brely, L., Bosia, F. and Pugno, N.M. (2015) A Hierarchical Lattice Spring Model to Simulate the Mechanics of 2-D Materials-Based Composites. *Frontiers in Materials*, 2. doi:10.3389/fmats.2015.00051.

Brown, J.C., Gerhardt, T.E. and Kwon, E. (2021) "Risk Factors For Coronary Artery Disease." In *StatPearls*. Treasure Island (FL): StatPearls Publishing. Available at: http://www.ncbi.nlm.nih.gov/books/NBK554410/ (Downloaded: 24 August 2021).

Bruce, J.W. and Giblin, P.J. (1992) *Curves and singularities: a geometrical introduction to singularity theory*. 2nd ed. Cambridge [England] ; New York, NY, USA: Cambridge University Press.

Buccheri, D., Piraino, D., Andolina, G., et al. (2016) Understanding and managing in-stent restenosis: a review of clinical data, from pathogenesis to treatment. *Journal of Thoracic Disease*, 8 (10): E1150–E1162. doi:10.21037/jtd.2016.10.93.

Caiazzo, A., Evans, D., Falcone, J.-L., et al. (2011) A Complex Automata approach for in-stent restenosis: Two-dimensional multiscale modelling and simulations. *Journal of Computational Science*, 2 (1): 9–17. doi:10.1016/j.jocs.2010.09.002.

Capasso, S., Tagliafierro, B., Güzel, H., et al. (2021) A Numerical Validation of 3D Experimental Dam-Break Wave Interaction with a Sharp Obstacle Using DualSPHysics. *Water*, 13 (15): 2133. doi:10.3390/w13152133.

Cassar, A., Holmes, D.R., Rihal, C.S., et al. (2009) Chronic Coronary Artery Disease: Diagnosis and Management. *Mayo Clinic Proceedings*, 84 (12): 1130–1146. doi:10.4065/mcp.2009.0391.

Chaudhry, R., Miao, J.H. and Rehman, A. (2022) "Physiology, Cardiovascular." In *StatPearls*. Treasure Island (FL): StatPearls Publishing. Available at: http://www.ncbi.nlm.nih.gov/books/NBK493197/ (Downloaded: 11 May 2022).

Cheung, Y. (2010) "Systemic Circulation." In *Paediatric Cardiology*. Elsevier. pp. 91–116. doi:10.1016/B978-0-7020-3064-2.00006-0.

Chinikar, M. and Sadeghipour, P. (2014) Coronary Stent Fracture: A Recently Appreciated Phenomenon with Clinical Relevance. *Current Cardiology Reviews*, 10 (4): 349–354. doi:10.2174/1573403X10666140404105923.

Choudhury, T.R., Al-Saigh, S., Burley, S., et al. (2017) Longitudinal deformation bench testing using a coronary artery model: a new standard? *Open Heart*, 4 (2): e000537. doi:10.1136/openhrt-2016-000537.

Colombo, A., Stankovic, G. and Moses, J.W. (2002) Selection of coronary stents. *Journal of the American College of Cardiology*, 40 (6): 1021–1033. doi:10.1016/S0735-1097(02)02123-X.

Cosmi, J.E., Kort, S., Tunick, P.A., et al. (2002) The risk of the development of aortic stenosis in patients with "benign" aortic valve thickening. *Archives of Internal Medicine*, 162 (20): 2345–2347. doi:10.1001/archinte.162.20.2345.

Cutress, I.J., Dickinson, E.J.F. and Compton, R.G. (2010) Analysis of commercial general engineering finite element software in electrochemical simulations. *Journal of Electroanalytical Chemistry*, 638 (1): 76–83. doi:10.1016/j.jelechem.2009.10.017.

Davies, T.J. and Compton, R.G. (2005) The cyclic and linear sweep voltammetry of regular and random arrays of microdisc electrodes: Theory. *Journal of Electroanalytical Chemistry*, 585 (1): 63–82. doi:10.1016/j.jelechem.2005.07.022.

Daxini, S.D. and Prajapati, J.M. (2014) A Review on Recent Contribution of Meshfree Methods to Structure and Fracture Mechanics Applications. *The Scientific World Journal*, 2014: 1–13. doi:10.1155/2014/247172.

Desrues, J., Argilaga, A., Caillerie, D., et al. (2019) From discrete to continuum modelling of boundary value problems in geomechanics: An integrated FEM-DEM approach. *International Journal for Numerical and Analytical Methods in Geomechanics*, 43 (5): 919–955. doi:10.1002/nag.2914.

Di Lisio, R., Grenier, E. and Pulvirenti, M. (1998) The convergence of the SPH method. *Computers & Mathematics with Applications*, 35 (1–2): 95–102. doi:10.1016/S0898-1221(97)00260-5.

Di Venuta, I., Boghi, A. and Gori, F. (2017) Three-dimensional numerical simulation of a failed coronary stent implant at different degrees of residual stenosis. Part I: Fluid dynamics and shear stress on the vascular wall. *Numerical Heat Transfer, Part A: Applications*, 71 (6): 638–652. doi:10.1080/10407782.2017.1293985.

Dickinson, E.J.F., Streeter, I. and Compton, R.G. (2008) Chronoamperometry and Cyclic Voltammetry at Conical Electrodes, Microelectrodes, and Electrode Arrays: Theory. *The Journal of Physical Chemistry B*, 112 (13): 4059–4066. doi:10.1021/jp711936y.

Ding, H., Zhang, Y., Liu, Y., et al. (2019) Analysis of Vascular Mechanical Characteristics after Coronary Degradable Stent Implantation. *BioMed Research International*, 2019: 1–9. doi:10.1155/2019/8265374.

DISCRETE MULTIPHYSICS: modelling complex systems with particle methods. (2021). S.l.: MDPI AG.

Duraiswamy, N., Jayachandran, B., Byrne, J., et al. (2005) Spatial Distribution of Platelet Deposition in Stented Arterial Models Under Physiologic Flow. *Annals of Biomedical Engineering*, 33 (12): 1767–1777. doi:10.1007/s10439-005-7598-2.

Escalera-López, D., Griffin, R., Isaacs, M., et al. (2017) Electrochemical sulfidation of WS 2 nanoarrays: Strong dependence of hydrogen evolution activity on transition metal sulfide surface composition. *Electrochemistry Communications*, 81: 106–111. doi:10.1016/j.elecom.2017.06.016.

Everett, K.D., Conway, C., Desany, G.J., et al. (2016) Structural Mechanics Predictions Relating to Clinical Coronary Stent Fracture in a 5 Year Period in FDA MAUDE Database. *Annals of Biomedical Engineering*, 44 (2): 391–403. doi:10.1007/s10439-015-1476-3.

Evju, Ø. and Mardal, K.-A. (2015) "On the Assumption of Laminar Flow in Physiological Flows: Cerebral Aneurysms as an Illustrative Example." In Quarteroni, A. (ed.) *Modeling the Heart and the Circulatory System*. MS&A. Cham: Springer International Publishing. pp. 177–195. doi:10.1007/978-3-319-05230-4_7.

Faik, I., Mongrain, R., Leask, R.L., et al. (2007) Time-dependent 3D simulations of the hemodynamics in a stented coronary artery. *Biomedical Materials*, 2 (1): S28–S37. doi:10.1088/1748-6041/2/1/S05.

Fedele, M., Faggiano, E., Dedè, L., et al. (2017) A patient-specific aortic valve model based on moving resistive immersed implicit surfaces. *Biomechanics and Modeling in Mechanobiology*, 16 (5): 1779–1803. doi:10.1007/s10237-017-0919-1.

Feldberg, S.W. (2010) Implications of Marcus−Hush Theory for Steady-State Heterogeneous Electron Transfer at an Inlaid Disk Electrode. *Analytical Chemistry*, 82 (12): 5176–5183. doi:10.1021/ac1004162.

Finet, G. and Rioufol, G. (2012) Coronary stent longitudinal deformation by compression: is this a new global stent failure, a specific failure of a particular stent design or simply an angiographic detection of an exceptional PCI complication? *EuroIntervention*, 8 (2): 177–181. doi:10.4244/EIJV8I2A29.

Fioretta, E.S., Dijkman, P.E., Emmert, M.Y., et al. (2018) The future of heart valve replacement: recent developments and translational challenges for heart valve tissue engineering: The future of heart valve replacement. *Journal of Tissue Engineering and Regenerative Medicine*, 12 (1): e323–e335. doi:10.1002/term.2326.

Fischbacher, T. and Fangohr, H. (2009) Continuum multi-physics modeling with scripting languages: the Nsim simulation compiler prototype for classical field theory. *arXiv:0907.1587 [cond-mat, physics:physics]*. Available at: http://arxiv.org/abs/0907.1587 (Accessed: 30 April 2019).

Fogler, H.S. (2006) *Elements of chemical reaction engineering*. Prentice Hall PTR international series in the physical and chemical engineering sciences. 4th ed. Upper Saddle River, NJ: Prentice Hall PTR.

Fulk, D.A. and Quinn, D.W. (1996) An Analysis of 1-D Smoothed Particle Hydrodynamics Kernels. *Journal of Computational Physics*, 126 (1): 165–180. doi:10.1006/jcph.1996.0128.

Geuzaine, C. and Remacle, J.-F. (2009) Gmsh: A 3-D finite element mesh generator with built-in pre- and post-processing facilities. *International Journal for Numerical Methods in Engineering*, 79 (11): 1309–1331. doi:10.1002/nme.2579.

Ghasemi Bahraseman, H., Mohseni Languri, E., Yahyapourjalaly, N., et al. (2016) Fluid–structure interaction modeling of aortic valve stenosis at different heart rates. *Acta of Bioengineering and Biomechanics; 03/2016; ISSN 1509-409X*. doi:10.5277/abb-00429-2015-03.

Gingold, R.A. and Monaghan, J.J. (1977) Smoothed particle hydrodynamics: theory and application to non-spherical stars. *Monthly Notices of the Royal Astronomical Society*, 181 (3): 375–389. doi:10.1093/mnras/181.3.375.

Gott, S.C., Jabola, B.A. and Rao, M.P. (2015) Vascular stents with submicrometer-scale surface patterning realized via titanium deep reactive ion etching. *Journal of Micromechanics and Microengineering*, 25 (8): 085016. doi:10.1088/0960-1317/25/8/085016.

Griffith, M.D., Leweke, T., Thompson, M.C., et al. (2013) Effect of small asymmetries on axisymmetric stenotic flow. *Journal of Fluid Mechanics*, 721: R1. doi:10.1017/jfm.2013.109.

Hajar, R. (2017) Risk factors for coronary artery disease: Historical perspectives. *Heart Views*, 18 (3): 109. doi:10.4103/HEARTVIEWS.HEARTVIEWS_106_17.

Hamid, M.S., Sabbah, H.N. and Stein, P.D. (1985) Comparison of finite element stress analysis of aortic valve leaflet using either membrane elements or solid elements. *Computers & Structures*, 20 (6): 955–961. doi:10.1016/0045-7949(85)90015-X.

Hammer, P.E., Sacks, M.S., del Nido, P.J., et al. (2011) Mass-Spring Model for Simulation of Heart Valve Tissue Mechanical Behavior. *Annals of Biomedical Engineering*, 39 (6): 1668–1679. doi:10.1007/s10439-011-0278-5.

Harewood, F., Grogan, J. and McHUGH, P. (2010) A MULTISCALE APPROACH TO FAILURE ASSESSMENT IN DEPLOYMENT FOR CARDIOVASCULAR STENTS. *Journal of Multiscale Modelling*, 02 (01n02): 1–22. doi:10.1142/S1756973710000278.

Hartley, A., Hammond-Haley, M., Marshall, D.C., et al. (2021) Trends in Mortality From Aortic Stenosis in Europe: 2000–2017. *Frontiers in Cardiovascular Medicine*, 8: 748137. doi:10.3389/fcvm.2021.748137.

Hopp-Hirschler, M., Shadloo, M.S. and Nieken, U. (2018) A Smoothed Particle Hydrodynamics approach for thermo-capillary flows. *Computers & Fluids*, 176: 1–19. doi:10.1016/j.compfluid.2018.09.010.

Hsiao, H.-M., Lee, K.-H., Liao, Y.-C., et al. (2012) Hemodynamic Simulation of Intra-stent Blood Flow. *Procedia Engineering*, 36: 128–136. doi:10.1016/j.proeng.2012.03.020.

Huntley, G.D., Thaden, J.J., Alsidawi, S., et al. (2018) Comparative study of bicuspid vs. tricuspid aortic valve stenosis. *European Heart Journal - Cardiovascular Imaging*, 19 (1): 3–8. doi:10.1093/ehjci/jex211.

Huo, Y. and Kassab, G.S. (2006) Pulsatile blood flow in the entire coronary arterial tree: theory and experiment. *American Journal of Physiology-Heart and Circulatory Physiology*, 291 (3): H1074–H1087. doi:10.1152/ajpheart.00200.2006.

Ioannidis, J.P.A. (2005) Why Most Published Research Findings Are False. *PLoS Medicine*, 2 (8): e124. doi:10.1371/journal.pmed.0020124.

Jain, K. (2020) Transition to turbulence in an oscillatory flow through stenosis. *Biomechanics and Modeling in Mechanobiology*, 19 (1): 113–131. doi:10.1007/s10237-019-01199-1.

Jarvis S (2018) Vascular system 1: anatomy and physiology. Nursing Times [online]; 114: 4, 40-44. Accessed on 11th may, 2022.

Jenner C. (2012). A Systematic Modelling Approach. Retrieved at: http://processprinciples.com/2012/05/a-systematic-modelling-approach/. Accessed on 22/02/2021.

Jeoung, E., Galow, T.H., Schotter, J., et al. (2001) Fabrication and Characterization of Nanoelectrode Arrays Formed via Block Copolymer Self-Assembly. *Langmuir*, 17 (21): 6396–6398. doi:10.1021/la010531g.

Jermihov, P.N., Jia, L., Sacks, M.S., et al. (2011) Effect of Geometry on the Leaflet Stresses in Simulated Models of Congenital Bicuspid Aortic Valves. *Cardiovascular Engineering and Technology*, 2 (1): 48–56. doi:10.1007/s13239-011-0035-9.

Ji, S., Chen, X. and Liu, L. (2019) Coupled DEM-SPH Method for Interaction between Dilated Polyhedral Particles and Fluid. *Mathematical Problems in Engineering*, 2019: 1–11. doi:10.1155/2019/4987801.

Ji, Z., Liu, L. and Wang, Y. (2010) B-Mesh: A Modeling System for Base Meshes of 3D Articulated Shapes. *Computer Graphics Forum*, 29 (7): 2169–2177. doi:10.1111/j.1467-8659.2010.01805.x.

Jiménez, J.M. and Davies, P.F. (2009) Hemodynamically Driven Stent Strut Design. *Annals of Biomedical Engineering*, 37 (8): 1483–1494. doi:10.1007/s10439-009-9719-9.

Kaizer, J.S., Heller, A.K. and Oberkampf, W.L. (2015) Scientific computer simulation review. *Reliability Engineering & System Safety*, 138: 210–218. doi:10.1016/j.ress.2015.01.020.

Kamimura, D., Hans, S., Suzuki, T., et al. (2016) Delayed Time to Peak Velocity Is Useful for Detecting Severe Aortic Stenosis. *Journal of the American Heart Association*, 5 (10). doi:10.1161/JAHA.116.003907.

Kandzari, D.E., Leon, M.B., Meredith, I., et al. (2013) Final 5-Year Outcomes From the Endeavor Zotarolimus-Eluting Stent Clinical Trial Program. *JACC: Cardiovascular Interventions*, 6 (5): 504–512. doi:10.1016/j.jcin.2012.12.125.

Khalilimeybodi, A., Alishzadeh Khoei, A. and Sharif-Kashani, B. (2020) Future Balloon-Expandable Stents: High or Low-Strength Materials? *Cardiovascular Engineering and Technology*, 11 (2): 188–204. doi:10.1007/s13239-019-00450-1.

Kolodgie, F.D., Nakazawa, G., Sangiorgi, G., et al. (2007) Pathology of Atherosclerosis and Stenting. *Neuroimaging Clinics of North America*, 17 (3): 285–301. doi:10.1016/j.nic.2007.03.006.

Kot, M. (2021) Mass Spring Models of Amorphous Solids. *ChemEngineering*, 5 (1): 3. doi:10.3390/chemengineering5010003.

Kot, M., Nagahashi, H. and Szymczak, P. (2015) Elastic moduli of simple mass spring models. *The Visual Computer*, 31 (10): 1339–1350. doi:10.1007/s00371-014-1015-5.

Krzhizhanovskaya, V.V. and Sun, S. (2007) "Simulation of Multiphysics Multiscale Systems: Introduction to the ICCS'2007 Workshop." In Shi, Y., van Albada, G.D., Dongarra, J., et al. (eds.) *Computational Science – ICCS 2007*. Berlin, Heidelberg: Springer Berlin Heidelberg. pp. 755–761. doi:10.1007/978-3-540-72584-8_100.

Ku, D.N. (1997) BLOOD FLOW IN ARTERIES. *Annual Review of Fluid Mechanics*, 29 (1): 399–434. doi:10.1146/annurev.fluid.29.1.399.

Lally, C., Dolan, F. and Prendergast, P.J. (2005) Cardiovascular stent design and vessel stresses: a finite element analysis. *Journal of Biomechanics*, 38 (8): 1574–1581. doi:10.1016/j.jbiomech.2004.07.022.

Lazaros, G., Drakopoulou, M.I. and Tousoulis, D. (2018) Transaortic Flow in Aortic Stenosis: Stroke Volume Index versus Flow Rate. *Cardiology*, 141 (1): 71–73. doi:10.1159/000494051.

Lee, W. and Jung, E. (2015) A Multiscale Model of Cardiovascular System Including an Immersed Whole Heart in the Cases of Normal and Ventricular Septal Defect (VSD). *Bulletin of Mathematical Biology*, 77 (7): 1349–1376. doi:10.1007/s11538-015-0088-2.

Leon, M.B., Mauri, L., Popma, J.J., et al. (2010) A Randomized Comparison of the Endeavor Zotarolimus-Eluting Stent Versus the TAXUS Paclitaxel-Eluting Stent in De Novo Native Coronary Lesions. *Journal of the American College of Cardiology*, 55 (6): 543–554. doi:10.1016/j.jacc.2009.08.067.

Leopold, J.A. (2013) Vascular calcification: an age-old problem of old age. *Circulation*, 127 (24): 2380–2382. doi:10.1161/CIRCULATIONAHA.113.003341.

Levich, V.G. (1962) *Physiochemical hydrodynamics*. Englewood Cliffs, N.J.: Prentice-Hall.

Li, D., Zhen, Z., Zhang, H., et al. (2019) Numerical Model of Oil Film Diffusion in Water Based on SPH Method. *Mathematical Problems in Engineering*, 2019: 1–14. doi:10.1155/2019/8250539.

Lind, S.J., Rogers, B.D. and Stansby, P.K. (2020) Review of smoothed particle hydrodynamics: towards converged Lagrangian flow modelling. *Proceedings of the Royal*

Society A: Mathematical, Physical and Engineering Sciences, 476 (2241): 20190801. doi:10.1098/rspa.2019.0801.

Liu, G.R. and Liu, M.B. (2003) *Smoothed particle hydrodynamics: a meshfree particle method*. New Jersey: World Scientific.

Liu, M.B. and Liu, G.R. (2006) Restoring particle consistency in smoothed particle hydrodynamics. *Applied Numerical Mathematics*, 56 (1): 19–36. doi:10.1016/j.apnum.2005.02.012.

Liu, W. and Wu, C.-Y. (2020) Modelling Complex Particle–Fluid Flow with a Discrete Element Method Coupled with Lattice Boltzmann Methods (DEM-LBM). *ChemEngineering*, 4 (4): 55. doi:10.3390/chemengineering4040055.

Liu, Z. (2018) *Multiphysics in porous materials*.

Lloyd, B., Szekely, G. and Harders, M. (2007) Identification of Spring Parameters for Deformable Object Simulation. *IEEE Transactions on Visualization and Computer Graphics*, 13 (5): 1081–1094. doi:10.1109/TVCG.2007.1055.

Lucy, L.B. (1977) A numerical approach to the testing of the fission hypothesis. *The Astronomical Journal*, 82: 1013. doi:10.1086/112164.

Lüscher, T.F. (2018) Performance of modern stents in stable and acute coronary disease. *European Heart Journal*, 39 (26): 2435–2438. doi:10.1093/eurheartj/ehy393.

Lyly et al (1999) *ELMER - A finite element solver for multiphysics.* CSC-report on scientific computing 2000.

Mahmood, S.S., Levy, D., Vasan, R.S., et al. (2014) The Framingham Heart Study and the epidemiology of cardiovascular disease: a historical perspective. *The Lancet*, 383 (9921): 999–1008. doi:10.1016/S0140-6736(13)61752-3.

Malakar, A.Kr., Choudhury, D., Halder, B., et al. (2019) A review on coronary artery disease, its risk factors, and therapeutics. *Journal of Cellular Physiology*, 234 (10): 16812–16823. doi:10.1002/jcp.28350.

Masci, P.G., Dymarkowski, S. and Bogaert, J. (2008) Valvular heart disease: what does cardiovascular MRI add? *European Radiology*, 18 (2): 197–208. doi:10.1007/s00330-007-0731-x.

Mauri, L., Massaro, J.M., Jiang, S., et al. (2010) Long-Term Clinical Outcomes With Zotarolimus-Eluting Versus Bare-Metal Coronary Stents. *JACC: Cardiovascular Interventions*, 3 (12): 1240–1249. doi:10.1016/j.jcin.2010.08.021.

Mayo clinic (2019). Aortic valve stenosis. Retrieved at: https://www.mayoclinic.org/diseases-conditions/aortic-stenosis/symptoms-causes/syc-20353139. Accessed on 02/09/2019.

Michelena, H.I., Prakash, S.K., Della Corte, A., et al. (2014) Bicuspid Aortic Valve: Identifying Knowledge Gaps and Rising to the Challenge From the International Bicuspid

Aortic Valve Consortium (BAVCon). *Circulation*, 129 (25): 2691–2704. doi:10.1161/CIRCULATIONAHA.113.007851.

Mohammed, A.M., Ariane, M. and Alexiadis, A. (2020) Using Discrete Multiphysics Modelling to Assess the Effect of Calcification on Hemodynamic and Mechanical Deformation of Aortic Valve. *ChemEngineering*, 4 (3): 48. doi:10.3390/chemengineering4030048.

Mohammed, A.M., Ariane, M. and Alexiadis, A. (2021) Fluid-Structure Interaction in Coronary Stents: A Discrete Multiphysics Approach. *ChemEngineering*, 5 (3): 60. doi:10.3390/chemengineering5030060.

Mohammed, A.M., Iqbal, M., Rees, N.V., et al. (2019) Computational study of mass transfer at surfaces structured with reactive nanocones. *Applied Mathematical Modelling*, 74: 373–386. doi:10.1016/j.apm.2019.04.057.

Monaghan, J.J. (1992) Smoothed Particle Hydrodynamics. *Annual Review of Astronomy and Astrophysics*, 30 (1): 543–574. doi:10.1146/annurev.aa.30.090192.002551.

Monaghan, J.J. (1994) Simulating Free Surface Flows with SPH. *Journal of Computational Physics*, 110 (2): 399–406. doi:10.1006/jcph.1994.1034.

Monaghan, J.J. (2012) Smoothed Particle Hydrodynamics and Its Diverse Applications. *Annual Review of Fluid Mechanics*, 44 (1): 323–346. doi:10.1146/annurev-fluid-120710-101220.

Moravej, M. and Mantovani, D. (2011) Biodegradable Metals for Cardiovascular Stent Application: Interests and New Opportunities. *International Journal of Molecular Sciences*, 12 (7): 4250–4270. doi:10.3390/ijms12074250.

Morganti, S., Conti, M., Aiello, M., et al. (2014) Simulation of transcatheter aortic valve implantation through patient-specific finite element analysis: Two clinical cases. *Journal of Biomechanics*, 47 (11): 2547–2555. doi:10.1016/j.jbiomech.2014.06.007.

Morice, M.-C., Serruys, P.W., Barragan, P., et al. (2007) Long-Term Clinical Outcomes With Sirolimus-Eluting Coronary Stents. *Journal of the American College of Cardiology*, 50 (14): 1299–1304. doi:10.1016/j.jacc.2007.06.029.

Morice, M.-C., Serruys, P.W., Sousa, J.E., et al. (2002) A Randomized Comparison of a Sirolimus-Eluting Stent with a Standard Stent for Coronary Revascularization. *New England Journal of Medicine*, 346 (23): 1773–1780. doi:10.1056/NEJMoa012843.

Morris, J.P., Fox, P.J. and Zhu, Y. (1997) Modeling Low Reynolds Number Incompressible Flows Using SPH. *Journal of Computational Physics*, 136 (1): 214–226. doi:10.1006/jcph.1997.5776.

Mortier, P., De Beule, M., Van Loo, D., et al. (2009) Finite element analysis of side branch access during bifurcation stenting. *Medical Engineering & Physics*, 31 (4): 434–440. doi:10.1016/j.medengphy.2008.11.013.

Mullany, C.J. (2003) Coronary Artery Bypass Surgery. *Circulation*, 107 (3). doi:10.1161/01.CIR.0000048896.72317.49.

Müller, M., Schirm, S., Teschner, M., et al. (2004) Interaction of fluids with deformable solids. *Computer Animation and Virtual Worlds*, 15 (34): 159–171. doi:10.1002/cav.18.

Murgo, J.P., Westerhof, N., Giolma, J.P., et al. (1980) Aortic input impedance in normal man: relationship to pressure wave forms. *Circulation*, 62 (1): 105–116. doi:10.1161/01.CIR.62.1.105.

Murphy, B.P., Savage, P., McHugh, P.E., et al. (2003) The Stress–Strain Behavior of Coronary Stent Struts is Size Dependent. *Annals of Biomedical Engineering*, 31 (6): 686–691. doi:10.1114/1.1569268.

Myerson, S.G. (2012) Heart valve disease: investigation by cardiovascular magnetic resonance. *Journal of Cardiovascular Magnetic Resonance*, 14 (1): 7. doi:10.1186/1532-429X-14-7.

Newman, J.S. and Thomas-Alyea, K.E. (2004) *Electrochemical systems*. 3rd ed. Hoboken, N.J: J. Wiley.

Ng, K.C., Alexiadis, A., Chen, H., et al. (2020) A coupled Smoothed Particle Hydrodynamics-Volume Compensated Particle Method (SPH-VCPM) for Fluid Structure Interaction (FSI) modelling. *Ocean Engineering*, 218: 107923. doi:10.1016/j.oceaneng.2020.107923.

O'Brien, B.J., Stinson, J.S., Larsen, S.R., et al. (2010) A platinum–chromium steel for cardiovascular stents. *Biomaterials*, 31 (14): 3755–3761. doi:10.1016/j.biomaterials.2010.01.146.

Oja, S.M., Wood, M. and Zhang, B. (2013) Nanoscale Electrochemistry. *Analytical Chemistry*, 85 (2): 473–486. doi:10.1021/ac3031702.

Olvera Lopez, E., Ballard, B.D. and Jan, A. (2022) "Cardiovascular Disease." In *StatPearls*. Treasure Island (FL): StatPearls Publishing. Available at: http://www.ncbi.nlm.nih.gov/books/NBK535419/ (Downloaded: 4 August 2022).

Otsuka, F., Yasuda, S., Noguchi, T., et al. (2016) Pathology of coronary atherosclerosis and thrombosis. *Cardiovascular Diagnosis and Therapy*, 6 (4): 396–408. doi:10.21037/cdt.2016.06.01.

Otto, C.M. and Prendergast, B. (2014) Aortic-Valve Stenosis — From Patients at Risk to Severe Valve Obstruction. *New England Journal of Medicine*, 371 (8): 744–756. doi:10.1056/NEJMra1313875.

Pant, S., Bressloff, N.W., Forrester, A.I.J., et al. (2010) The Influence of Strut-Connectors in Stented Vessels: A Comparison of Pulsatile Flow Through Five Coronary Stents. *Annals of Biomedical Engineering*, 38 (5): 1893–1907. doi:10.1007/s10439-010-9962-0.

Pant, S., Bressloff, N.W. and Limbert, G. (2012) Geometry parameterization and multidisciplinary constrained optimization of coronary stents. *Biomechanics and Modeling in Mechanobiology*, 11 (1–2): 61–82. doi:10.1007/s10237-011-0293-3.

Parisi, A.F., Folland, E.D. and Hartigan, P. (1992) A Comparison of Angioplasty with Medical Therapy in the Treatment of Single-Vessel Coronary Artery Disease. *New England Journal of Medicine*, 326 (1): 10–16. doi:10.1056/NEJM199201023260102.

Pazdniakou, A. and Adler, P.M. (2012) Lattice Spring Models. *Transport in Porous Media*, 93 (2): 243–262. doi:10.1007/s11242-012-9955-6.

Peksen, M. (2018) *Multiphysics modelling: materials, components, and systems*. London: Academic Press.

Plimpton, S. (1995) Fast Parallel Algorithms for Short-Range Molecular Dynamics. *Journal of Computational Physics*, 117 (1): 1–19. doi:10.1006/jcph.1995.1039.

Rahmat, A., Barigou, M. and Alexiadis, A. (2019a) Deformation and rupture of compound cells under shear: A discrete multiphysics study. *Physics of Fluids*, 31 (5): 051903. doi:10.1063/1.5091999.

Rahmat, A., Barigou, M. and Alexiadis, A. (2019b) Numerical simulation of dissolution of solid particles in fluid flow using the SPH method. *International Journal of Numerical Methods for Heat & Fluid Flow*, 30 (1): 290–307. doi:10.1108/HFF-05-2019-0437.

Rahmat, A., Tofighi, N., Shadloo, M.S., et al. (2014) Numerical simulation of wall bounded and electrically excited Rayleigh–Taylor instability using incompressible smoothed particle hydrodynamics. *Colloids and Surfaces A: Physicochemical and Engineering Aspects*, 460: 60–70. doi:10.1016/j.colsurfa.2014.02.044.

Rahmat, A. and Yildiz, M. (2018) A multiphase ISPH method for simulation of droplet coalescence and electro-coalescence. *International Journal of Multiphase Flow*, 105: 32–44. doi:10.1016/j.ijmultiphaseflow.2018.03.006.

Ribeiro, A.L. and Otto, C.M. (2014) Heartbeat: Highlights from this issue. *Heart*, 100 (22): 1735–1736. doi:10.1136/heartjnl-2014-306915.

Roth, G.A., Mensah, G.A., Johnson, C.O., et al. (2020) Global Burden of Cardiovascular Diseases and Risk Factors, 1990–2019. *Journal of the American College of Cardiology*, 76 (25): 2982–3021. doi:10.1016/j.jacc.2020.11.010.

Ruiz-Riancho, I.N., Alexiadis, A., Zhang, Z., et al. (2021) A Discrete Multi-Physics Model to Simulate Fluid Structure Interaction and Breakage of Capsules Filled with Liquid under Coaxial Load. *Processes*, 9 (2): 354. doi:10.3390/pr9020354.

Saeed, S., Senior, R., Chahal, N.S., et al. (2017) Lower Transaortic Flow Rate Is Associated With Increased Mortality in Aortic Valve Stenosis. *JACC: Cardiovascular Imaging*, 10 (8): 912–920. doi:10.1016/j.jcmg.2017.05.008.

Sahputra, I.H., Alexiadis, A. and Adams, M.J. (2020) A Coarse Grained Model for Viscoelastic Solids in Discrete Multiphysics Simulations. *ChemEngineering*, 4 (2): 30. doi:10.3390/chemengineering4020030.

Sanfilippo, D., Ghiassi, B., Alexiadis, A., et al. (2021) Combined Peridynamics and Discrete Multiphysics to Study the Effects of Air Voids and Freeze-Thaw on the Mechanical Properties of Asphalt. *Materials*, 14 (7): 1579. doi:10.3390/ma14071579.

Schiavone, A., Qiu, T.-Y. and Zhao, L.-G. (2017) Crimping and deployment of metallic and polymeric stents -- finite element modelling. *Vessel Plus*, 1 (1). doi:10.20517/2574-1209.2016.03.

Schütt, M., O'Farrell, C., Stamatopoulos, K., et al. (2022) Simulating the Hydrodynamic Conditions of the Human Ascending Colon: A Digital Twin of the Dynamic Colon Model. *Pharmaceutics*, 14 (1): 184. doi:10.3390/pharmaceutics14010184.

Schütt, M., Stamatopoulos, K., Simmons, M.J.H., et al. (2020) Modelling and simulation of the hydrodynamics and mixing profiles in the human proximal colon using Discrete Multiphysics. *Computers in Biology and Medicine*, 121: 103819. doi:10.1016/j.compbiomed.2020.103819.

Senst, B., Goyal, A., Basit, H., et al. (2022) "Drug Eluting Stent Compounds." In *StatPearls*. Treasure Island (FL): StatPearls Publishing. Available at: http://www.ncbi.nlm.nih.gov/books/NBK537349/ (Downloaded: 28 July 2022).

Serruys, P.W., Kutryk, M.J.B. and Ong, A.T.L. (2006) Coronary-Artery Stents. *New England Journal of Medicine*, 354 (5): 483–495. doi:10.1056/NEJMra051091.

Shadloo, M.S. and Yildiz, M. (2011) Numerical modeling of Kelvin-Helmholtz instability using smoothed particle hydrodynamics. *International Journal for Numerical Methods in Engineering*, 87 (10): 988–1006. doi:10.1002/nme.3149.

Shadloo, M.S., Zainali, A., Sadek, S.H., et al. (2011) Improved Incompressible Smoothed Particle Hydrodynamics method for simulating flow around bluff bodies. *Computer Methods in Applied Mechanics and Engineering*, 200 (9–12): 1008–1020. doi:10.1016/j.cma.2010.12.002.

Shadloo, M.S., Zainali, A. and Yildiz, M. (2013) Simulation of single mode Rayleigh–Taylor instability by SPH method. *Computational Mechanics*, 51 (5): 699–715. doi:10.1007/s00466-012-0746-2.

Sharma, Abhinav & Sharma, Aman. (2014). A Review of Modeling and Simulation Techniques. International Journal for Research in Technological Studies. 1.

Simard, T., Hibbert, B., Ramirez, F.D., et al. (2014) The Evolution of Coronary Stents: A Brief Review. *Canadian Journal of Cardiology*, 30 (1): 35–45. doi:10.1016/j.cjca.2013.09.012.

Sokolowski, J.A. and Banks, C.M. (eds.) (2010) *Modeling and simulation fundamentals: theoretical underpinnings and practical domains*. Hoboken, N.J: John Wiley.

Stevens, J.R., Zamani, A., Osborne, J.I.A., et al. (2021) Critical evaluation of stents in coronary angioplasty: a systematic review. *BioMedical Engineering OnLine*, 20 (1): 46. doi:10.1186/s12938-021-00883-7.

Stevens, S.A., Lakin, W.D. and Goetz, W. (2003) A differentiable, periodic function for pulsatile cardiac output based on heart rate and stroke volume. *Mathematical Biosciences*, 182 (2): 201–211. doi:10.1016/S0025-5564(02)00200-6.

Stewart, J., Manmathan, G. and Wilkinson, P. (2017) Primary prevention of cardiovascular disease: A review of contemporary guidance and literature. *JRSM Cardiovascular Disease*, 6: 204800401668721. doi:10.1177/2048004016687211.

Stone, G.W., Ellis, S.G., Cox, D.A., et al. (2004) A Polymer-Based, Paclitaxel-Eluting Stent in Patients with Coronary Artery Disease. *New England Journal of Medicine*, 350 (3): 221–231. doi:10.1056/NEJMoa032441.

Strange, G.A., Stewart, S., Curzen, N., et al. (2022) Uncovering the treatable burden of severe aortic stenosis in the UK. *Open Heart*, 9 (1): e001783. doi:10.1136/openhrt-2021-001783.

Stukowski, A. (2010) Visualization and analysis of atomistic simulation data with OVITO–the Open Visualization Tool. *Modelling and Simulation in Materials Science and Engineering*, 18 (1): 015012. doi:10.1088/0965-0393/18/1/015012.

Sun, Y., Liu, Y., Liang, Z., et al. (2009) On the Applicability of Conventional Voltammetric Theory to Nanoscale Electrochemical Interfaces. *The Journal of Physical Chemistry C*, 113 (22): 9878–9883. doi:10.1021/jp902311h.

Swegle, J.W., Hicks, D.L. and Attaway, S.W. (1995) Smoothed Particle Hydrodynamics Stability Analysis. *Journal of Computational Physics*, 116 (1): 123–134. doi:10.1006/jcph.1995.1010.

Thakar, R., Wilburn, J.P. and Baker, L.A. (2011) Studies of Edge Effects with Shroud-Modified Electrodes. *Electroanalysis*, 23 (7): 1543–1547. doi:10.1002/elan.201100170.

Thiriet, M. (2008) *Biology and Mechanics of Blood Flows*. New York, NY: Springer New York. doi:10.1007/978-0-387-74847-4.

Thubrikar, M., Deck, J., Aouad, J., et al. (1983) Role of mechanical stress in calcification of aortic bioprosthetic valves. *The Journal of thoracic and cardiovascular surgery*, 86 (1): 115—125.

Tobias, C. W., Eisenberg, M., and Wilke, C. R. (1952) Diffusion and convection in electrolysis-A Theoretical review. *Journal of electrochemical society*, 99 (12): 359C-365C.

Tran-Duc, T., Phan-Thien, N. and Khoo, B.C. (2017) A smoothed particle hydrodynamics (SPH) study of sediment dispersion on the seafloor. *Physics of Fluids*, 29 (8): 083302. doi:10.1063/1.4993474.

Vamvakidou, A., Chahal, N. and Senior, R. (2017) Lack of Stroke Volume Determined Flow Reserve Does Not Always Preclude Assessment of Severity of Aortic Stenosis in Low-Flow

Low-Gradient State During Dobutamine Echocardiography. *JACC: Cardiovascular Imaging*, 10 (4): 491–493. doi:10.1016/j.jcmg.2016.04.001.

Vamvakidou, A., Jin, W., Danylenko, O., et al. (2019) Low Transvalvular Flow Rate Predicts Mortality in Patients With Low-Gradient Aortic Stenosis Following Aortic Valve Intervention. *JACC: Cardiovascular Imaging*, 12 (9): 1715–1724. doi:10.1016/j.jcmg.2018.01.011.

Violeau, D. and Issa, R. (2007) Numerical modelling of complex turbulent free-surface flows with the SPH method: an overview. *International Journal for Numerical Methods in Fluids*, 53 (2): 277–304. doi:10.1002/fld.1292.

Vrints, C.J., Claeys, M.J., Bosmans, J., et al. (1999) Effect of stenting on coronary flow velocity reserve: comparison of coil and tubular stents. *Heart*, 82 (4): 465–470. doi:10.1136/hrt.82.4.465.

Walke, W., Paszenda, Z. and Filipiak, J. (2005) Experimental and numerical biomechanical analysis of vascular stent. *Journal of Materials Processing Technology*, 164–165: 1263–1268. doi:10.1016/j.jmatprotec.2005.02.204.

Wall, J.G., Podbielska, H. and Wawrzyńska, M. (eds.) (2018) *Functionalized cardiovascular stents*. Woodhead Publishing series in biomaterials. Duxford, United Kingdom ; Cambridge, MA: Elsevier, Woodhead Publishing.

Wasilewski, J., Mirota, K., Wilczek, K., et al. (2012) Calcific aortic valve damage as a risk factor for cardiovascular events. *Polish Journal of Radiology*, 77 (4): 30–34. doi:10.12659/pjr.883626.

Watkins, J.J., Chen, J., White, H.S., et al. (2003) Zeptomole Voltammetric Detection and Electron-Transfer Rate Measurements Using Platinum Electrodes of Nanometer Dimensions. *Analytical Chemistry*, 75 (16): 3962–3971. doi:10.1021/ac0342931.

Watkins, J.J., Zhang, B. and White, H.S. (2005) Electrochemistry at Nanometer-Scaled Electrodes. *Journal of Chemical Education*, 82 (5): 712. doi:10.1021/ed082p712.

Wei, L., Chen, Q. and Li, Z. (2019a) Influences of plaque eccentricity and composition on the stent–plaque–artery interaction during stent implantation. *Biomechanics and Modeling in Mechanobiology*, 18 (1): 45–56. doi:10.1007/s10237-018-1066-z.

Wei, L., Leo, H.L., Chen, Q., et al. (2019b) Structural and Hemodynamic Analyses of Different Stent Structures in Curved and Stenotic Coronary Artery. *Frontiers in Bioengineering and Biotechnology*, 7: 366. doi:10.3389/fbioe.2019.00366.

Welty, J. (2008) Fundamentals of Momentum, Heat and Mass Transfer, 5th Edition. *book*, p. 729.

Wiesent, L., Schultheiß, U., Schmid, C., et al. (2019) Experimentally validated simulation of coronary stents considering different dogboning ratios and asymmetric stent positioning Avitabile, D. (ed.). *PLOS ONE*, 14 (10): e0224026. doi:10.1371/journal.pone.0224026.

World Health Organisation (WHO). Cardiovascular Diseases (2021). Retrieved at https://www.who.int/news-room/fact-sheets/detail/cardiovascular-diseases-(cvds). Accessed on 06/07/2021.

Xu, J., Yang, J., Huang, N., et al. (2016) Mechanical response of cardiovascular stents under vascular dynamic bending. *BioMedical Engineering OnLine*, 15 (1): 21. doi:10.1186/s12938-016-0135-8.

Yang, X.F., Peng, S.L. and Liu, M.B. (2014) A new kernel function for SPH with applications to free surface flows. *Applied Mathematical Modelling*, 38 (15–16): 3822–3833. doi:10.1016/j.apm.2013.12.001.

Zhao, S., Wu, W., Samant, S., et al. (2021) Patient-specific computational simulation of coronary artery bifurcation stenting. *Scientific Reports*, 11 (1): 16486. doi:10.1038/s41598-021-95026-2.

APPENDIX A: THREE-DIMENSIONAL MODELLING OF MASS TRANSFER AT THE SURFACES STRUCTURED WITH REACTIVE NANOCONES USING MESH-BASED MODELING APPROACH

This is a study on the use of a mesh-based modelling methodology, which functioned as a preliminary step in learning modelling in order to grasp the fundamental idea before switching to a particle-based approach.

A.1 Overview

In this study, the mass transfer on a structured surface composed of a lattice of conical nanoelectrodes is modelled, and a variety of geometrical setups are simulated. The optimal size and distance between cones are sought in terms of dimensionless groups. In the calculations, we look at three different definitions of current density based on three different reference surfaces: the total surface, the surface of the cones, and the local infinitesimal area. Optimization based on different definitions results in different optimal configurations. This implies that, in designing the structured surface, a choice must be made between optimizing the electrode at the nanoscale or at the macroscale based on the actual cost of manufacturing and the return expected by running the electrochemical system.

A.2 Introduction

In the field of electrochemistry, transitioning from the microscale to the nanoscale poses many fascinating possibilities. Nanoelectrodes (electrodes with at least one dimension < 100 nm) enhance mass transport and enable processes to be performed for systems that would require larger electrodes (Watkins et al., 2005) and (Sun et al., 2009). Beside size, the shape of the

nanoelectrode affects the performance too, and conical geometries offer higher mass transport than planar electrodes (Dickinson et al., 2008).

Nanoelectrode fabrication is achieved with different materials and methods, depending on factors including the desired geometry of the nanoelectrode. An excellent summary of these methods was offered by Oja et al. in 2013. Arrays of conical nanoelectrodes, with which this paper is concerned, have been fabricated using block copolymer self-assembly, where a copolymer solution of polystyrene and polymethyl methacrylate in toluene is spin coated onto a gold-plated silicon film (Jeoung et al., 2001). They have also been fabricated using focused ion beam milling of a silicon nitride layer over a buried platinum electrode 2007. The conical nanoelectrode array shown in Figure A-1a was fabricated using plasma etching of nanopillars constituted of MoS_2 and WS_2 nanosheets (Escalera-López et al., 2017).

A number of parameters, such as dimensions of the cone and the spacing between cones are expected to affect the efficiency of the system. On the one hand, higher cone concentration means higher chemical activity; on the other hand, if the cones are too close, current densities decrease due to regions of depleted analyte between the nanoelectrodes (Davies and Compton, 2005).

In this study, the mass transfer on a lattice of conical nanoelectrodes is modelled, and several computer simulations for a variety of cone dimensions and interelectrode spacings are run. On the basis of these calculations, the optimal size and distance between cones is sought in terms of dimensionless groups.

A.3 Modelling

A.3.1 Geometry

The actual system of nanoscale conical electrodes is shown in Figure A-1a. For the computer simulations, we simplify the geometry by assuming a regular lattice distribution of the cones with axial spacing $2S$ as shown in Figure A-1b. With these simplifications, we can take advantages of the symmetries in the geometry and limit the numerical investigation to the computational domain shown in Figure A-1c (grey area) where R is the cone radius, H its height and each cone is surrounded by an area $4S^2 - \pi R^2$ of electrochemical inactive insulation. For a 3D geometry, the computational domain is rectangular with a 1/4 cone inside as shown in Figure A-3a.

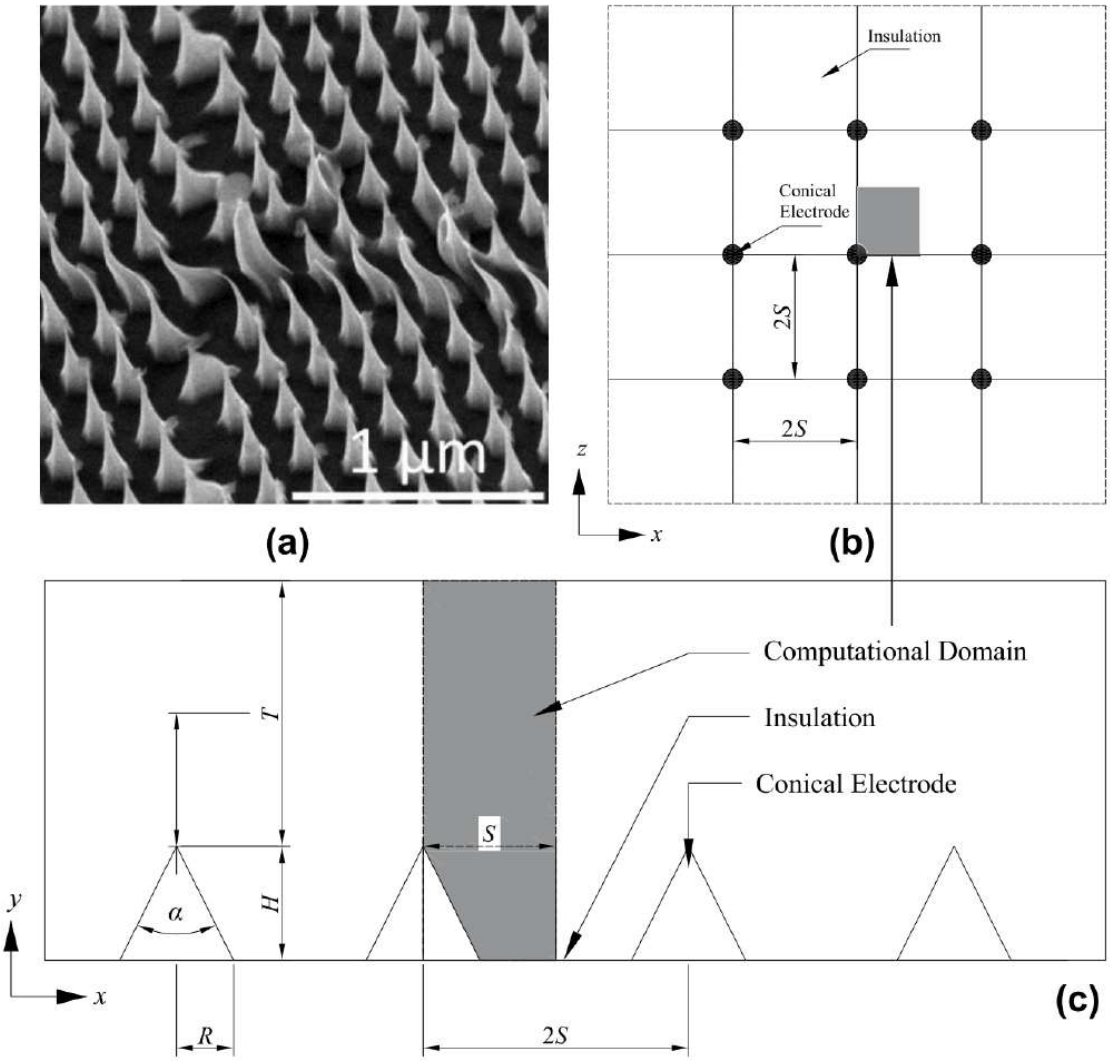

Figure A-1: (a) Image of real nanoscale conical electrodes, (b) simplified cone distribution x-z view (c) Simplified cone distribution x-y view (the actual view for the 3D domain used in the simulation is shown in Fig A-3)

In following, we use the dimensionless spacing and height of the cone defined respectively as

$$S^* = {}^{S}/_{R}, \tag{A1}$$

and

$$H^* = {}^{H}/_{R} \tag{A2}$$

Hence, $S^* = 1$ corresponds to the case of touching conical electrodes. We also use the angle α at the cone apex, which is related to H and R by

$$\alpha = 2\arctan\left(\frac{R}{H}\right) \tag{A3}$$

Using dimensionless groups, we do not need to consider all three geometrical dimensions (i.e. R, H and S) of the system, but only two dimensionless variables (e.g. α and S^*).

A.3.2 Simplifications and modelling equations

For simplicity, only one reacting charged species C is considered and only a semi-cell, which only refers to one electrode, is being considered. We also assume that mass transfer is diffusion limited due to fast kinetics; the validity of this assumption is verified in Section 4.3.5. The fluid is considered stagnant around the electrode (nanocones), as reported Dickinson et. al., 2008 and Tobias et al., 1952, and mass transfer due to migration is neglected due to the excess of supporting electrolyte (Ward, 2012). This condition occurs often in practice (Dickinson et al., 2008) and, additionally, it allows us to neglect other nanoscale phenomena due to the overlap of the diffusion and electrical double layer (Watkins et al., 2003), and edge effects (Thakar et al., 2011).

The fluid is stationary in proximity of the nanocones; far from the nanocones, a stirring bar (Figure 4-2b) ensures that the fluid is well mixed, and the concentration reaches the plateau value C_{bulk}. The concentration decay in the cell is confined in a small layer near the electrode (see

a), where the thickness λ of this layer depends on how the cell is stirred and normally is of the order of 10^{-4}–10^{-3} m (Levich, 1962) for diffusivities and stirring speeds typically occurring in electrochemical applications. In this work, the fluid is considered stagnant around the nanocones and, therefore, the actual length of the concentration layer should be even larger. If the electrode surface were flat, the concentration would decay almost linearly from $x = \lambda$ to $x = 0$ (

b). However, because of the conical structures that increase the contact area, the (average) concentration decreases more than linearly in the layer δ (this is verified in Section 4.4.5) whose thickness is of the order of the cone height (10^{-6} m). Hence, we can distinguish two distinct regions in the concentration layer, δ and λ. In the calculations, we focus only on the region δ in order to reduce significantly the size of the computational domain. Instead of calculating the concentration profiles from the bulk to the electrode surface (Figure 4-2b), we limit our analysis to the region within a distance $T > \delta$ from the electrode surface (Figure 4-2b) and introduce the dimensionless concentration defined as

$$C^* = \frac{C}{C_T} \tag{A4}$$

where C_T is the concentration at T. The actual value of C_T is unknown and, therefore, the profile of C cannot be reconstructed from C^*. However, in eq. A4, C_T acts as a multiplicative constant and, since the aim of this paper is to solve an optimisation problem, the solution is independent of any multiplicative constant. The value of δ, however, is unknown beforehand. Since it is reasonable to assume that δ is of the order of H, the value $T = 2H$ is used in the simulations: in Section 4.3.5, we verify that the non-linear concentration decay is confined in the region $\delta < 2H$.

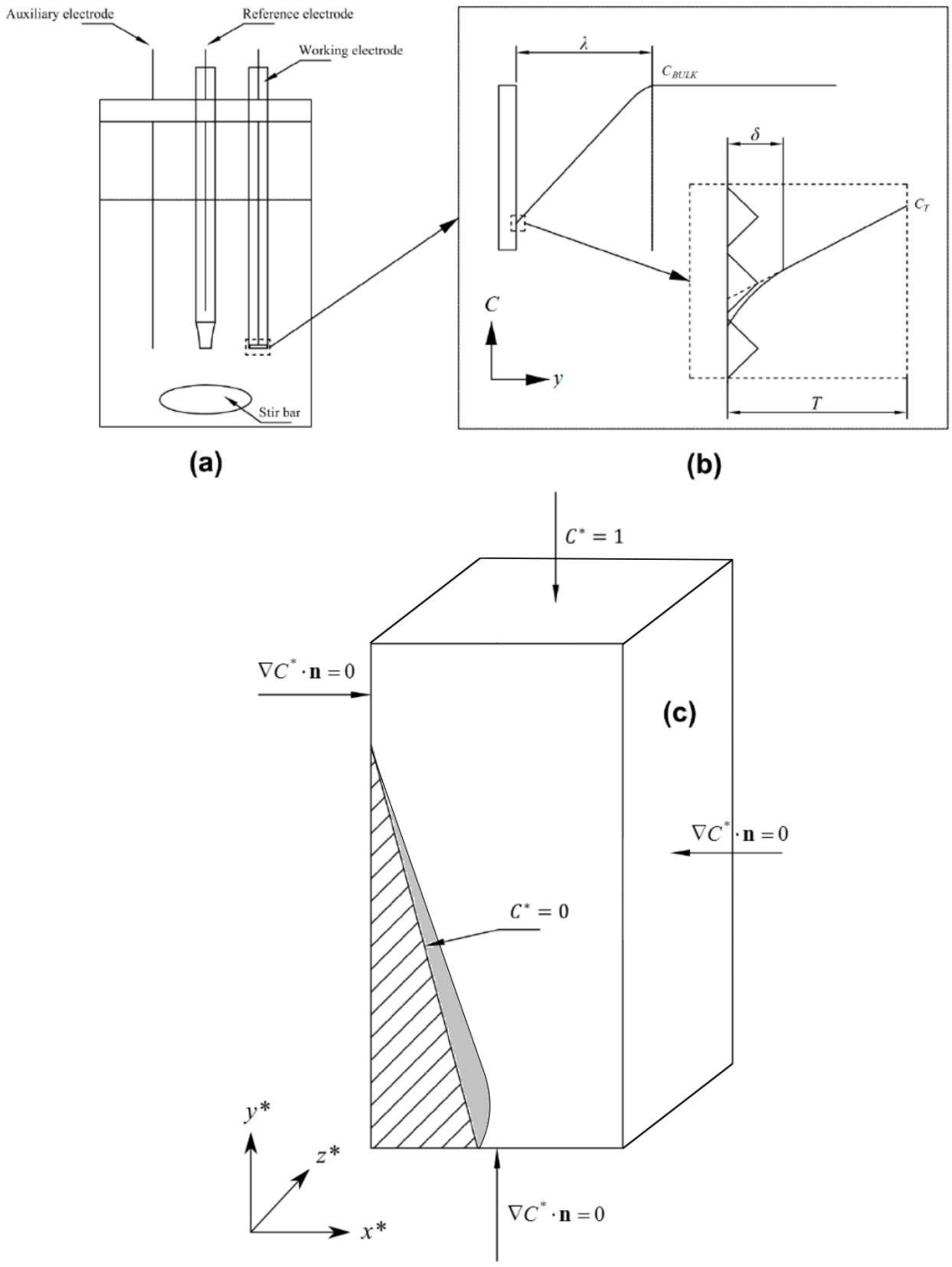

Figure A-2: (a) Electrochemical cell, (b) electrode concentration layer (rotated 90° anticlockwise), (c) boundary conditions.

We also assume *pseudo steady-state* conditions (Welty, 2008). This implies that the layer δ develops significantly faster than the rate at which C_{bulk} changes. The validity of this assumption can be verified by means of an order of magnitude analysis. The goal is to estimate the time required for a concentration difference $C_T - C_W$, where C_W is the wall concentration (here $C_W = 0$), to form in a layer of thickness δ. Considering Fick's law for the transient case in the control volume $0 < x < \delta$ and with concentration $0 < C < C_T$

$$\frac{\partial C}{\partial t} = D\nabla^2 \mathrm{C}, \tag{A5}$$

an order of magnitude analysis brings to

$$\frac{C_T - 0}{\Delta t} \sim D\,\frac{C_T - 0}{\delta^2}, \tag{A6}$$

rearrangement yields

$$\Delta t \sim \frac{\delta^2}{D}, \tag{A7}$$

where D is the diffusivity of C in the liquid. If we introduce in eq. A7 a typical value for electrolyte diffusivity in water (10^{-9} m^2s^{-1}) and $\delta \sim H \sim 10$ nm, we obtain that the characteristic scale Δt required to reach steady-state and form the concentration layer δ is of the order of 10^{-7} s. If we consider a typical voltammetry case, the rate of change of C_{bulk} is of the order of 1s and, therefore, the assumption of pseudo steady-state is sensible.

In general, the Nernst-Planck equation expresses the mass transfer in electrochemical systems. Based on the preceding simplifying assumptions, however, the equation to be solved on the domain of Figure A-1 (grey area) is Laplace's equation in dimensionless form.

$$\nabla^2 C^* = 0 \tag{A8}$$

where the C^* is dimensionless concentration (Eq. A4) and the gradient is calculated with respect to the dimensionless coordinates

$$x^* = \frac{x}{R}, \quad y^* = \frac{y}{R}, \quad z^* = \frac{z}{R} \tag{A9}$$

By taking advantage of the geometric symmetries, the computational domain was reduced to the quarter lattice cell indicated by the grey area in both Figure A-1b and A-1c. The boundary conditions are defined in

c. There is no mass flux through the bottom wall (the insulator), and through the symmetry line ($\nabla C^*.\boldsymbol{n} = 0$). Since the simulations are run for the diffusion limited case, we assume that the chemical reaction is very fast and, on the surface of the reacting cone, C^*=0.

A.4 Numerical solution

The numerical solution is calculated by means of the open-source multiphysics simulation software Elmer based on the finite element method (Lyly et al, 1999). Several geometries (from $\alpha = 5^0$ to 175^0 and from $S^* = 1$ to 10) were generated and meshed with the open-source finite element mesh generator GMSH (Geuzaine and Remacle, 2009). The number of mesh cells depends on the size of the geometry which depends on α and S^* (the smaller the angle the larger the H and hence the larger the volume). Therefore, the geometries, ranging from smallest to the largest, consists of meshes with 14639 nodes and 58367 triangular heptahedral elements and 671315 nodes and 3519343 triangular heptahedral elements respectively. The solved concentration profile was input to the open-source data visualisation software Paraview (Ahrens et al., 2005) to obtain the results. The actual computational domain is represented by Figure A-3a and it consists of ¼ cone of angle α. Figure A-3b however, is the conical boundary section single out from the computational domain.

The conical geometry has two singularities, one at the apex and one at the bottom of the cone. At these points the geometry is not well behaved (Bruce and Giblin, 1992), and hence a sufficiently fine mesh is required to obtain accurate results (Cutress et al., 2010).

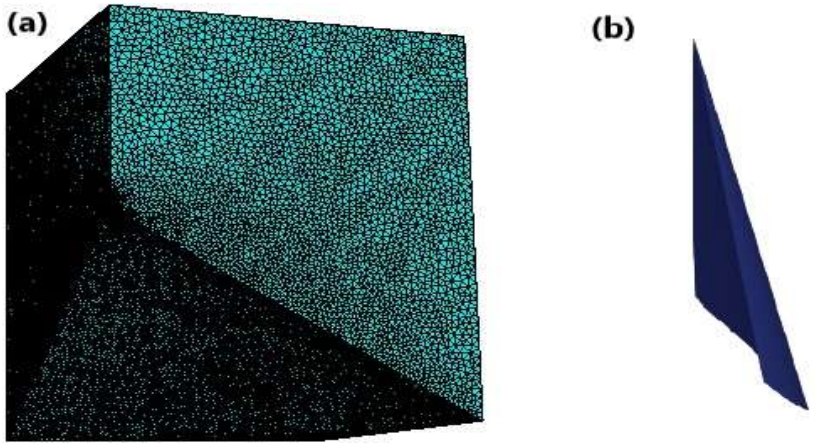

Figure A-3: A 3D view of (a); the computational domain and (b); conical boundary section

In line with the above, a further specification required for accurate results was the fineness of the mesh at the conical face. Therefore, meshes of different characteristic size were tested. This was done by reducing the mesh size by half (making it finer) until the overall difference in the concentration profiles of the successive mesh size are below 1%. Grid independence was then achieved with a mesh of dimensionless characteristic size $q^* = q/\mathrm{r}$ (where q is the actual size of the mesh) = 8×10^{-2} on the bulk region and mesh size $q^* = 2\times10^{-2}$ on the conical surface, and this is used for all the geometries in the simulation. In all cases considered, Eq. A8 was solved with a convergence tolerance of 1×10^{-10}.

A.5. Results

A.5.1 Concentration Profiles and total current

Examples of concentration profiles for the cases $\alpha = 5°$ with $S^* = 1$, $\alpha = 5^\circ$ with $S^* = 10$, $\alpha = 135°$ with $S^* = 1$, and $\alpha = 135°$ with $S^* = 10$ are shown in Figure A-4. Each profile in the Figure shows the concentration distribution.

If only a narrow spacing between two adjacent cones is available (e.g. α is small and $S^*=1$), the reactant cannot reach the lower section of the cone and it is rapidly consumed as in the case of Figure A-4a. In the lower part of the domain, therefore, a C^* depleted region forms.

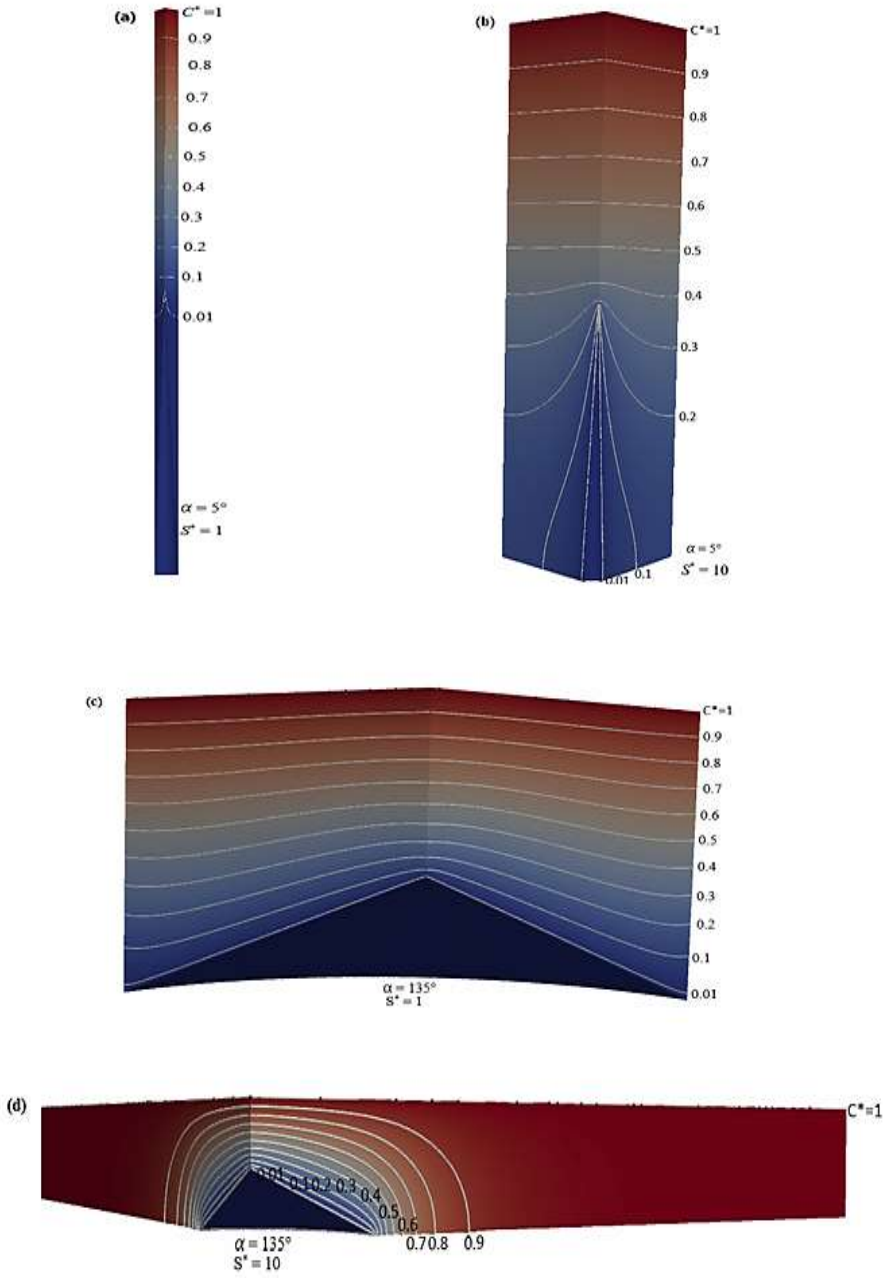

Figure A-4: Concentration isoprofiles for (a) α = 5°, S^* = 1; (b) α = 5°, S^* = 10; (c) α = 135°, S^* = 1 and (d) α = 135°, S^* = 10

When the values of α and S^* increase, however, it is easier for the reactant to reach the non-reactive bottom wall resulting in a smaller depleted region. The isoconcentration surface at $C^* = 0.01$ in Figure A-4 illustrates how the depleted region changes with α and S^*. In Fig.

A-4b, C^*=0.001 almost coincides with the cone surface, which implies a very small, depleted region at higher values of α and S^*. The variation in the concentration profile with α can be appreciated by comparing Fig A-4a with Fig A-4c: the larger the angle the more reactive the cone surface is and, hence, more cone current density is generated. The effect of increasing S^* is noticeable when comparing Fig A-4a with A-4b, which are of the same angle but different value of S^*. The concentration profile is more uniformly distributed when α increases (Fig A-4a with A-4c) than when S^* increases (Fig A-4a with A-4b). Therefore, the cone (electrode) surfaces become more active by increasing the angle rather than the inter electrode spacing.

From the concentration profiles, we can compute the total current I for each cone as

$$I = FnD \int_{A_{cone}} (\nabla C)_\Gamma \cdot d\boldsymbol{A} \tag{A10}$$

where F is the Faraday constant, n the ionic charge of the reacting species, A_{cone} the total area of the cone, $d\mathbf{A}$ the surface vector perpendicular to the cone surface, and $(\nabla C)_\Gamma$ the concentration gradient calculated at the cone surface. By introducing dimensionless variables (eq. A4 and A9), we obtain

$$I = FnDRC_T \int_{A^*_{cone}} (\nabla C^*)_\Gamma \cdot d\boldsymbol{A}^* \tag{A11}$$

We can, therefore, define the dimensionless current as

$$I^* = \frac{I}{FDnC_TR} = \int_{A^*_{cone}} (\nabla C^*)_\Gamma \cdot d\boldsymbol{A}^*. \tag{A12}$$

As we discussed from C and C^*, we cannot determine I form I^* since C_T is unknown. However, C_T only appears as a multiplicative constant in eq. A12 and, therefore, it does not affect any optimization problem based on eq. A12. Similarly, D and n change from ion to ion, but they only appear as multiplicative constants in eq. A12. The results discussed in the next sections, therefore, are valid for any type of ion and diffusivity.

As already mentioned, the aim of this paper is to study how the current changes with the distance between cones (S^*) and the angle at the apex (α) and determine the optimal S^* and α that maximize the current density. In the case under investigation, we can define the current density in three different ways according to the reference area considered. Each definition refers to a different scale of observation and provides understanding of the system's behaviour from a different point of view.

The three (dimensionless) current densities discussed in the next sections are: the local current density j^* (Section 4.5.2), the cone current density $J_C{}^*$(Section 4.5.3), and the electrode current density $J_E{}^*$(Section 4.5.4).

A.5.2 Local current density j*

The local current density j^* is the current generated by each infinitesimal area dA^* of the cone

$$j^* = \frac{dI^*}{dA^*} = (\nabla C^*)_\Gamma \cdot \mathbf{n}, \tag{A13}$$

where **n** is a unit vector perpendicular to dA^*. Various profiles of $j^*$are plotted in Figure 4.5 for different values of α and S^*. The abscissa is the dimensionless distance from the apex defined as

$$\zeta^* = \frac{\zeta}{Z} \tag{A14}$$

where ζ is the distance from the apex to the location where the current density is measured, and Z the total slant distance from the apex to the bottom of the cone. Figure A-5 and Figure

A-4 refer to the same cases and are used together for understanding the dynamics of the system.

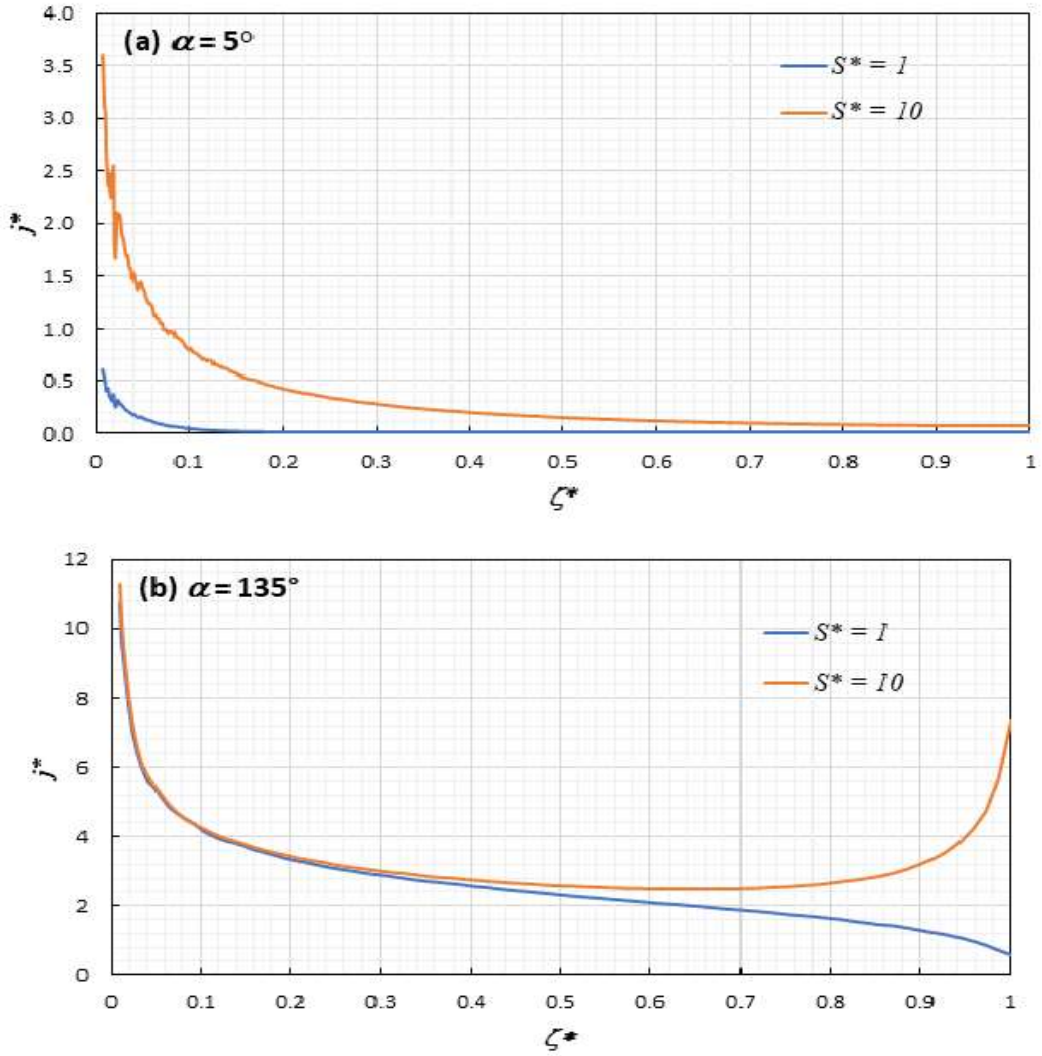

Figure A-5: Local current densities along conical face for α = 5° (a) and 135° (b), S^* = 1 and S^* = 10

For α = 5° (Figure A-5a) and S^* = 1, the current is high at the apex and quickly decays to zero after ζ^* = 0.12 leaving the remainder of the conical surface inactive. This inactive surface corresponds to the depleted zone shown in Figure A-4a. For S^* = 10 however, with the same α = 5°, the profile is similar, but a larger portion of the conical surface generates current.

A different situation occurs when α = 135° (Figure A-5b), which corresponds to a very flat cone. Even when two cones are in close contact (S^*=1), there is enough space between two adjacent cones for efficient mass transfer (see also Figure A-4c and A-4d). Consequently, near the apex, the j^* profiles in Figure A-5b are similar. However, as ζ^* approaches 1 (towards the bottom of the cone) the S^* = 10 graph shows an increase in j^*, whereas the S^* = 1 graph a decrease. This result can be explained by comparing Figure A-4c and A-4d. For S^*=1, the bottom of the cone is where one cone touches the adjacent one; two cones, therefore consume C^* in that region. For S^*=10, however, around the cone there is a large unreactive area, where C^* is higher and can effectively diffuse on the reactive conical surface thereby resulting to an increase in j^*.

The advantage of looking at the local current density j^* lies in the fact that, in this way, we can distinguish which fraction of the cone is active and which is inactive. Especially for small α (Figure A-5a), where the current density decays sharply, we can divide the electrode's surface in two regions (Figure A-6): an *active zone*, where most of the current is produced, and a *depleted zone*, where mass transfer is not effective enough to replenish the consumed C^* and electrochemical activity is low. From Figure A-5a and A-5b, it is clear that the active zone increases with increasing α.

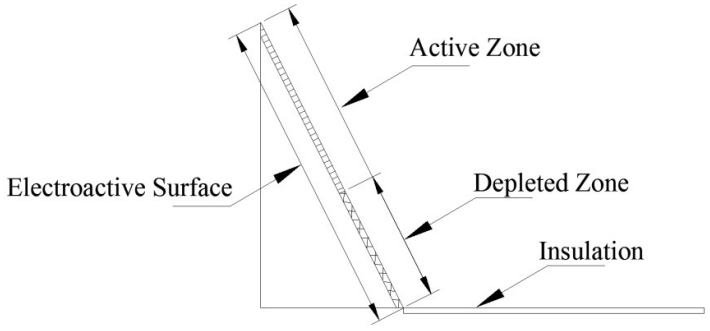

Figure A-6: Schematic of different zones on electrode geometry

We can arbitrarily define the depleted zone as the part of the cone where j^* is below 1% of its maximal value and, the active zone as the other part. Based on this, we can define the cone efficiency as

$$\eta = \frac{\zeta_A}{Z} \tag{A15}$$

where ζ_A is the length of active zone and Z the total slant height of the cone. Figure A-7 shows how η varies with α and S^*.

Maximal efficiency (η =1 i.e. j^* never goes below 1% of its maximal value) is achieved for any value of S^* when $\alpha \geq 90°$ as it can also be seen in Figure A-7.

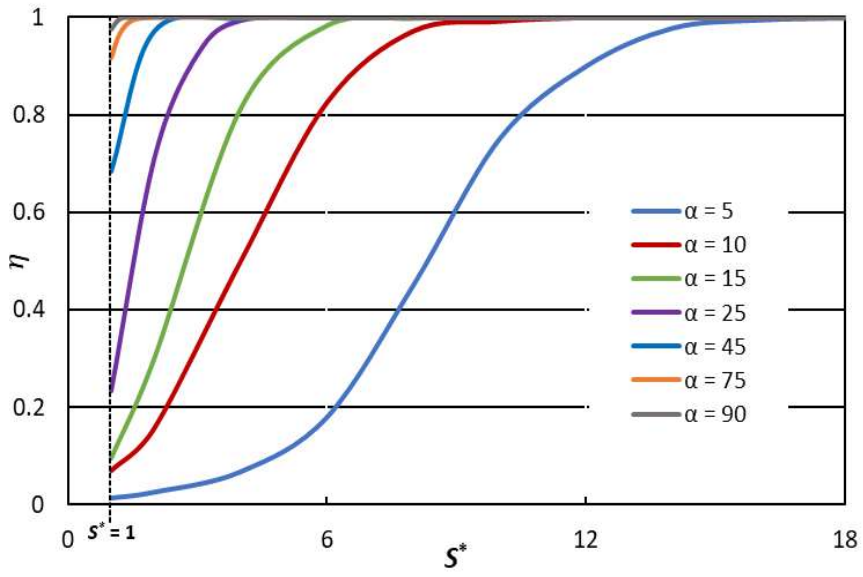

Figure A-7: Conical efficiencies for different geometries

The value of $\alpha = 90°$, therefore, represents a demarcation value: below 90°, significantly depleted zones could appear at the bottom of the cone; above 90°, the concentration may decrease along the cone, but completely depleted zones never occur. Moreover, as also Figure A-5b shows, at high angles, the concentration at the bottom of the cone may even increase due to the fact that the insulation wall is not reactive.

From the point of view of j^*, it is desirable to operate under conditions that guarantee $\eta = 1$, since these conditions avoid depleted zones and the exploit the whole surface of the electrode.

A.5.3 Cone current density JC*

The cone current density J_C^* is the total current generated by each cone divided by the area of the cone

$$J_C^* = \frac{\int_{A_{cone}^*} (\nabla C^*)_\Gamma \cdot d\boldsymbol{A}^*}{A_{cone}^*} \tag{A16}$$

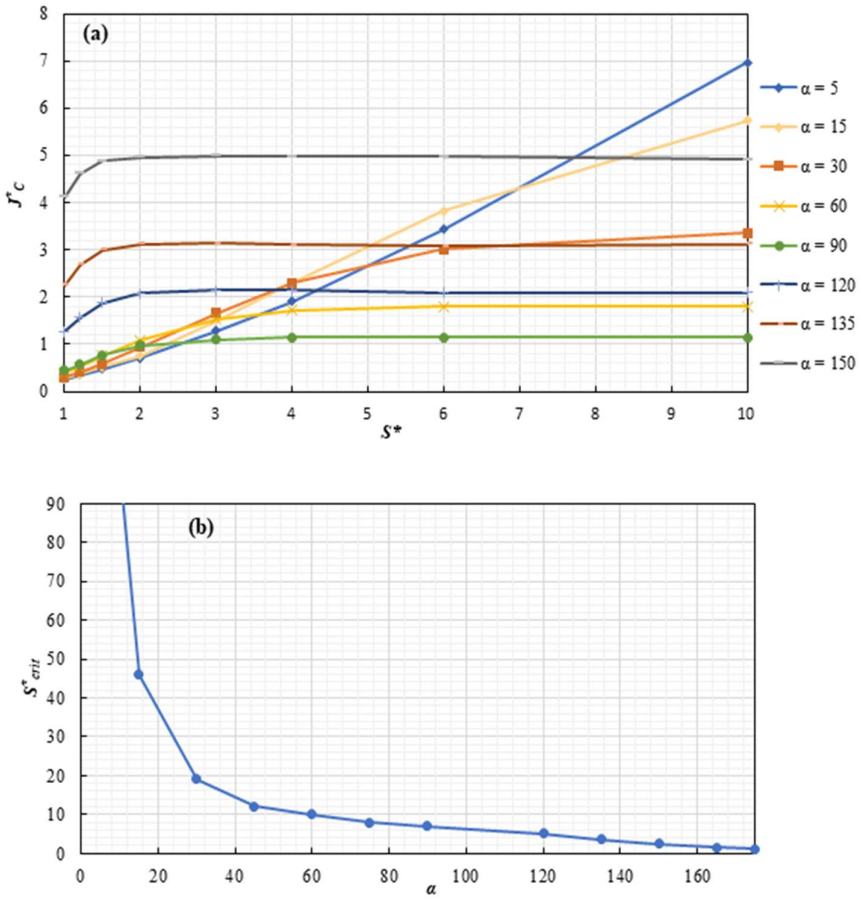

Figure A-8: Plots of J^*_C (a) and S^*_{crit} (b)

Figure A-8a shows the plot of J_C^* vs S^* for different values of α. As S^* increases, the space between two cones increases; this facilitates the replenishment of C^* and J_C^* increases. In the

case of $S^* = 1$ up to $\alpha = 150°$, the cone is very flat, and the solution is similar to the analytical solution for a flat disk. The flat disk solution was calculated by (Dickinson et al., 2008) and corresponds to $J^*_C = 4$[1]. Above a certain S^*, however, the distance between the cones is large enough to allow the maximal transfer of C^*. At some point, J_C^* reaches a plateau and moving the cones further apart does not improve the current density. The value of S^*, at which J_C^* reaches a plateau, is denoted as S^*_{crit}, and is plotted in Figure A-8b. Figure A-8a also shows that the value at the plateau (i.e. $S^* = S^*_{crit}$) is very high for sharps cones (i.e. $\alpha < 15°$), gradually decreases until $\alpha = 90°$, and increases again for $\alpha > 90°$ This shows, as also highlighted in Section 4.3.2, that sharp cones are potentially very reactive; however, they are also more subjected to the presence of depleted zones and J^*_C dramatically decrease at low values of S^*. Flat cones (i.e. $\alpha > 90°$), on the contrary, are generally less active, but also less prone to depletion; therefore, their current density does not change significantly between high and low values of S^*. Intermediate cones (i.e. $15° < \alpha < 90°$) show a behaviour in between sharp and flat cones.

From the point of view of J_C^*, it is desirable to operate at $S^* = S^*_{crit}$ because it is the best compromise between high reaction rate and compact electrodes (i.e. small S^*).

A.5.4 Electrode current density JE*

The final current density we introduce is J_E^*, which is defined as the current density with respect to the projected area occupied by an electrode and its surrounding insulation.

$$J_E^* = \frac{\int_{A^*_{cone}} (\nabla C^*)_\Gamma \cdot d\boldsymbol{A}^*}{S^{*2}} \tag{A17}$$

[1] *In Dickinson et al. (2008) the solution was given as $2/\pi$, but they use an additional 2π factor at the denominator of their dimensionless current; therefore, their $2/\pi$ value corresponds to $J^*_C = 4$ in this study*

J_C^* differ from J_E^* by the surface used at the denominator of eq. A16 and equation A17. J_C^* considers only the electroactive conical surface A_{cone}, while J_E^* considers the (macroscopic) apparent electrode surface S^2, which also includes the electrochemically inactive insulator.

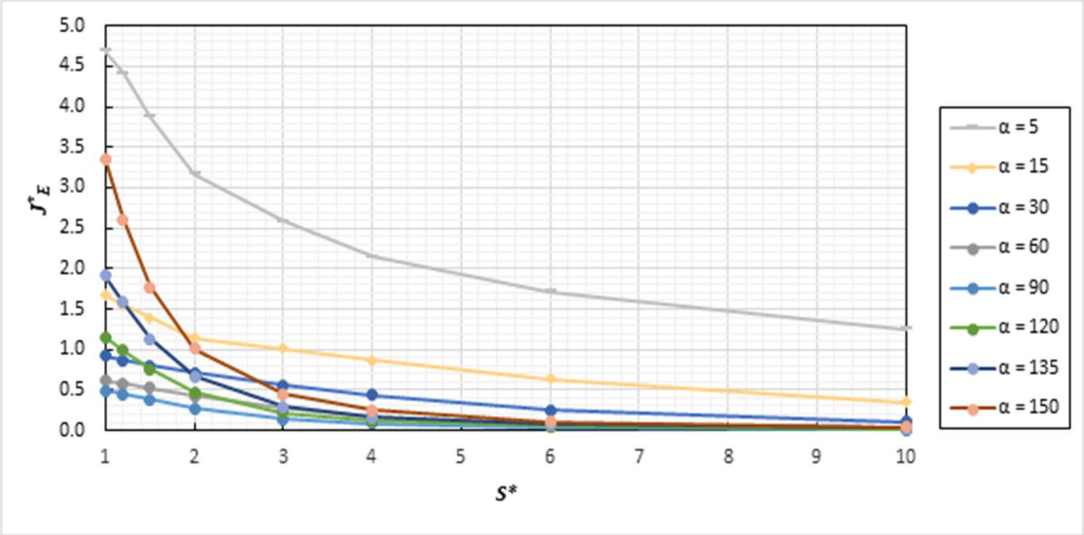

Figure A-9**:** Plots of J_E^* *vs.* S^* for selected values of α

Figure A-9 shows the plot of J_E^* vs. S^* for selected values of α. In general, J_E^* attains its maximum values at S^*=1 and decays as S^* increases. Also, this case shows a difference of behaviour among sharp, intermediate and flat cones as discussed in previous Sections.

From the point of view of J_E^*, it is desirable to operate, in all cases, with touching conical electrodes (S^* = 1).

In this section, we have identified three types of current densities. Each definition brings to different "optimal" values of S^* for a given type of cone (i.e. sharp, intermediate, flat). The practical differences and consequences of these three sets of optimal conditions are discussed in the conclusions.

A.5.5 Validity of the simplifying hypothesis

In Section 4.2, we discussed three simplifying hypotheses used in the model:(i) pseudo steady state, (ii) linear decay from C_T to δ, and (iii) diffusion limited conversion (fast chemical reaction). The first hypothesis was discussed in Section 4.2.2; here we verify that the last two are correct.

In the case of linear decay from C_T to δ, we verified that, in all the simulations, above a distance δ from the apex the concentration profile is almost linear. We also checked that, by using $T = 2H$, our computational domain is always larger than δ. An example can be seen in Figure A-10 that shows the concentration profile C^* versus $T - H$ (the height above the apex) for R = 50nm, H = 121nm (α = 45°) and T = 100 nm. The calculated value of δ is 12 nm, which, incidentally, also supports the order of magnitude analysis in eq. A5 to A7 used to justify the pseudo-state hypothesis.

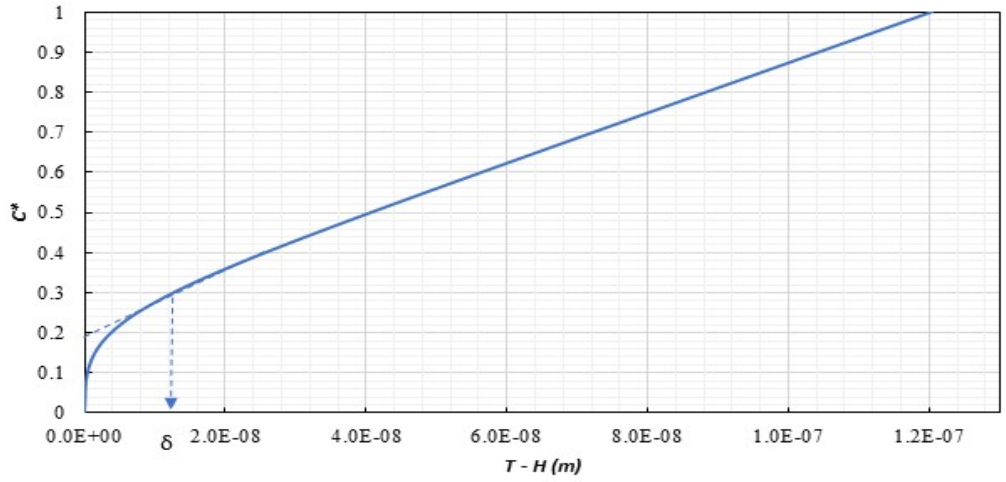

Figure A-10: Steady-state concentration profile above apex of nanoscale system (R = 50nm, H = 121nm, α = 45°, T = 2H, S^* = 1)

To verify the diffusion limited hypothesis, we ran several simulations with different boundary conditions at the conical wall. If the reaction is very fast, the concentration at the wall is negligible and Dirichlet boundary condition (C^*=0) can be used (Figure A-2c). If the reaction is not as fast, the boundary conditions must change accordingly. To determine the new boundary conditions, we start from the Butler-Volmer equation

$$i = i_0 \left\{ \exp\left[\frac{\beta_a nF}{\mathcal{RT}}(E - E_{eq})\right] - \exp\left[-\frac{\beta_c nF}{\mathcal{RT}}(E - E_{eq})\right]\right\} \tag{A18}$$

where i is electrode current density, i_0 the exchange current density, E and E_{eq} are the applied and equilibrium potentials respectively, β_a and β_c are, respectively the anodic and cathodic transfer coefficients, $\mathcal{R}$ is the ideal gas constant and $\mathcal{T}$ is the Kelvin temperature (Newman and Thomas-Alyea, 2004). Given a specific electrode and a constant set of working conditions, the Butler-Volmer equation can be simplified to Tafel equation (eq. A19) (Newman and Thomas-Alyea, 2004; Bard and Faulkner, 2001) which is a first order chemical reaction and further simplifies to eq. 20.[2]

$$i = nFk_0 C exp\left(\pm\beta_{a/c} F \frac{E - E_{eq}}{\mathcal{RT}}\right) \tag{A19}$$

$$i = FnkC \tag{A20}$$

where,

$$k = k_0 exp\left(\pm\beta_{a/c} F \frac{E - E_{eq}}{\mathcal{RT}}\right) \tag{A21}$$

[2] *Eq. (18) can be simplified in the two limiting cases of low ($E \sim E_{eq}$) and high overpotentials ($E >> E_{eq}$ for anodic reactions and $E << E_{eq}$ for cathodic reactions). Practical applications require high reaction rates and therefore $|E| >> |E_{eq}|$. In this case, the Butler-Volmer equation at a specific electrode simplifies to the Tafel equation, $i = nFk_0 C exp\left(\pm\beta_{a/c} F \frac{E - E_{eq}}{\mathcal{RT}}\right)$, where the sign depends on the type of reaction (anodic or cathodic) and k_0 is the rate constant for the electrode reaction. Given a specific electrode and chemical reaction (i.e. k_0, n, E_{eq} and $\beta_{a/c}$ are constant) and a set of constant working conditions (i.e. $\mathcal{T}$ and E are constant), eq. (19) further simplifies to eq. (20) where the exponential term (constant) is lumped into the constant k.*

where the reaction constant k [m s^{-1}] depends on the cell overpotential. The diffusive flux at the electrode surface (current) is equal to the rate of reaction at the electrode surface (Feldberg, 2010).

$$i = FnkC = FnD\nabla C \cdot \mathbf{n} \tag{A22}$$

where n is the number of electrons and **n** the unit vector perpendicular to the electrode surface. This provides a set of Robin boundary condition at the conical wall

$$kC - D\nabla C \cdot \mathbf{n} = 0 \tag{A23}$$

or, in dimensional form,

$$\nabla C^* \cdot \mathbf{n} - Da\, C^* = 0, \tag{A24}$$

where Da is the Damköhler number

$$Da = \frac{kR}{D}. \tag{A25}$$

The Damköhler number, which is a dimensionless number, gives a quick estimate of the degree of conversion achieved in a given reaction (Fogler, 2006). The effect of Da on the plateau-value of J_C^* is shown in Figure A-11 for α = 150° and S^*=1.

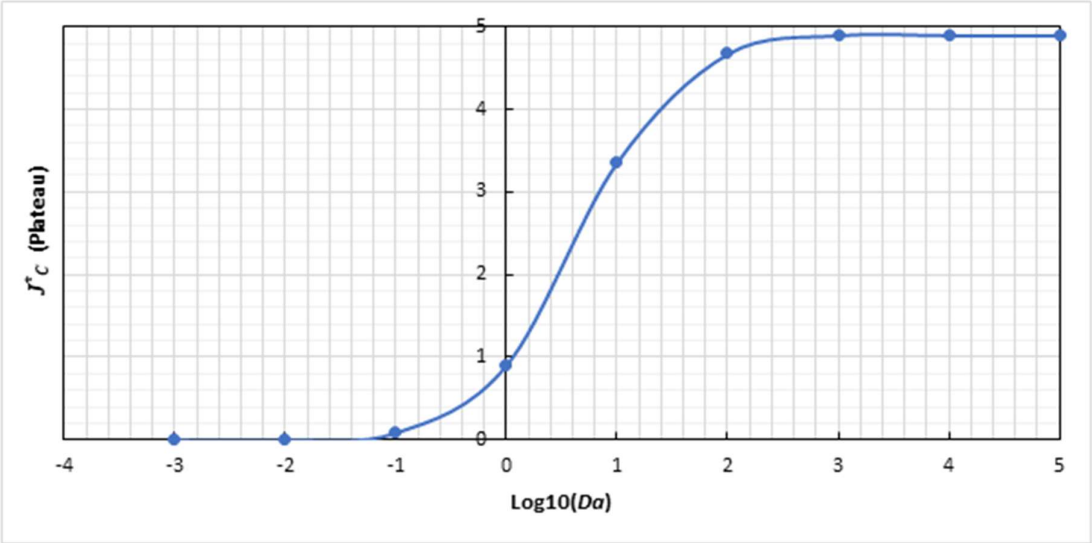

Figure A-11: Effect of Da on J_C^* at the plateau (S* = 1, α = 150°)

Below $Da = 0.1$, the chemical reaction is slow, and no effective conversion is observed. Between $Da = 0.1$ and $Da = 100$, the value of $J_C{}^*$ gradually increases until $Da > 100$ where it reaches a constant value. This implies that the diffusion limited conditions (i.e. $Da \rightarrow \infty$) are valid for $Da > 100$.

A.6 Conclusion

We modelled the mass transfer on a lattice of conical nanoelectrodes and run a number of simulations for a variety of cone dimensions and interelectrode spacings. The analysis is carried out using dimensionless groups to reduce the number of geometrical variables from three (R, H and S) to two (α and S^*).We look at three different definitions of dimensionless current density: one is based on the total surface including the insulator (J_E^*), the other on the conical electroactive surface (J_C^*), and the third on the local infinitesimal area (j^*).

Optimization based on different current densities results in different optimal α and S^*.

If we optimize with respect to J_E^*, we look at the structured surface from the macroscopic point of view. This is the traditional approach, which focuses on the current generated by the overall surface. In this case, since the highest electrochemical activity occurs at the apex, for flat nanocones ($\alpha > 90°$) and highly concentrated (low S^*) nancones are preferable. This solution does not waste a lot of electroactive material and the nanocones are widely utilised due to large electroactive regions between adjacent cones.

If we optimize with respect of J_C^*, we look at the cones from the microscopic point of view. For $S^* \to \infty$, small angles are preferable, but with a given α, $S^* = 1$ is not the best choice. The optimal spacing varies with α and $S^* = S_{crit}^*$ is the best compromise between high reaction rate and compact electrodes.

The local current density (j^*) explains this behaviour. The conical surface can be divided two zones: the active zone and the depleted zone. Sharp cones increase local current density, but, at the same time, reduce the area of the active zone. Larger spacing reduces the local current density (because the insulation surface increases), but, at the same time, increase the area of the active zone. At a critical distance S_{crit}^*, these two opposite effects balance each other and an optimal spacing, for that particular angle, is achieved.

These considerations bring to the conclusion that there is no best solution and the choice is between optimizing the macroscopic surface or the nanostructures of the electrode. By maximising J_C^*, one obtains the most efficient use of the material, whereas by maximising J_E^* one best utilises the electroactive surface. The final setup will depend on the actual cost of manufacturing the nanostructures compared to the return expected by running the electrochemical system. High manufacturing costs will favour microscopic optimization, whereas high returns will favour macroscopic optimization.

A.7 Nomenclature and Notations

A	Conical surface area [m^2]
C	Concentration of the charged species [mol m^{-3}]
C_{bulk}	Bulk concentration [mol m^{-3}]
C_T	Concentration at $x=T$ [mol m^{-3}]
D	Diffusion coefficient [m^2 s^{-1}]
Da	Damköhler number [-]
E	Potential [V]
F	Faraday's Constant [C mol^{-1}]
H	Apex height of conical electrode [m]
i	Current [A]
i_0	Current exchange density [A m^{-2}]
J	Current density based on electroactive conical surface area [A m^{-2}]
k	First order reaction constant [m s^{-1}]
k_0	Rate constant for the electrode reaction [m s^{-1}]
K	Overall mass transfer coefficient [m s^{-1}]
n	Number of electrons [-]
n	Unit vector perpendicular to the electrode surface

q Characteristic length [m]

R Basal radius of conical electrode [m]

R^* Dimensionless form of [-]

S Inter electrode spacing [m]

S^* Dimensionless form of S [-]

T Height above apex of conical electrode [m]

$\mathcal{T}$ Temperature [K]

Z Total slant height of the cone from the apex [m]

α Contact angle [deg]

ρ Number of cones per unit area [m^{-2}]

β Transfer coefficient [-]

δ, λ Concentration layer thickness [m]

ζ distance from the apex to the location where the current density is measured [m]

ζ^* Dimensionless form of ζ [dimensionless]

APPENDIX B: TRANSITION FROM MESH-BASED TO PARTICLE-BASED MODELLING APPROACH

The transition from a mesh-based to a particle-based modelling approach is demonstrated in this report. We therefore chose simple geometry (rectangular bar) to show how a linear elasticity problem is handled using both mesh-based and particle-based techniques. The two methodologies' foundations are described, and comparisons are made based on the outcomes. Therefore, we move from the mesh technique to the particle method through this knowledge transition, which subsequently lead us to DMP framework which is a combination of particle methods.

B.1 Abstract

In the previous chapter we applied the mesh-based modelling technique to solve a mass transfer problem, and in this chapter therefore, the application of particle method is introduced and the two approaches (mesh and particle) were used to solve a linear elasticity problem with a simple rectangular geometry. A Finite Element Software 'Elmer' was used for the mesh-based while a Lattice Spring Model was used as the particle method. In the mesh-based approach a Poisson's ratios of 0.37 was used. Whereas the particle method implicitly uses the a Poisson's ratio of 0.25 since, according to Kot et al., (2015), the Poisson's ratio for a lattice spring is always 0.25. A numerical comparison of the results was made, and it was found that the two method gives very similar results despite haven different Poisson's ratios. In fact, the resulting stresses are only partially dependent on the Poisson's ratio. When, in the mesh-based method, the Poisson ratio is changed to $\nu = 0.25$, the values for the maximum stress are only slightly lower than those for $\nu = 0.37$.

B.2 Introduction

It was mentioned that the advent of simulation has reduced, drastically, the risk and cost by avoiding the danger and loss of life during testing. It is also true that with computer simulations many conditions can be varied and outcomes investigated without risk (Armengaud et al., 2009) and certain behaviours can be studied easily or closely by either speeding up or slowing down the simulation.

As already mentioned in Chapter 1, the modelling and simulation of a particular problem can be done either by the traditional mesh-based method or meshfree particle method (MPM). The mesh-based method considered the whole geometry as a continuum entity. The geometry is then created and the surfaces and volume gridded with either structured or unstructured mesh using a mesh generator software such as GridPro, Gmsh, Gambit etc (Geuzaine and Remacle, 2009). With the particle method the geometry is made-up of particles arranged in an orderly manner to form the geometry.

The detail theory was already written in chapter 2 for mesh-based and chapter 3 for particle-based approach respectively.

B.3 Methodology

The two approaches were used to quantify the maximum von Mises stress on a wooden rectangular bar made of pine wood. The bar geometry was created and meshed using Gmsh (with a structured mesh) and then exported to Elmer for calculations. Linear Elasticity equation in Elmer was applied and the boundary conditions defined. After the computation, the Elmer vtu file (result file) is uploaded to Paraview for post-processing.

For the particle-based simulations, LAMMPS script file was written, using MATLAB codes, for the same structure, and this time, the number of nodes obtained from the structured mesh were represented by particles. The principle of LSM was employed where the particles are connected to each other by a means of a spring (Kot et al., 2015; Alexiadis, 2015a), with the equation relating the applied force with the distance the particle moves (eq. 2.11)

$$F = k(r - r_0). \tag{B1}$$

where F is the applied force, r_0 is the initial distance between two particles, r is the instantaneous distance, and k the spring constant. The k is related to the material's Young modulus (Sanfilippo et al., 2021) as in equation (212). See details of these equations (eq. 2.11 to 2.14) in Chapter 2.

$$k = \frac{El_0}{2.5}. \tag{B2}$$

The simulation was run in LAMMPS, and the dumb file (result file) is visualized with Ovito software (a visualization software) for post-processing. In the postprocessing, properties such as von Mises stress and the material displacement (bending due to load) were calculated.

B.4 Geometry and the model

The geometry is that of a rectangular wood bar of dimension $x = 0.1$ m, $y = 0.05$ m and $z = 1.0$ m. Both approaches (mesh and particle-based) were used to build the geometry of that dimension with one represented by mesh and the other, by particles. A mesh generating software Gmsh was used to create the geometry and the structured mesh (grid). The surface of the geometry was grided with an equal size box (squares) of dimension 0.0125m.

For the particle geometry, however, the particles and bonds between them were created using MATLAB code with each node of the square represented by a spherical particle and the

distance between the particle (bond length) is 0.0125m (which is the same size as that obtained from mesh).

The computation was done by a FEM software Elmer where the in-built linear elasticity model was used. The model was set up with the preconditions that specified the maximum number of iteration equal 500, the steady state simulation type, and a BDF boundary condition. The equation was specified, and the material was chosen as a pine wood from the material library with a density of 550kgm^{-3}. The Young modulus of 10 x10^{19} Nm^{-2} and the Poisson's ratio of 0.37 were used. The boundary condition state that the force of 200N was applied at one end and the other end was held constant.

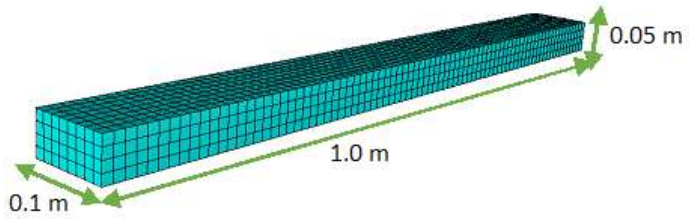

Figure B-1: Wooden bar geometry with structured mesh

In the particle method the geometry consists of 3645 number of particles and 27,100 number of bonds. The mass of particle is gotten from the specified density and the volume of the material. The same was applied for the force used and this gives the per atom mass and per atom force and the simulation boundary was set to be periodic at *x,y* and *z* directions. Table B-1 present some of the parameters used during the simulation.

Table B-0.1: Parameters used in the simulation

Elmer	
Length z	1.0 m
With x	1.0×10^{-1} m
Thickness y	5.0×10^{-2} m
Applied force	2,000 N
Acceleration g	9.88 m s^{-2}
Density of the bar ρ	550 kg m^{-3}
Yong modulus	1.0×10^{-10} N m^{-2}
Poison ratio	0.37 [-]
Boundary Condition	BDF
LSM	
Number particles	3,645
Number of bonds	27,100
Mass of each particle	7.55×10^{-4} kg
Particle spacing l	1.25×10^{-2} m
Bar thickness d	5.0×10^{-2} m
Elastic constant k	1000 kg s^{-2}
Time step Δt	1×10^{-6} s

In the LSM, the Poisso'n ratio is always 0.25 (Kot et al., 2015) and this cannot be changed when using the LSM particle method. Therefore, we tried to adjust the Poison ratio in the mesh-based method from the given 0.37 to 0.25 (similar to that of the particle method) to compare the results.

B.5 Results and Discussion

B.5.1 Stress distribution

The von Mises stress is computed, and the distribution is presented by colour coding the structure using ParaView (for mesh-based method) and Ovito (for the particle method). With a Poisson's ratio of 0.37 and 0.25 for Elmer and LSM respectively, the results obtained for the maximum stress and the maximum displacement were very similar. The area of maximum stress can be seen as the most reddish colour while the lowest stress is the most blueish as shown in Figure B-2 (see the colour guide in the Figure). The maximum stress in (A) is 5.2 x 10^7 N m^{-2} while it is 5.24 x 10^7 N m^{-2} in (B).

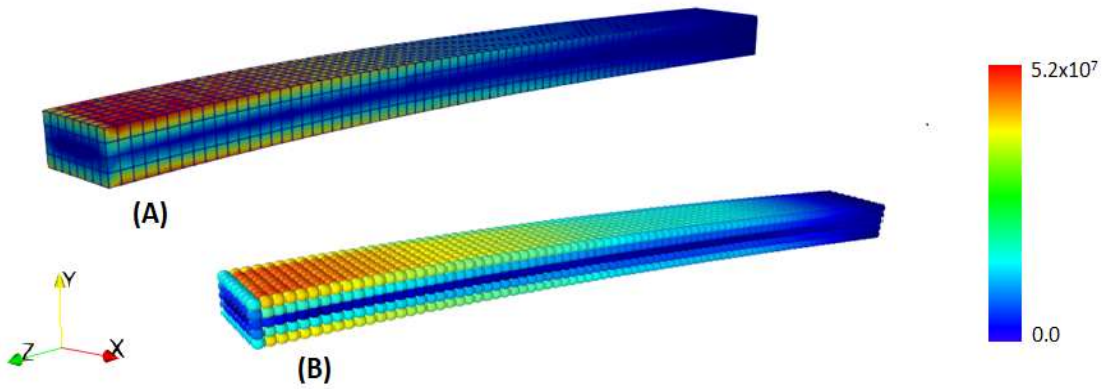

Figure B-2: The von Mises stress from (A) the ParaView (mesh-based) and (B) Ovito (particle-based).

When a Poisson's ratio of 0.25 was used in the Elmer, the result shows a small decrease in value for displacement as well as the stress. The maximum von Mises stress became 5.0 x 10^7 N m^{-2}. This is expected because the maximum stress increase with increasing the Poisson's ratio (Abd-Elhady and Sallam, 2016) and vice vasa.

When we compare the mesh-based method with Poisson's ratio 0.37, which correspond to the given Young modulus, and the particle method (with Poisson's ratio always 0.25) it is interesting to note that, despite the difference in the Poisson's ratio between the two methods, the values obtained are very close. This shows that differences in Poisson ratios result in relatively modest differences in stresses. This fact will be useful in the next chapters when the LSM is used to model solid structures. In fact, even if, by using the LSM, we are limited to $\nu = 0.25$, which can be different from the actual Poisson ration of the material under investigation, we expect only small differences due to this limitation.

B.5.2 Displacement

Similar to what was said in section 7.4.1, the displacement was also presented in term of colour coding. The two approaches give almost same result with mesh-base method having 6.13×10^{-2} m maximum displacement and the particle method having 6.10×10^{-2} m maximum displacement (Figure B-3a and b). As mentioned in the section above, these values were obtained when a Poisson's ratios of 0.37 and 0.25 were used and yet the differences noticed is minimal.

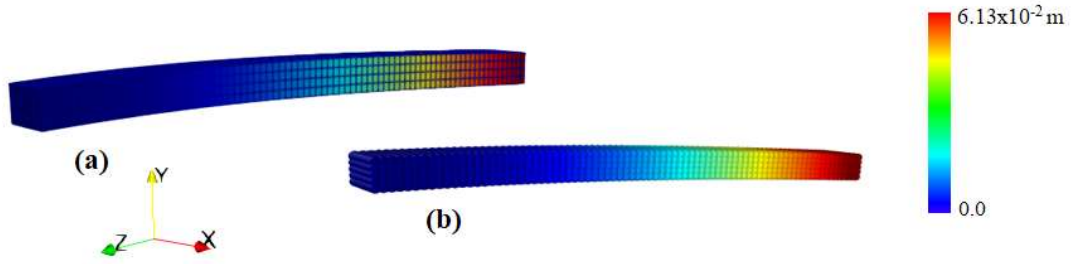

Figure B-3: Maximum displacement (a) the ParaView (mesh-based) and (b) Ovito (particle-based).

Again, this shows how both methods, for a given simple geometry, can give almost same result with little variation. When the problem involves a simple geometry, one has a choice of using either of the method because there is no significant difference or advantage in term of convenience, but when the problem involves fluid structure interactions, it is easy to handle it with particle method as we can see in the next chapters.

B.6 Conclusion

In this chapter, a linear elasticity problem was simulated with both mesh and particle-based modelling approach. The result shows that there is no significant difference between the two methods except little variation. The LSM equation always used 0.25 as Poisson's ratio (Kot et al., 2015) whereas the Poisson's ratio given for this problem in Elmer was 0.37 (Lyly et al, 1999). Though there is freedom of choosing any Poisson's ratio with mesh-based method, however, there is not such freedom when using the LSM (particle) method. Moreover, the displacement of the bar due to the applied force was more precise with the particle method because each particle's deformation can be accounted for (deformation at any position), unlike the mesh-based method that only gives the overall deformation.

In Chapters 4 and 5, the use of the particle approach with complex geometries was demonstrated.

B.7 Notation and abbreviations

Notation

m	mass [Kg]
ρ	Density [Kg m^{-3}]
g	Gravity [m s^{-2}]

r	Distance [m]
t	time [s]
F	Force [N]
K	Bulk Modulus [N m^{-2}]
k	Spring constant [N m^{-1}]
v	Poisson's ratio [-]
E	Young modulus [N m^{-2}]

Abbreviations

DMP	Discrete Multi-Physics
SPH	Smooth Particle Hydrodynamics
LSM	Lattice Spring Model
LAMMPS	Large-scale Atomic/Molecular Massively Parallel Simulator

APPENDIX C: CREATION OF BOND COEFFICIENT AND POSITIONS FOR CORONARY STENT GEOMETRY

In this Appendix, some of the files used which represent the arrangement of the particles, bonds, and the bond-coefficient were presented.

C1. Stent.csv file: Data file showing the particle positions on x,y,z (3D) coordinate.

S/N	Particle No.	X	Y	Z
1	2	1.98E-03	1.44E-03	0.00E+00
2	2	2.02E-03	1.44E-03	0.00E+00
3	2	2.05E-03	1.44E-03	0.00E+00
4	2	2.09E-03	1.44E-03	0.00E+00
5	2	2.12E-03	1.44E-03	0.00E+00
6	2	3.11E-03	1.44E-03	0.00E+00
7	2	3.15E-03	1.44E-03	0.00E+00
8	2	3.18E-03	1.44E-03	0.00E+00
9	2	3.22E-03	1.44E-03	0.00E+00
10	2	3.26E-03	1.44E-03	0.00E+00
11	2	4.24E-03	1.44E-03	0.00E+00
12	2	4.28E-03	1.44E-03	0.00E+00
13	2	4.32E-03	1.44E-03	0.00E+00
14	2	4.35E-03	1.44E-03	0.00E+00
15	2	4.39E-03	1.44E-03	0.00E+00
16	2	5.38E-03	1.44E-03	0.00E+00
17	2	5.41E-03	1.44E-03	0.00E+00
18	2	5.45E-03	1.44E-03	0.00E+00
19	2	5.52E-03	1.44E-03	0.00E+00
20	2	5.48E-03	1.44E-03	0.00E+00
21	2	1.98E-03	1.47E-03	0.00E+00
22	2	2.02E-03	1.47E-03	0.00E+00
23	2	2.05E-03	1.47E-03	0.00E+00
24	2	2.09E-03	1.47E-03	0.00E+00
25	2	2.12E-03	1.47E-03	0.00E+00
26	2	3.11E-03	1.47E-03	0.00E+00
27	2	3.15E-03	1.47E-03	0.00E+00
28	2	3.18E-03	1.47E-03	0.00E+00
29	2	3.22E-03	1.47E-03	0.00E+00
30	2	3.26E-03	1.47E-03	0.00E+00
31	2	4.24E-03	1.47E-03	0.00E+00
32	2	4.28E-03	1.47E-03	0.00E+00
33	2	4.32E-03	1.47E-03	0.00E+00
34	2	4.35E-03	1.47E-03	0.00E+00
35	2	4.39E-03	1.47E-03	0.00E+00
36	2	5.38E-03	1.47E-03	0.00E+00

37	2	5.41E-03	1.47E-03	0.00E+00
39	2	5.52E-03	1.47E-03	0.00E+00
*	*	*	*	*
*	*	*	*	*
46336	2	5.82E-03	3.25E-04	-1.51E-03

C2. MATLAB Code: This code generates the position of the bonds and bond coefficient of the stent geometry using the information of the particle positions (stent.csv). This is an example of the many MATLAB codes used in this work.

```
help size%load the stent.csv files with the stent
particles
clc
x=bar.x;
y=bar.y;
z=bar.z;
[Natoms, dummy]=size(x);
clear dr b1 b2
dL(1)=0.0125; %side distance between 2 stent particles
dL(2)=0.0125*sqrt(2);%diagonal distance between 2 stent
particles
nb = 1;
disp('please wait...');
file1 = fopen('Bonds.txt','w'); %open file1 for writing
fprintf(file1,'Bonds\n\n');
file2 = fopen('stent.bonds','w'); %open file2 for writing
for i=1:Natoms
    for j=i+1:Natoms
        dx = x(j)- x(i);
        dy = y(j)- y(i);
        dz = z(j)- z(i);
        r = sqrt(dx^2+dy^2+dz^2);
        if (r> 0.9*dL(1) && r <1.1*dL(2))
            b1(nb) = i;
            b2(nb) = j;
            dr(nb) = r;%distance of the bond
            string1 =[num2str(nb),' ',num2str(nb),'
',num2str(i),' ',num2str(j),'\n'];
            fprintf(file1,string1);
            string2 =['bond_coeff ',num2str(nb),' ${kB}
',num2str(r),'\n'];
            fprintf(file2,string2);
            nb = nb+1;
        end
    end
end
Nbonds = nb - 1;
disp([num2str(Nbonds), ' bonds']);
disp([num2str(Nbonds), ' bond types']);
fclose(file1);%close file
fclose(file2);%close file
```

C3. Bond Coefficient

```
bond_coeff    1     ${kB}     4e-05
bond_coeff    2     ${kB}     3e-05
bond_coeff    3     ${kB}     5e-05
bond_coeff    4     ${kB}     3.0707e-05
bond_coeff    5     ${kB}     3.8047e-05
bond_coeff    6     ${kB}     4.7e-05
bond_coeff    7     ${kB}     4.3257e-05
bond_coeff    8     ${kB}     4.8695e-05
bond_coeff    9     ${kB}     4e-05
bond_coeff    10    ${kB}     3e-05
bond_coeff    11    ${kB}     5e-05
bond_coeff    12    ${kB}     3.0707e-05
bond_coeff    13    ${kB}     3.8047e-05
bond_coeff    14    ${kB}     4.7e-05
bond_coeff    15    ${kB}     4.3257e-05
bond_coeff    16    ${kB}     4.8695e-05
bond_coeff    17    ${kB}     3e-05
bond_coeff    18    ${kB}     5e-05
bond_coeff    19    ${kB}     3e-05
bond_coeff    20    ${kB}     4.2426e-05
bond_coeff    21    ${kB}     4.8052e-05
bond_coeff    22    ${kB}     4.2588e-05
bond_coeff    23    ${kB}     4.4155e-05
bond_coeff    24    ${kB}     3.9638e-05
bond_coeff    25    ${kB}     3.7363e-05
bond_coeff    26    ${kB}     4e-05
bond_coeff    27    ${kB}     3e-05
bond_coeff    28    ${kB}     5e-05
bond_coeff    29    ${kB}     3e-05
bond_coeff    30    ${kB}     4.2426e-05
```

```
bond_coeff      31      ${kB}           4.8052e-05
bond_coeff      32      ${kB}           4.2588e-05
bond_coeff      33      ${kB}           4.4155e-05
bond_coeff      34      ${kB}           3.9638e-05
bond_coeff      35      ${kB}           3.7363e-05
bond_coeff      36      ${kB}           4e-05
bond_coeff      37      ${kB}           4.2426e-05
bond_coeff      38      ${kB}           3e-05
bond_coeff      39      ${kB}           5e-05
*               *       *               *
*               *       *               *
*               *       *               *
bond_coeff      303152 ${kB}            4e-05
```

C4. Bonds

S/N	x	y	z
1	1	1	2
2	2	1	21
3	3	1	22
4	4	1	82
5	5	1	83
6	6	1	84
7	7	1	138
8	8	1	139
9	9	1	34754
10	10	1	34773
11	11	1	34774
12	12	1	34834
13	13	1	34835
14	14	1	34836
15	15	1	34890
16	16	1	34891
17	17	2	3
18	18	2	21
19	19	2	22
20	20	2	23
21	21	2	85
22	22	2	87
23	23	2	91
24	24	2	139
25	25	2	142
26	26	2	34753
27	27	2	34755
28	28	2	34773
29	29	2	34774

30	30	2	34775
31	31	2	34837
32	32	2	34839
33	33	2	34843
34	34	2	34891
35	35	2	34894
36	36	3	4
37	37	3	22
38	38	3	23
39	39	3	24
*	*	*	*
*	*	*	*
303152	303152	46335	46336